

Quarterly Technical Report

Solid State Research

1985:4

Lincoln Laboratory

MASSACHUSETTS INSTITUTE OF TECHNOLOGY

LEXINGTON, MASSACHUSETTS



Prepared under Electronic Systems Division Contract F19628-85-C-0002.

Approved for public release; distribution unlimited.

ADA172872

The work reported in this document was performed at Lincoln Laboratory, a center for research operated by Massachusetts Institute of Technology, with the support of the Department of the Air Force under Contract F19628-85-C-0002.

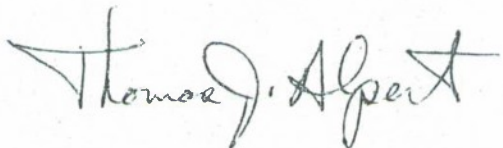
This report may be reproduced to satisfy needs of U.S. Government agencies.

The views and conclusions contained in this document are those of the contractor and should not be interpreted as necessarily representing the official policies, either expressed or implied, of the United States Government.

The ESD Public Affairs Office has reviewed this report, and it is releasable to the National Technical Information Service, where it will be available to the general public, including foreign nationals.

This technical report has been reviewed and is approved for publication.

FOR THE COMMANDER



Thomas J. Alpert, Major, USAF
Chief, ESD Lincoln Laboratory Project Office

Non-Lincoln Recipients

PLEASE DO NOT RETURN

Permission is given to destroy this document
when it is no longer needed.

**MASSACHUSETTS INSTITUTE OF TECHNOLOGY
LINCOLN LABORATORY**

SOLID STATE RESEARCH

QUARTERLY TECHNICAL REPORT

1 AUGUST — 31 OCTOBER 1985

ISSUED 6 FEBRUARY 1986

Approved for public release; distribution unlimited.

ABSTRACT

This report covers in detail the solid state research work of the Solid State Division at Lincoln Laboratory for the period 1 August through 31 October 1985. The topics covered are Solid State Device Research, Quantum Electronics, Materials Research, Microelectronics, and Analog Device Technology. Funding is provided primarily by the Air Force, with additional support provided by the Army, DARPA, Navy, SDIO, NASA, and DOE.

TABLE OF CONTENTS

Abstract	iii
List of Illustrations	vii
List of Tables	xi
Introduction	xiii
Reports on Solid State Research	xvii
Organization	xxv
1. SOLID STATE DEVICE RESEARCH	1
1.1 Serrodyne Optical Frequency Translation with High Sideband Suppression	1
1.2 Performance and Reproducibility of Mach-Zehnder Interferometer Arrays in Ti:LiNbO ₃ Operating at Wavelengths from 0.458 μm to 3.39 μm	2
1.3 Series Resistance in GaInAsP/InP Buried-Heterostructure Lasers Fabricated on p-type Substrates	6
2. QUANTUM ELECTRONICS	11
2.1 Ti:Al ₂ O ₃ Laser Experiments	11
2.2 Fast Electro-optical Tuning for a Frequency-Agile Laser System	12
2.3 Frequency Conversion Using KTP	14
3. MATERIALS RESEARCH	19
3.1 Growth and Characterization of Ti:Al ₂ O ₃ Crystals	19
3.2 Monolithic Integration of GaAs MESFETs and Si MOSFETs	22
3.3 Picosecond Photodetectors Fabricated in Heteroepitaxial GaAs Layers	24
3.4 Static Random-Access Memories Fabricated in Zone-Melting-Recrystallized Silicon-On-Insulator Films	28
3.5 High-Efficiency Double-Heterostructure AlGaAs/GaAs Solar Cells	31
4. MICROELECTRONICS	37
4.1 Quantum-Well Charge-Coupled Devices	37
4.2 Balanced Monolithic Mixer for Use at 44 GHz	40
4.3 Excimer-Laser Etching of Diamond and Hard Carbon Films By Direct Writing and Optical Projection	44
4.4 Hot Jet Etching of GaAs and Si	47

5. ANALOG DEVICE TECHNOLOGY	53
5.1 Dual-Channel, 256-Sample, 128-Tap Analog-Binary Charge-Coupled-Device (CCD) Correlator	53
5.2 Optically Addressed Readout of MOS and MNOS Arrays	56
5.3 A SAW-Based Communication Link with Precise Time-of-Arrival Measurements	59

LIST OF ILLUSTRATIONS

Figure No.		Page
1-1	Schematic Illustration of Waveguide Device and Sawtooth Drive Circuit for Evaluating Serrodyne Frequency Translation	1
1-2	Experimental Results Obtained when $\Delta f_2 = 5$ kHz and $\Delta f_1 = 40$ kHz with Input Polarizer Set at (a) 0° (TE Excitation) and (b) 45° (both TE and TM Excitation). The Dominant Component is at 45 kHz and the Sideband Spacing is 5 kHz	3
1-3	(a) Performance of 20-Interferometer Array with Incident $0.82\text{-}\mu\text{m}$ Radiation and a Readout Using a Silicon Imaging CCD. The Outputs at the 'nulls' at $\pm 180^\circ$ are Due to Crosstalk in the CCD Designed for the Visible. The Curves Have Been Shifted in Phase so the Maxima for the Interferometers Occur at 0° . (b) Histogram of the Imbalance in the Lengths of the Arms of Each Interferometer Obtained from the Above Shift in ϕ (Solid Line). The Number of the Interferometer in the Array Is Noted. The Dashed Lines Are Data Taken Nine Months Earlier and Plotted with a Slightly Higher Resolution on a Different Array. The Two Arrays Were Fabricated with the Same Photomask	4
1-4	The Optical Path Difference (OPD) Measured by a 20-Interferometer Array with Incident $3.39\text{-}\mu\text{m}$ Radiation is Compared with OPD Expected (Solid Curve) for a Beam Diverging from a Point Source 1.65 m Distant	5
1-5	Performance of Interferometer Array at $0.458 \mu\text{m}$. The Curves Have Been Shifted in ϕ so the Maxima for the Interferometers Occur at 0°	6
1-6	Calculated Current and Voltage Distributions in a p-Substrate GaInAsP/InP Buried-Heterostructure Laser. The Solid and Dashed Curves are the Equipotentials and Streamlines, Respectively. The Equipotentials Are Shown in Voltage Increments of 0.1 V. The Junction Voltage at the GaInAsP Active Region is 0.98 V. ¹²	7
1-7	The Conformal Mapping Used to Calculate the Current and Voltage Distributions in the p-Substrate, Buried-Heterostructure Laser. The Solid and Dashed Curves are the Equipotentials and Streamlines, Respectively. Part (a) Shows the Simple Case of Current Flowing (Uniformly from All Directions at Infinity) Into a Slit That is Maintained at a Constant Potential of $\Phi = 0$	8

Figure No.		Page
1-8	Calculated Spreading Resistance for the p-Substrate, Buried-Heterostructure Laser as a Function of the Device Geometry	9
2-1	Peak Output Power of the Ti:Al ₂ O ₃ Laser vs Argon-Ion Laser Peak Pump Power Incident upon the Input Face of the Crystal at Room Temperature. The Two Curves Correspond to Two Different Duty Cycles (4.2% and 50%, Respectively) of the Mechanically Chopped Pump Beam	11
2-2	Tunable Laser Cavity	13
2-3	Principle of Operation of the Electro-Optic Tuning Device	13
2-4	Wavelength-vs-Time Transient Response of a Laser Driven by a 400 V Pulse Applied to the Intracavity E-O Tuning Cell	15
2-5	SHG in 5 mm KTP Crystal as a Function of Input Power Density	16
3-1	Single Crystal of Ti:Al ₂ O ₃ Grown by Thermal-Gradient-Freeze Technique from Charge Containing 0.5 wt% Ti ₂ O ₃	19
3-2	Absorptance Spectra for Light Polarized Parallel to the c Axis, Taken at Seven Positions Along the Length of the Crystal Shown in Figure 3-1	20
3-3	Absorption Coefficient Corresponding to Peak Absorptance for the Spectra of Figure 3-2, Plotted Against Distance from the Top of the Crystal	21
3-4	Processing Steps for Monolithic Integration of Si MOSFETs and GaAs MESFETs	22
3-5	Optical Micrograph of GaAs MESFET and Adjacent Si MOSFET Fabricated on the Same GaAs/Si Substrate, Together with Transistor Characteristics for Each Device	23
3-6	Sampling Oscilloscope System for Measuring Photodetector Response	25
3-7	Correlation Measurement System and Dual Detector Configuration	26
3-8	Pulse Response of Interdigitated MGS Photodetector	26
3-9	Pulse Response of Interdigitated MGSOS Photodetector	27
3-10	Correlation Signal from Monolithic Pair of MGSOS Photodetectors	28
3-11	CMOS 1-K Static Random-Access Memory (SRAM) Chip Fabricated in Zone-Melting-Recrystallized Si-on-Insulator (SOI) Film	29

Figure No.		Page
3-12	Characteristics of SOI SRAM for (a) Read '0', and (b) Read '1' Operations	30
3-13	Chip-Enable Access Time vs Supply Voltage for SOI SRAM	31
3-14	Schematic Cross Section of a Double-Heterostructure (DH) Solar Cell	32
3-15	Current-Voltage Characteristic Under One-Sun Simulated AM1 Illumination for a DH Solar Cell	33
3-16	External Quantum Efficiency vs Wavelength for the Cell of Figure 3-15	33
4-1	Cross-Sectional View of an Integrated Quantum-Well CCD/MQW Spatial Light Modulator	37
4-2	Material Layer Sequence and Energy-Band Diagram of the Structure of Figure 4-1 for the Full Well or Thermal Equilibrium Case (Solid Curves and Dashed Line for the Fermi Level) and for the Empty-Well Case when the Carriers Are Removed from the GaAs CCD Quantum-Well Channel (Dashed Curves)	38
4-3	Electrical Performance of a 16-Stage Quantum-Well CCD at a 1-MHz Data Rate. Upper Trace Is an Input Signal of Eight Pulses, While Lower Trace Is the Delayed Output from the Device	39
4-4	Projected Embedding Impedance Locus for a Monolithic Mixer Circuit as a Function of Frequency	41
4-5	Balanced Monolithic Mixer	41
4-6	Balanced 44-GHz Monolithic Mixer in Orthogonal Waveguide Structure	42
4-7	Assembled 44-GHz Balanced Monolithic Mixer	43
4-8	Balanced Monolithic Mixer Single-Sideband Noise Figure vs Frequency	43
4-9	Scanning Electron Micrograph of a 0.25- μm -Period Grating Etched in Monocrystalline Diamond with a 0.193- μm Laser. The Grating Was Generated in Projection with One 15-ns Excimer-Laser Pulse. The Fluence Was 65 J/cm ²	45
4-10	Schematic Representation of the Excimer-Laser/Diamond Interaction	46

Figure No.		Page
4-11	Scanning Electron Micrographs at Two Different Magnifications of Grooves Etched in GaAs Following Exposure of the Carbon Thin Film to Excimer-Laser Irradiation (0.5 J/cm^2 , One 15-ns Pulse). In (a) the Carbon Film and the Laser-Induced Etch Pattern on It Are Clearly Visible	46
4-12	Diagram of the Hot Jet Etching System	48
4-13	Percentage of Radicals Formed by Thermal Dissociation	49
4-14	Scale Drawing of the Hot Jet. The Hot Jet Dimensions Were Found Not To Be Critical	50
5-1	CCD Correlator Block Diagram	54
5-2	Code Input (Top Traces) and Correlation Output (Bottom Traces) Displayed at (a) $5 \mu\text{s}/\text{div}$ and (b) $100 \text{ ns}/\text{div}$	56
5-3	Cross Section of MNOS Pixel During Optically Addressed Readout. The Pixel Is Discharged by Hole-Electron Pairs Created in the Depletion Layer by the Readout Beam	57
5-4	Measured Output of an MNOS Pixel as a Function of the Stored Image Intensity. One Curve Was Measured by a Conventional C(V) Determination of the Flatband Voltage; the Second Curve Was Measured by the Optically Addressed Technique	59
5-5	The Hybrid Analog/Digital Signal Processor Located in the Modem	60
5-6	Incoherent Binary Integration for Finding a Precursor. The Top Photo is the Input to the Matched Filter. The Two Middle Photos Are Consecutive Output Frames from the Matched Filter, Each Containing a Data Bit. The Precursor Can Just Barely Be Seen But Will Integrate Up Out of the Noise to a Detectable Level in the Binary Integrator. The Two Data Bits Are the Same in This Case as Can Be Seen by the Output Appearing on the Sum Port. The Running DPSK Decision That Is Stored for the Binary Integrator Also Is Displayed. The Bottom Photo Shows the Result Out of the Binary Integrator After Detection. The Precursor Location with Respect to the Large Signal Represents the Improvement in the Time-of-Arrival Measurement	62

LIST OF TABLES

Table No.		Page
4-1	Hot Jet Etching	50
5-1	Correlator Specifications	53

INTRODUCTION

SOLID STATE DEVICE RESEARCH

A Ti:LiNbO₃ serrodyne optical frequency translator with 42-dB overall sideband suppression for frequency shifts of 40 kHz has been demonstrated. The device utilizes a single-polarization waveguide design and a specialized sawtooth drive circuit.

Mach-Zehnder interferometer arrays have been operated at 0.458 μm , 0.82 μm and 3.39 μm . Interferometers in the 20-element arrays were reproducibly fabricated with extinction ratios >17 dB; the measured input phase biases were determined predominantly by the photolithographic mask.

GaInAsP/InP buried-heterostructure lasers fabricated on p-InP substrates offer considerable advantages in terms of reduced series resistance because of the large-area p-contact. A simple formula has been derived that permits an accurate calculation of the spreading resistance in the p-InP.

2. QUANTUM ELECTRONICS

Low threshold operation has been achieved in a Ti:Al₂O₃ laser pumped at room temperature by a multiline Ar laser. The use of a near concentric laser cavity resulted in a threshold of 1.8 W when the pump was chopped at a 4.2% duty cycle and 2.2 W when chopped at 50% duty cycle.

Initial work on cavity design for a frequency-agile laser has demonstrated the fast-tuning capability of a simple electro-optic birefringent filter. The filter (a commercial Pockels cell) is used inside the laser cavity and is tunable through the gain bandwidth of a dye laser when driven by moderate voltages (under 1 kV).

Preliminary frequency-doubling and damage threshold experiments were performed on KTP crystals irradiated with a focused 1- μs -long laser pulse operating at a wavelength of 1.645 μm . Significant variation in the resistance to damage was observed both between crystals and within a single crystal.

3. MATERIALS RESEARCH

A seeded thermal-gradient-freeze technique has been used to grow Ti:Al₂O₃ single crystals for tunable lasers from charges containing between 0.15- and 0.5-mole percent Ti₂O₃. For the most heavily doped crystal, the highest optical absorption coefficient measured at the peak of the Ti³⁺ pump band is 5 cm⁻¹, corresponding to an estimated Ti₂O₃ concentration of 0.19 weight percent.

Both GaAs MESFETs and Si MOSFETs have been fabricated on a monolithic GaAs/Si substrate prepared by the growth of GaAs epitaxial layers on selected areas of a Si wafer. The operating characteristics of the GaAs and Si devices are comparable to those of similar devices fabricated on separate GaAs and Si wafers.

Photoconductive detectors with response times of \sim 60 and \sim 40 ps (FWHM), respectively, have been fabricated in GaAs layers grown by molecular beam epitaxy on silicon and silicon-on-sapphire wafers. Such detectors could be combined readily with GaAs logic devices such as MESFETs to

provide high-speed optical to electrical conversion for optical interconnects that are integrated with Si circuits on a monolithic GaAs/Si substrate.

Fully functional 1-K static random-access memories have been fabricated by a coplanar CMOS process in Si-on-insulator films prepared by zone-melting recrystallization. These memories, each containing about 8200 transistors with a minimum feature size of 4 μm , are superior in speed performance to commercial bulk Si memories of similar configuration.

Double-heterostructure solar cells have been fabricated from wafers prepared by using organometallic chemical vapor deposition to grow a p GaAs absorbing layer sandwiched between p⁺ and n⁺ AlGaAs layers. The best cell, which incorporates an abrupt AlGaAs/GaAs shallow heterojunction, exhibits a global AM1 one-sun conversion efficiency of 23%.

4. MICROELECTRONICS

A novel single-sideband balanced monolithic mixer has been fabricated for use at 44 GHz. The mixer has a single-sideband noise figure of 6.5 dB flat to within 0.5 dB over a 2-GHz band centered at 44 GHz.

A new heterojunction charge-coupled device has been demonstrated in which the carriers are confined to a narrow quantum well consisting of a 140-Å layer of GaAs clad on both sides by Al_{0.3}Ga_{0.7}As. The carrier confinement minimizes the charge packet volume and therefore bulk trapping effects. A 16-stage CCD has been operated at a 1-MHz clock and showed no measurable trapping effects.

Excimer-laser patterning of crystalline diamond and diamond-like carbon thin films was performed in the direct-writing and optical-projection modes. Linewidths as narrow as 0.13 μm were etched with single 0.193 μm wavelength laser pulses. The effectiveness of the diamond-like carbon thin films for submicrometer resolution lithography of semiconductors was demonstrated.

A new anisotropic dry etching technique (hot jet etching) that does not require ions or plasmas has been developed. The anisotropic etching is obtained from a directed flux of chemically reactive species. The reactive species are obtained by thermally decomposing comparatively unreactive feed gases in a resistively heated tube. Etch rates as high as 5 $\mu\text{m}/\text{min}$ have been obtained with Cl₂ and GaAs samples.

5. ANALOG DEVICE TECHNOLOGY

A dual-channel, 256-sample, 128-tap analog-binary CCD has been designed and fabricated for use as a correlator. To facilitate a wide range of applications, the device, which will operate at 25 MHz with 50-dB dynamic range, has been architected to be flexible, self-contained, and simple to use. Preliminary tests at 5 MHz have demonstrated functionality of the device as well as compatibility with commercial CCD foundries.

An optically addressed output technique for MOS and MNOS arrays, in particular imagers, has been developed. Storage wells containing signals, represented by packets of charge existing in either

nonvolatile storage in the gate dielectric or volatile dynamic storage in an inversion layer, are addressed and discharged by a scanned beam of light. Output is measured as a substrate current and requires only two electrodes on the array.

A spread-spectrum radio that exploits 100-MHz-bandwidth surface-acoustic-wave (SAW) convolvers and binary-quantized digital post-processing circuits has been developed to provide data communications at rates that range from 1.45 Mbps down to 44 bps with the commensurate and almost ideal trade for signal processing gain of 18 dB up to 61 dB. This processing, in combination with error correction, permits efficient demodulation even in the presence of severe interference within a multipath environment. The signal processing also facilitates radio ranging measurements to a 3-meter resolution.

REPORTS ON SOLID STATE RESEARCH

1 August through 31 October 1985

PUBLISHED REPORTS

Journal Articles

JA No.

5672	Single-Mode Optical Waveguides and Phase Modulators in the InP Material System	J.P. Donnelly N.L. DeMeo F.J. Leonberger* S.H. Groves F.J. O'Donnell	IEEE J. Quantum Electron. QE-21 , 1147 (1985)
5709	Multigigahertz Lumped-Element Electrooptic Modulators	R.A. Becker	IEEE J. Quantum Electron. QE-21 , 1144 (1985)
5715	Design Considerations for Flat-Plate Photovoltaic/Thermal Collectors	C.H. Cox, III P.Raghuraman	Sol. Energy 35 , 227 (1985)
5730	Applications of Saw Convolvers to Spread-Spectrum Communications and Wideband Radar	I.Yao J.H. Cafarella	IEEE Trans. Sonics Ultrason. SU-32 , 760 (1985)
5742	The SAW/FET Signal Processor	J.B. Green G.S. Kino*	IEEE Trans. Sonics Ultrason. SU-32 , 734 (1985)
5760	Metal-Oxide-Semiconductor Field-Effect Transistors Fabricated Using Self-Aligned Silicide Technology	B-Y. Tsaur C.H. Anderson, Jr.	Appl. Phys. Lett. 47 , 527 (1985)
5761	Theory of the Effect of Traps on the Spectral Characteristics of Diode Lasers	H.J. Zeiger	Appl. Phys. Lett. 47 , 545 (1985)
5792	Tunable Paramagnetic-Ion Lasers	P.F. Moulton	Chapter in <i>Laser Handbook</i> , Vol. V, edited by M. Bass and M.L. Stich, (North-Holland Physics Publishing, Amsterdam, The Netherlands, 1985)

* Author not at Lincoln Laboratory.

Meeting Speeches

MS No.

6550B	Recent Advances in Transition-Metal-Doped Lasers	P.F. Moulton	<i>Tunable Solid-State Lasers</i> , P. Mammerling, A.B. Budgore, and A. Pinto, eds. (Springer-Verlag, Berlin, 1985), p. 4
6692	Graphite-Strip-Heater Zone-Melting Recrystallization of Si Films	J.C.C. Fan	Proc. 1984 Seoul International Symposium on the Physics of Semiconductors and Its Applications, Seoul, Korea, 1984, p. 99
6794	High-Speed Analog Signal Processing with Superconductive Circuits	R.W. Ralston	In <i>Picosecond Electronics and Optoelectronics</i> , Vol. 21, G.A. Mourou, D.M. Bloom, and C-H. Lee, Eds. (Springer-Verlag, New York, 1985) p. 228
6839	High-Speed Optoelectronic Track-and-Hold Circuits in Hybrid Signal Processors for Wideband Radar	I.Yao V. Diadiuk E.M. Hauser C.A. Bouman	In <i>Picosecond Electronics and Optoelectronics</i> , Vol. 21, G.A. Mourou, D.M. Bloom, and C-H. Lee, Eds. (Springer-Verlag, New York, 1985) p. 207
6891	Basic Concepts for the Design of High-Efficiency Single-Junction and Multibandgap Solar Cells	J.C.C. Fan	In <i>Photovoltaics: Critical Review of Technology</i> , S.K. Deb, Ed., Proc. SPIE 543, 30 (1985)

UNPUBLISHED REPORTS

Journal Articles

JA No.

5766	Room-Temperature Operation of GaAs/AlGaAs Diode Lasers Fabricated on a Monolithic GaAs/Si Substrate	T.H. Windhorn G.M. Metze	Accepted by Appl. Phys. Lett.
5767	Double Heterostructure InGaAs/InP PIN Photodetectors	V.Diadiuk S.H. Groves	Accepted by Solid-State Electron.
5786	Photorefractive Effects in LiNbO ₃ Channel Waveguides: Model and Experimental Verification	R.A. Becker R.C. Williamson	Accepted by Appl. Phys. Lett.
5801	Theoretical Temperature Dependence of Solar Cell Parameters	J.C.C. Fan	Accepted by Solar Cells
5802	Spectroscopic and Laser Characteristics of Ti:Al ₂ O ₃	P.F. Moulton	Accepted by J. Opt. Soc. Am. B
5804	Use of Zone-Melting Recrystallization to Fabricate a 3-Dimensional Structure Incorporating Power Bipolar and Field Effect Transistor	M.W. Geis C.K. Chen R.W. Mountain N.P. Economou W.T. Lindley P.L. Hower*	Accepted by IEEE Electron. Device Lett.
5807	Early Applications of Laser Direct Patterning: Direct-Writing and Excimer Projection	D.J. Ehrlich	Accepted by Solid State Technol.
5810	Characterization and Entrainment of Subboundaries and Defect Trails in Zone-Melting Recrystallized Si Films	M.W. Geis H.I. Smith* C.K. Chen	Accepted by J. Appl. Phys.
5813	Low-Resistance Pd/Ge/Au & Ge/Pd/Au Ohmic Contacts to n-Type GaAs	C.L. Chen L.J. Mahoney M.C. Finn R.C. Brooks A. Chu J.G. Mavroides	Accepted by Appl. Phys. Lett.

* Author not at Lincoln Laboratory.

JA No.

5814	Millimeter-Wave Monolithic Circuit for Receiver and Transmitter Applications	A. Chu W.E. Courtney L.J. Mahoney B.J. Clifton	Accepted by RCA Rev.
5815	The Quest for the 200-GHz Transistor	R.A. Murphy	Accepted by IEEE Electrotechnology Rev.

Meeting Speeches†**MS No.**

6301A	Laser-Localized Selective Etching and Application to Aluminum	J.Y. Tsao D.J. Ehrlich D.J. Silversmith R.W. Mountain	Electrochemical Society Meeting, Las Vegas, Nevada, 13-18 October 1985
6375A	Comparison of Device Technologies	E. Stern	{ Conference on Technology for High Speed Signal Processing, Norwegian Institute of Technology, Trondheim, Norway, 21-23 August 1985
6712B	Wideband Radar Signal Processing Using Surface-Acoustic-Wave, Optoelectronic and Charge-Coupled Devices	I. Yao R.W. Ralston	
6720D	SOI Technologies: Device Applications and Future Prospects	B-Y. Tsaur	Seminar, Raytheon Company, Lexington, Massachusetts, 16 October 1985
6796A	Hybrid Signal Processor for Wideband Radar	I. Yao E.M. Hauser C.A. Bouman G.T. Flynn A.M. Chiang R.W. Ralston	Eleventh DARPA Strategic Systems Symposium, Monterey, California, 23 October 1985
6869	A Wideband Packet Radio Based on Hybrid Analog/Digital Signal Processing and Layered Architecture	J.H. Fischer J.H. Cafarella C.A. Bouman G.T. Flynn D.R. Arsenault J.D. Kurtze* R.R. Boisvert	MILCOM '85, Bedford, Massachusetts, 20-23 October 1985

* Author not at Lincoln Laboratory.

† Titles of Meeting Speeches are listed for information only. No copies are available for distribution.

MS No.

6878	CCD for Two Dimensional Transform	A.M. Chiang B.B. Kosicki R.W. Mountain G.A. Lincoln B.J. Felton	Applications of Digital Imaging Process III, SPIE, San Diego, California, 18-23 August 1985
6890	Integrated-Optical Components for Fiber Gyroscopes	L.M. Johnson	SPIE Annual Technical Symposium, San Diego, California, 18-23 August 1985
6920	Fundamental Spectral Width of Laser Light	A. Mooradian	XII National Conference on Laser and Nonlinear Optics, Moscow, USSR, 26-29 August 1985
6920B	Laser Linewidth and Devices	A. Mooradian	Seminar, Boston College, Newton, Massachusetts, 9 October 1985
6921	Methods of Characterizing Photorefractive Susceptibility of LiNbO_3 Waveguides	R.A. Becker	Second International Conference on Integrated Optical Circuit Engineering, part of SPIE Symposium on Optical and Electro-Optical Engineering, Cambridge, Massachusetts, 15-20 September 1985
6928	Integrated-Optical Components for Fiber Sensors	L.M. Johnson	
6922	Current Prospects for the Permeable Base Transistor	C.O. Bozler	Modulated Semiconductor Structures, Yamada Science Foundation, Kyoto, Japan, 9-13 September 1985
6924	Advances in the Technology of the Preparation of Single and Double Epitaxial Layers on $\text{Hg}_{1-x}\text{Cd}_x\text{Te}$ Grown by LPE Using Mercury-Pressure-Controlled Growth Solutions	T.C. Harman	1985 Meeting of the IRIS Specialty Group on Infrared Detectors, Boulder, Colorado, 6-8 August 1985

MS No.

6934A	Superconductive Analog Signal Processing Devices	R.S. Withers	Topics in Superconductivity, MIT, Cambridge, Massachusetts, 9 October 1985
6936	Nitrocellulose as a Self-Developing Resist	M.W. Geis J.N. Randall R.W. Mountain J.D. Woodhouse E.I. Bromley D.K. Astolfi N.P. Economou	ACS Symposium, Chicago, Illinois, 8-13 September 1985
6943	Microstructure Electromagnetic Effects	S.R.J. Brueck	Annual Meeting, Optical Society of America, Washington, D.C., 14-18 October 1985
6966	Coherent Ensemble of Diode Lasers with Feedback in the Fourier Plane	R.H. Rediker K.K. Anderson C. Corcoran*	
6947	OMCVD Growth of GaAs and AlGaAs in a Novel Horizontal Reactor	R.P. Gale	
6951	Acoustoelectronic Rayleigh Wave Devices	E. Stern	Second Biennial OMVPE Workshop, Ithaca, New York, 1-2 August 1985
6952	Prospects for Printing VLSI Circuits with Large-Area Ion Beams	J.N. Randall	Rayleigh Wave Centenary Symposium, Rank Prize Fund, IEE, The Royal Institution, England, 15-17 July 1985
6957	Wideband Chirp-Transform Adaptive Filter	D.R. Arsenault	American Vacuum Society Thirty-second National Symposium, Houston, Texas, 19-22 November 1985
6960	SAW/FET Programmable Transversal Filter with 100-MHz Bandwidth and Enhanced Programmability	D.E. Oates D.L. Smythe J.B. Green	

* Author not at Lincoln Laboratory.

MS No.

6961	Autocalibrating Circuitry for Processing SAW Convolver Outputs	J.H. Fischer	1985 IEEE Ultrasonics Symposium, San Francisco, California, 16-18 October 1985
6967	Single-Cell Concepts for Obtaining Photovoltaic Conversion Efficiency Over 30%	J.C.C. Fan	Eighteenth IEEE Photovoltaic Conference, Las Vegas, Nevada, 21-25 October 1985
6970	A High-Efficiency Double- Heterostructure AlGaAs/GaAs Solar Cell	R.P. Gale J.C.C. Fan G.W. Turner R.L. Chapman	
6989	Superconductive Time Integrating Correlator Design and Component Development	J.B. Green A.C. Anderson S.A. Rible	
6992	Superconductive Content- Sequential Readout	L.N. Smith	Workshop on Superconducting Electronic Devices, Circuits and Systems, Waterville Valley, New Hampshire, 11-15 August 1985
6996	Materials and Processes for Analog Device Fabrication	A.C. Anderson R.S. Withers	
6998	Development and Application of Wideband Signal-Processing Devices	R.S. Withers	
6991	Plasma Etching of GaAs with CCl_2F_2 and Additive Gases	A.R. Forte D.D. Rathman L.J. Mahoney	SOTAPCOCS III, Las Vegas, Nevada, 13-18 October 1985
7000	Quantum Well CCDs for Multiple Quantum Well Spatial Light Modulators	W.D. Goodhue B.E. Burke K.B. Nichols G.M. Metze G.D. Johnson	Sixth Molecular Beam Epitaxy Workshop, American Vacuum Society, Minneapolis, Minnesota, 14-16 August 1985

MS No.

7048	Excimer Laser Projection Patterning With and Without Resists	D.J. Ehrlich	Seventh International Conference on Photopolymers, Ellenville, New York, 28-30 October 1985
7055	Beam Processing	D.J. Ehrlich	Future of Microstructure Technology, AFOSR, Seabrook Island, South Carolina, 14 October 1985

ORGANIZATION

SOLID STATE DIVISION

A.L. McWhorter, *Head*
I. Melngailis, *Associate Head*
E. Stern, *Associate Head*
J.F. Goodwin, *Assistant*

P.E. Tannenwald, *Senior Staff*

QUANTUM ELECTRONICS

A. Mooradian, *Leader*
P.L. Kelley, *Associate Leader*

Barch, W.E.
Belanger, L.J.
Bushee, J.F., Jr.
Daneu, V.
DeFeo, W.E.
Feldman, B.
Hancock, R.C.
Harrison, J.*

Johnson, B.C.*
Killinger, D.K.
Le, H.
Menyuk, N.
Sanchez-Rubio, A.
Sharpe, K.A.
Sullivan, D.J.

ELECTRONIC MATERIALS

A.J. Strauss, *Leader*
B-Y. Tsaur, *Assistant Leader*
H.J. Zeiger, *Senior Staff*

Anderson, C.H., Jr.
Button, M.J.
Chen, C.K.
Choi, H.K.
Connors, M.K.
Delaney, E.J.
Fahey, R.E.
Finn, M.C.
Iseler, G.W.
Kolesar, D.F.
Krohn, L., Jr.
Mastromattei, E.L.
Nitishin, P.M.
Pantano, J.V.
Tracy, D.M.
Turner, G.W.
Wang, C.A.
Windhorn, T.H.

APPLIED PHYSICS

R.C. Williamson, *Leader*
D.L. Spears, *Assistant Leader*
T.C. Harman, *Senior Staff*
R.H. Rediker, *Senior Staff*

Anderson, K.K.*
Aull, B.F.
Betts, G.E.
Chan, S.K.*
Cox, C.H., III
DeMeo, N.L., Jr.
Diadiuk, V.
Donnelly, J.P.
Duffy, P.E.

Ferrante, G.A.
Groves, S.H.
Hovey, D.L.
Johnson, L.M.
Liau, Z.L.
Lind, T.A.
McBride, W.F.
Metze, G.M.
Molter, L.A.*

O'Donnell, F.J.
Plonko, M.C.
Reeder, R.E.
Tsang, D.Z.
Walpole, J.N.
Whitaker, N.*
Woodhouse, J.D.
Yap, D.*
Yee, A.C.

* Research Assistant

ANALOG DEVICE TECHNOLOGY

R.W. Ralston, *Leader*
R.S. Withers, *Assistant Leader*

Anderson, A.C.
Arsenault, D.R.
Boisvert, R.R.
Brogan, W.T.
Delaney, M.A.*
Denneno, A.P.
DiIorio, M.S.
Dolat, V.S.

Fischer, J.H.
Fitch, G.L.
Flynn, G.T.
Grant, P.M.
Green, J.B.
Holtham, J.H.
Kernan, W.C.
Lattes, A.L.

Macedo, E.M., Jr.
Macopoulos, W.
Marden, J.A.
Munroe, S.C.
Oates, D.E.
Sage, J.P.
Thompson, K.E.†
Yao, I.

MICROELECTRONICS

W.T. Lindley, *Leader*
D.J. Ehrlich, *Assistant Leader*
B.B. Kosicki, *Assistant Leader*
R.A. Murphy, *Assistant Leader*

Astolfi, D.K.
Bales, J.W.*
Bennett, P.C.
Black, J.G.
Bozler, C.O.
Brown, E.R.
Burke, B.E.
Calawa, A.R.
Chen, C.L.
Chiang, A.M.
Clifton, B.J.
Correa, C.A.
Daniels, P.J.
Doran, S.P.
Durant, G.L.
Efremow, N.N., Jr.
Felton, B.J.

Gajar, S.*
Geis, M.W.
Goodhue, W.D.
Gray, R.V.
Hollis, M.A.
Huang, J.C.M.
Lax, B.†
LeCoz, Y.L.*
Lincoln, G.A., Jr.
Lysczarz, T.M.
Mahoney, L.J.
Manfra, M.J.
McGonagle, W.H.
Melngailis, J.†
Mims, V.A.†
Mountain, R.W.
Nichols, K.B.

Oliver, S.
Paczuski, M.
Pang, S.W.
Parker, C.D.
Pichler, H.H.
Rabe, S.
Randall, J.N.
Rathman, D.D.
Reinold, J.H.
Rothschild, M.
Sedlacek, J.H.C.
Smythe, D.L., Jr.
Sollner, T.C.L.G.
Stern, L.A.
Taylor, J.A.*
Vera, A.
Wilde, R.E.

* Research Assistant

† Part Time

‡ Staff Associate

1. SOLID STATE DEVICE RESEARCH

1.1 SERRODYNE OPTICAL FREQUENCY TRANSLATION WITH HIGH SIDEBAND SUPPRESSION

Guided-wave serrodyne optical frequency shifters are being developed for a variety of applications, such as the phase-nulling optical fiber gyroscope.^{1,2} Here we present experimental results on a Ti:LiNbO₃ serrodyne frequency translator that utilizes a single-polarization waveguide design and a specialized sawtooth drive circuit. Overall sideband suppression of 42 dB was achieved for frequency shifts up to 40 kHz. The sideband suppression was nearly independent of the input polarization state. This is the highest known overall sideband suppression yet reported for such a device.

Serrodyne optical frequency translation³ is realized by applying sawtooth phase modulation to an optical signal. Ideally, the sawtooth has an infinitely fast fall time and an amplitude equal to $2\pi n$ radians, where n is an integer. This yields a frequency shift $\Delta f = n/T$ with 100% conversion efficiency, where T is the sawtooth period. Nonideal sawtooth modulation results in additional sidebands at integral multiples of $1/T$.

Serrodyne optical frequency translation was tested by means of a guided-wave Mach-Zehnder interferometer and sawtooth drive circuit, as shown in Figure 1-1. The drive circuit provides a

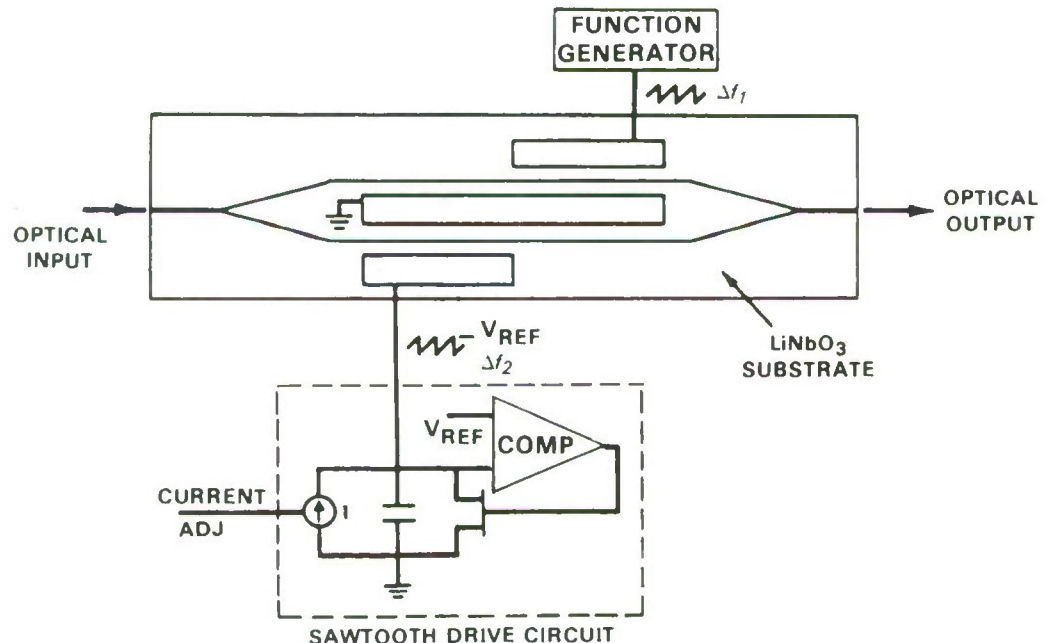


Figure 1-1. Schematic illustration of waveguide device and sawtooth drive circuit for evaluating serrodyne frequency translation.

high-quality sawtooth signal at the serrodyne test frequency Δf_2 , which is applied to one arm of the interferometer, a lower-quality sawtooth signal at a much higher frequency Δf_1 is applied to the other arm. This arrangement enabled both the fundamental frequency shift at $\Delta f_1 + \Delta f_2$ and the various sidebands at $\Delta f_1 \pm m \Delta f_2$ ($m = 0, 1, 2, 3, \dots$) associated with Δf_2 frequency shifting to be measured easily on a spectrum analyzer.

The ramp portion of the sawtooth is generated by applying a constant current to a capacitor, which results in a linear increase in capacitor voltage. Restarting the ramp is accomplished using a comparator and FET switch to discharge the capacitor periodically. This implementation permits independent control of the sawtooth frequency and amplitude by adjusting the charging current and comparator reference voltage, respectively. The circuit can operate at sawtooth frequencies as high as 40 kHz with fall times as short as 100 ns. Since LiNbO₃ phase modulators are polarization sensitive, simultaneous input excitation of the TE and TM modes as well as coupling and scattering between these modes can limit overall sideband suppression. This effect is minimized here by suppressing TM mode transmission. The waveguide fabrication parameters were chosen to provide single-mode operation at 0.85 μm with a well-confined TE mode and a nearly cutoff TM mode. The TM signal therefore is highly attenuated through the branches and bends of the interferometer.

The device was tested, as shown in Figure 1-1, by applying 5-kHz and 40-kHz sawtooth signals from the drive circuit and a function generator, respectively. A polarizer was placed at the device input to adjust the relative excitation of the TE and TM modes. Light was endfire-coupled into the device from a 0.85- μm diode laser, and the output of the detector was displayed on a spectrum analyzer. The sawtooth voltages were adjusted to maximize overall sideband suppression. Shown in Figure 1-2(a) is the result when the polarizer is set at 0° to minimize TM mode excitation. As can be seen, the overall sideband suppression is about 42 dB. The sawtooth and phase modulation amplitudes are 9.0 V and 2 π radians, respectively. Shown in Figure 1-2(b) is the result when the polarizer is set at 45° to excite equally both TE and TM modes. The sideband suppression is only slightly lower at 40 dB, thereby indicating the effectiveness of suppressing TM mode transmission. Comparable sideband suppression has been achieved for frequency shifts up to 40 kHz.

L.M. Johnson
C.H. Cox, III

1.2 PERFORMANCE AND REPRODUCIBILITY OF MACH-ZEHNDER INTERFEROMETER ARRAYS IN Ti:LiNbO₃ OPERATING AT WAVELENGTHS FROM 0.458 μm TO 3.39 μm

Integrated guided-wave optical devices formed from Ti:LiNbO₃ are being investigated for measurement and/or analog processing of optical wavefronts. An integrated optical device consisting of an array of interferometers and straight waveguides for wavefront measurement is the first such device whose performance has been evaluated.⁴ Concepts to vary the phase contour and/or to vary the intensity contour of the wavefront are under study. In analog processing, high

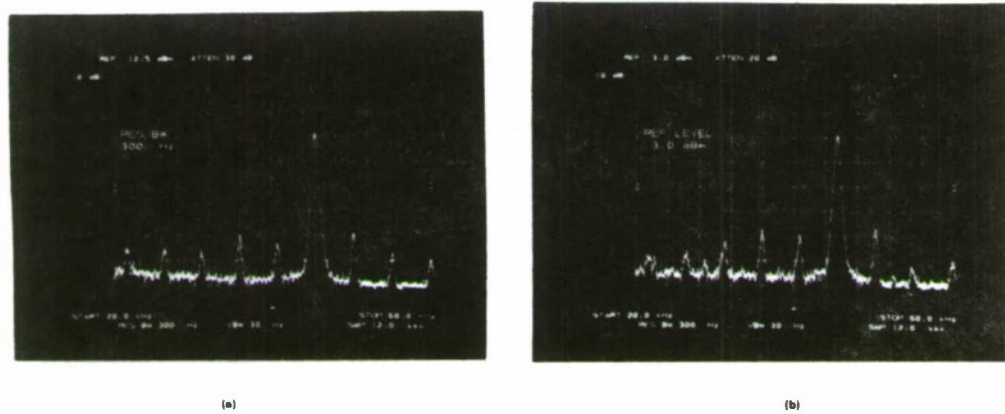


Figure 1-2. Experimental results obtained when $\Delta f_2 = 5 \text{ kHz}$ and $\Delta f_1 = 40 \text{ kHz}$ with input polarizer set at (a) 0° (TE excitation) and (b) 45° (both TE and TM excitation). The dominant component is at 45 kHz and the sideband spacing is 5 kHz .

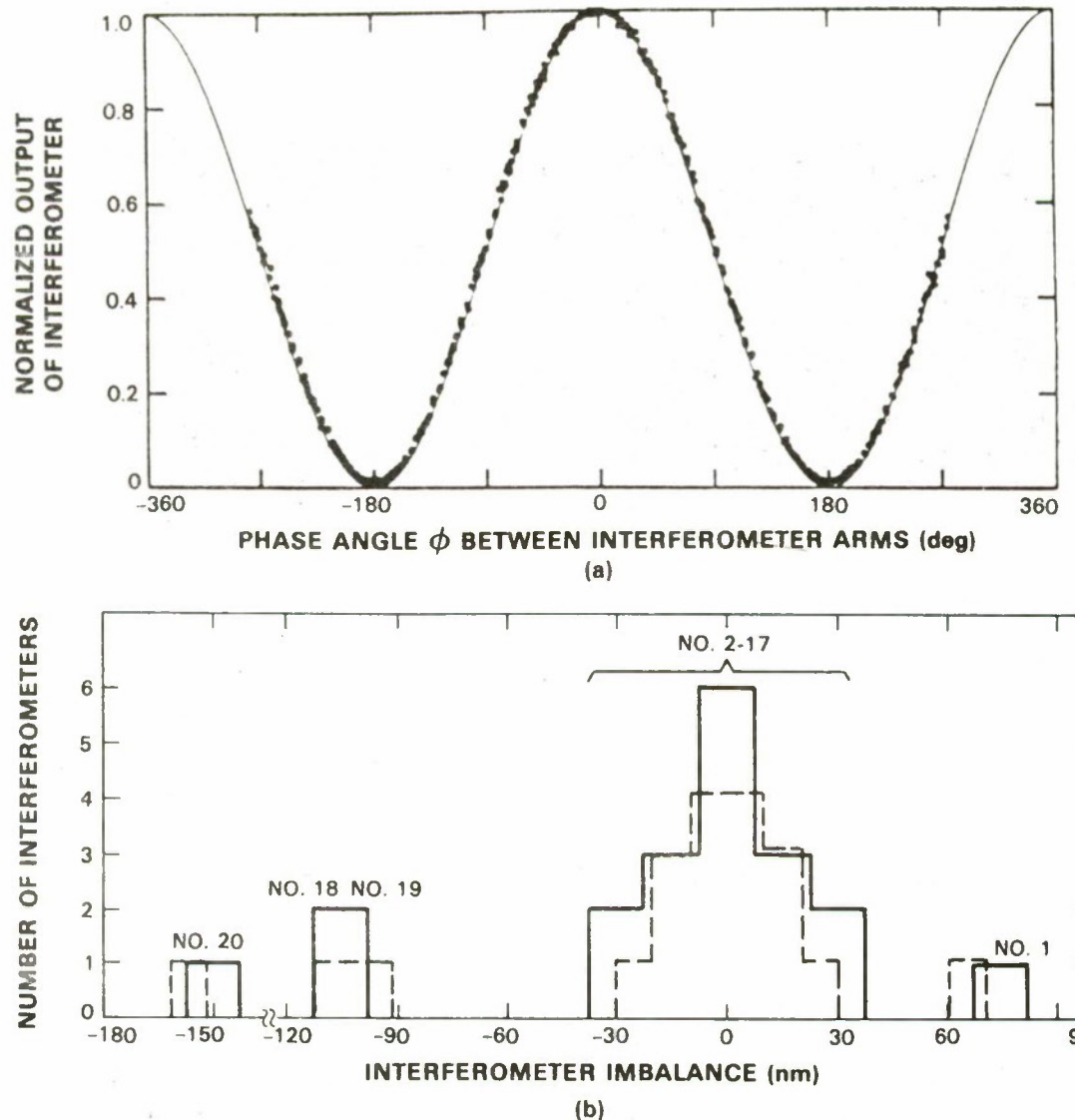
accuracy in the output (up to three significant figures) is desirable, thus uniformity and reproducibility are of paramount importance. The uniformity and reproducibility obtained for wavefront measurement sensors is reported here. To show the applicability of Ti:LiNbO_3 for analog processing throughout its transparent range of $\approx 0.4\text{-}4.0 \mu\text{m}$, wavefront measurement sensors have been fabricated for GaAs lasers ($0.82 \mu\text{m}$), for infrared HeNe lasers ($3.39 \mu\text{m}$), and for argon lasers ($0.458 \mu\text{m}$).

In the simplified one-dimensional sensor presently being investigated, variations of intensity and phase along the wavefront are measured using an array of 20 straight guides (for intensity) and 20 Mach-Zehnder interferometers (for phase). Most of the experiments have been at the GaAs laser wavelength ($0.82 \mu\text{m}$), where a wavefront sensor consisting of a Mach-Zehnder interferometer using discrete optical components is commercially available.⁵ The integrated optics sensor^{4,6} has advantages in performance and simplicity of construction over the sensor now available.

For equal illumination of the waveguides, the interferometer output power is given by

$$P_\phi = 2BP \cos^2 \left(\frac{\phi + \phi_0}{2} \right) , \quad (1-1)$$

where P is the output power of the straight waveguide. Experimentally, a planar wavefront was tilted to vary the phase difference ϕ between the two arms of the interferometer. Figure 1-3(a) shows the comparison of the experimental results with the theory of Equation (1-1). The results have been normalized to compensate for variations of up to 20% in the loss factor B from



154877-N-02

Figure 1-3. (a) Performance of 20-interferometer array with incident 0.82- μm radiation and a readout using a silicon imaging CCD. The outputs at the 'nulls' at $\pm 180^\circ$ are due to crosstalk in the CCD designed for the visible. The curves have been shifted in phase so the maxima for the interferometers occur at 0° . (b) Histogram of the imbalance in the lengths of the arms of each interferometer obtained from the above shift in ϕ (solid line). The number of the interferometer in the array is noted. The dashed lines are data taken nine months earlier and plotted with a slightly higher resolution on a different array. The two arrays were fabricated with the same photomask.

interferometer to interferometer. Techniques such as using input antennas will reduce the variations.⁷ These variations are reproducible from run to run and therefore can be reduced significantly by computer post-processing.

The value of the phase bias ϕ_0 in Equation (1-1) depends on the imbalance in the lengths of the arms of the interferometers. The curves in Figure 1-3(a) have been shifted in phase so all the maxima occur at 0° . From this shift, ϕ_0 and thus the equivalent length imbalance has been determined. Figure 1-3(b) shows the imbalance for the data of Figure 1-3(a) and for data obtained nine months earlier. For these earlier data, a different GaAs laser, a different array, and a different output detection scheme were used. Only the mask used to fabricate the two integrated-optics arrays was the same. The remarkable agreement in the imbalance illustrates the reproducibility of the integrated-optics components. Devices tested over a two-year time span have shown no change in this imbalance in interferometer arm lengths, which can be easily compensated for by putting electrodes across one arm and using the electro-optic effect, or by computer post-processing.

Wavefronts at $\lambda = 3.39 \mu\text{m}$ have been measured by the integrated-optics measurement sensor. In Figure 1-4, data for a diverging beam are compared to the theoretical result for a point source 1.65 m from the interferometer input. These data are not corrected for the interferometer imbalances described above, which have an insignificant effect at $3.39 \mu\text{m}$.

Figure 1-5 shows results similar to those of Figure 1-3 for $\lambda = 0.458 \mu\text{m}$. In these first results, the maximum power output from any waveguide was 10^{-11} . No photorefractive effect has been observed at these powers. The outputs at the nulls at $\pm 180^\circ$ were due to preamplifier noise in the detection system. The extinction ratio, limited by this noise, was better than 17 dB.

R.H. Rediker
T.A. Lind

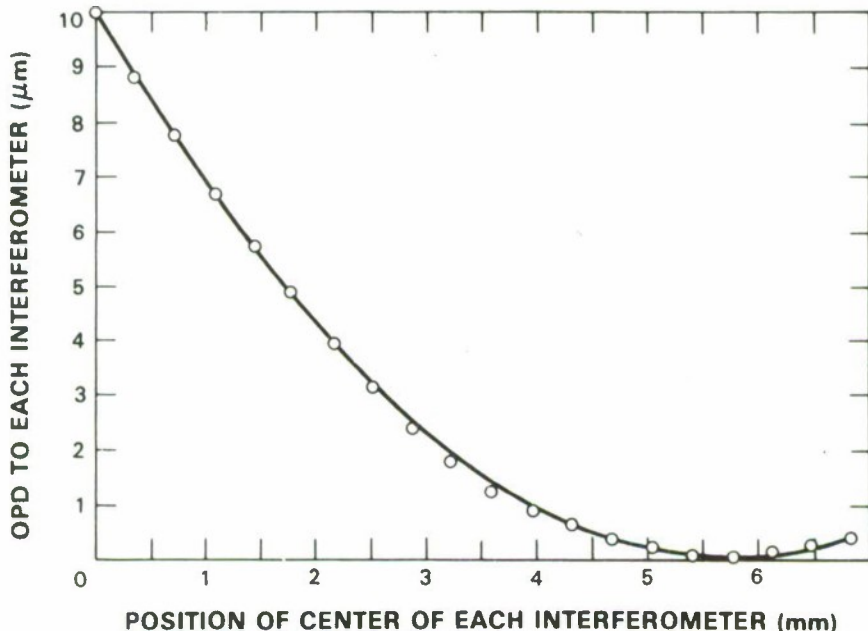


Figure 1-4. The optical path difference (OPD) measured by a 20-interferometer array with incident $3.39-\mu\text{m}$ radiation is compared with OPD expected (solid curve) for a beam diverging from a point source 1.65 m distant.

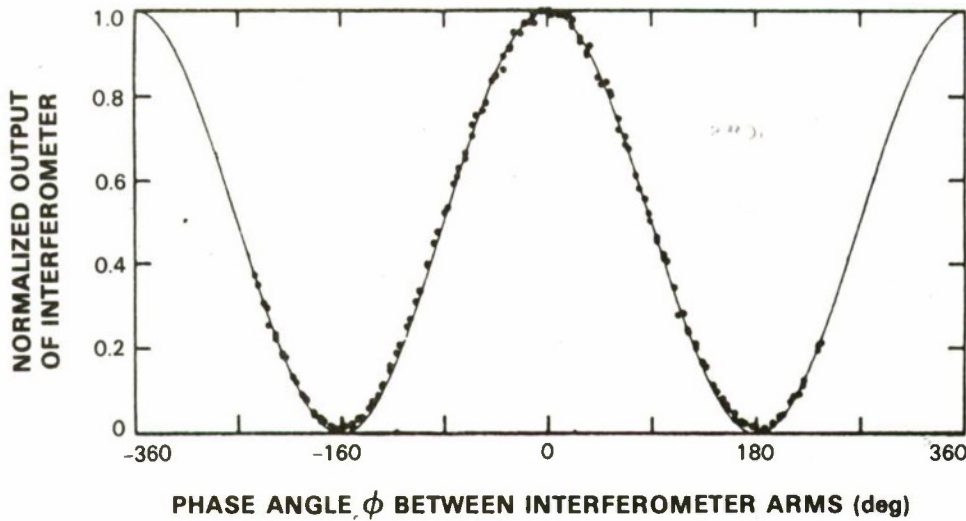


Figure 1-5. Performance of interferometer array at $0.458 \mu\text{m}$. The curves have been shifted in ϕ so the maxima for the interferometers occur at 0° .

1.3 SERIES RESISTANCE IN GaInAsP/InP BURIED-HETEROSTRUCTURE LASERS FABRICATED ON p-TYPE SUBSTRATES

Recent development⁸⁻¹⁰ of GaInAsP/InP buried-heterostructure diode lasers using p-InP substrates offers considerable advantages due to the large-area p contact, since the p contact is difficult to fabricate and has high specific contact resistance. In these devices, the total electrical resistance likely will be dominated by the spreading resistance in the p-InP, which has considerably higher resistivity than n-InP. In this work, the spreading resistance has been analyzed, and a simple formula has been derived that permits an accurate calculation.

The electrical current flow in the substrate of a p-InP substrate BH laser is illustrated in Figure 1-6 for a laser with a $100 \mu\text{m} \times 100 \mu\text{m}$ substrate cross section contacted at the bottom surface. In forward bias, current starts from the large-area p contact and flows into the narrow GaInAsP active layer (seen as a $2\text{-}\mu\text{m}$ -wide segment). The voltage distribution for this device geometry can be analyzed conveniently by using conformal mapping¹¹ from the simple case of current flowing from all directions into a slit. The latter is shown in Figure 1-7(a), where the equipotentials in the z plane ($z = x + iy$) are confocal ellipses given by

$$\frac{x^2}{\cosh^2 \Phi} + \frac{y^2}{\sinh^2 \Phi} = 1 \quad , \quad (1-2)$$

where Φ is the potential. The equipotential contours become nearly circular for $\Phi \geq 2$. In order to determine the equipotentials for our device geometry shown in Figure 1-6, we map the upper z plane into a strip in the upper w plane ($w = u + iv$) as shown in Fig. 1-7(b) using the coordinate transformation¹¹

$$z = \frac{\sin \frac{\pi w}{2s}}{\sin \frac{\pi W}{2s}} \quad , \quad (1-3)$$

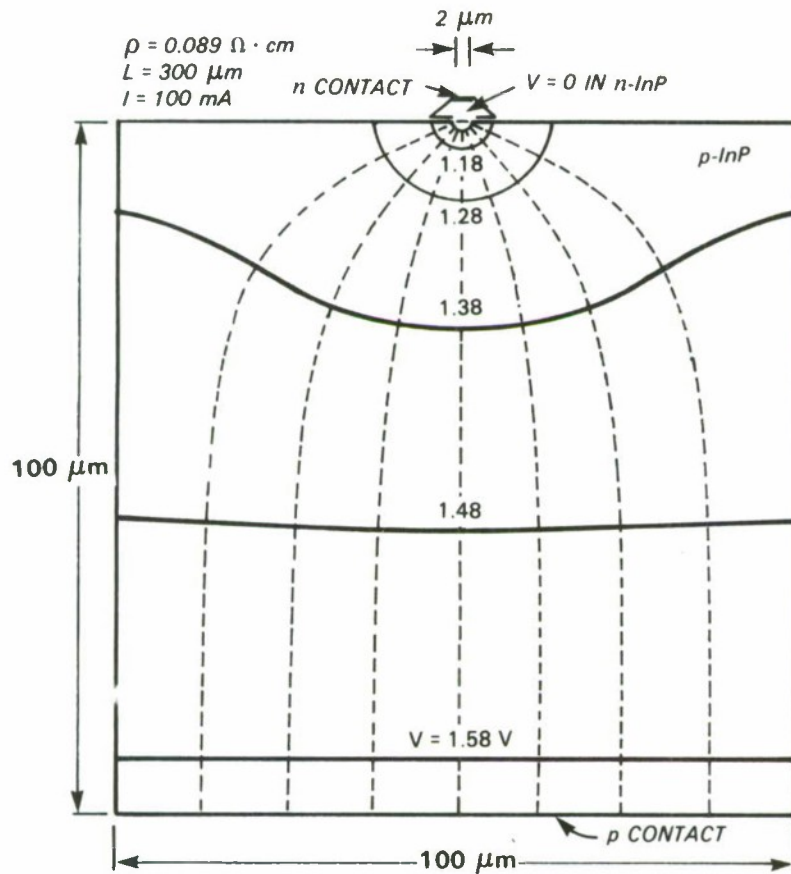


Figure 1-6. Calculated current and voltage distributions in a p-substrate GaInAsP/InP buried-heterostructure laser. The solid and dashed curves are the equipotentials and streamlines, respectively. The equipotentials are shown in voltage increments of 0.1 V. The junction voltage at the GaInAsP active region is 0.98 V.¹²

where W and s are the half widths of the active region and p substrate, respectively. By combining Equations (1-2) and (1-3), the potential $\Phi(u, v)$ is obtained, which then is converted into the voltage distribution $V(u, v)$ by¹²

$$V(u, v) = \frac{\rho I}{\pi L} \Phi(u, v) + V_Q , \quad (1-4)$$

where ρ is the resistivity of the p-InP, I is the current, L is the device length, and V_Q is the junction voltage at the quaternary active region. ($V_Q = 0.98$ V when the device is lasing.¹²) Note in Figure 1-7(b), that when $v \gtrsim s$, the equipotentials approach horizontal lines, and one of them will closely approximate the p contact, as shown in Figure 1-6.

To calculate the spreading resistance, only the voltage difference between the p contact and the quaternary active region needs to be evaluated. This can be done easily by considering only

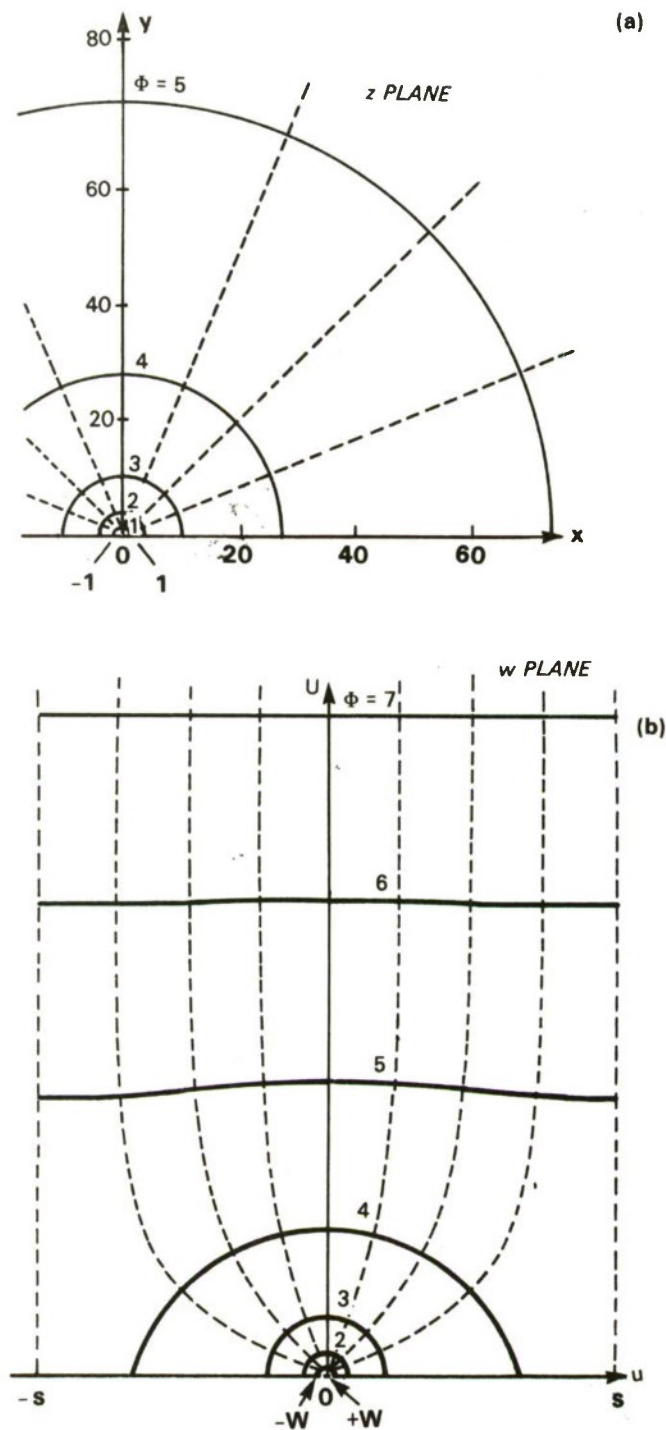


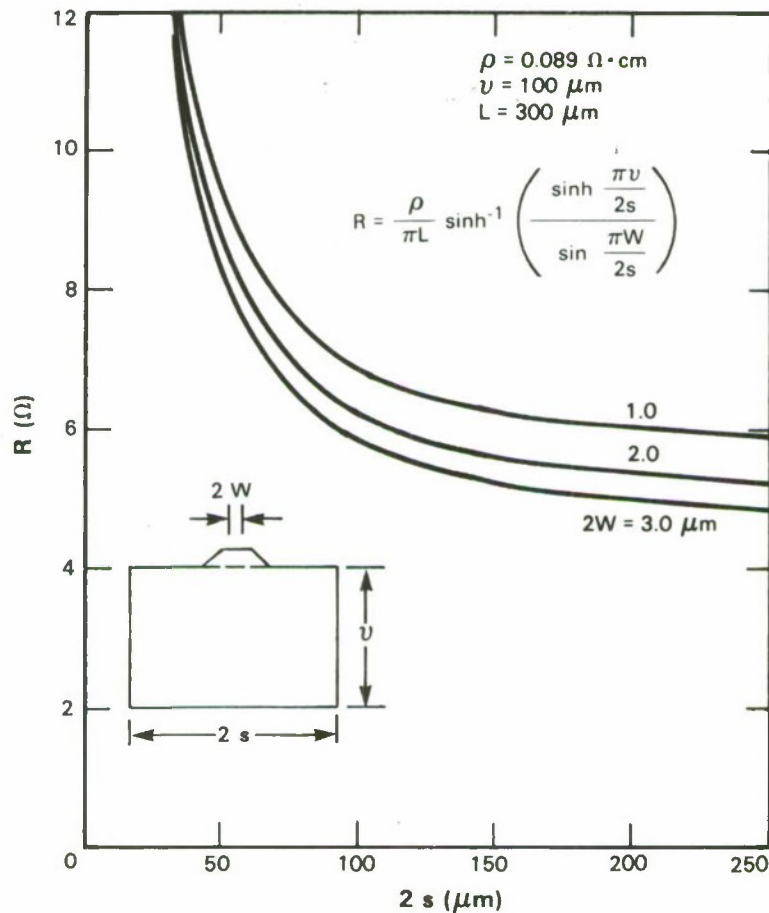
Figure 1-7. The conformal mapping used to calculate the current and voltage distributions in the p-substrate buried-heterostructure laser. The solid and dashed curves are the equipotentials and streamlines, respectively. Part (a) shows the simple case of current flowing (uniformly from all directions at infinity) into a slit that is maintained at a constant potential of $\phi = 0$.

the transformation [Equation (1-3)] along the imaginary axes and by noting that $\Phi = \sinh^{-1}y$ when $x = 0$. Thus, the spreading resistance is given by

$$R = \frac{\rho}{\pi L} \sinh^{-1} \frac{\sinh \frac{\pi v}{2s}}{\sin \frac{\pi W}{2s}} \quad (1-5)$$

[Note that $\sinh^{-1}y$ can be conveniently expressed as $\ln(y + \sqrt{y^2 + 1})$.] Equation (1-5) correctly reduces to $R = \rho v / 2sL$ when $W = s$.

Equation (1-5) allows for a direct computation of the spreading resistance R from the device geometry and the resistivity. Figure 1-8 shows that R varies slowly with $2s$ until $2s \leq v$. For typical discrete devices, $2s \approx 200 \mu\text{m}$ and spreading resistances of 5-6 Ω are obtained from Figure 1-8 for active region widths of 1-3 μm and for $\rho = 0.089 \Omega \cdot \text{cm}$ (corresponding to a hole



158172-N

Figure 1-8. Calculated spreading resistance for the p-substrate, buried-heterostructure laser as a function of the device geometry.

concentration of $1 \times 10^{18} \text{ cm}^{-3}$ with a hole mobility of $70 \text{ cm}^2/\text{V s}$). Our recent experimental values of the total device resistances were $\gtrsim 10 \Omega$, indicating that perhaps the contact resistances were not negligible. It is worth noting that with minor modifications Equation (1-5) also can be used to calculate the thermal resistance, provided that the device is mounted junction-side-up on a heatsink and that all the heat is generated near the active region.

In conclusion, a simple formula has been derived that permits an accurate calculation of the spreading resistance in p-substrate buried-heterostructure lasers. It is highly valuable in the device design and in minimizing the series resistance.

Z-L. Liau
J.N. Walpole
D.Z. Tsang

REFERENCES

1. J.L. Davis and S. Ezekiel, Opt. Lett. **6**, 505 (1981).
2. L.M. Johnson, *Technical Digest of the Topical Meeting on Optical Fiber Sensors* (Optical Society of America, Washington, D.C., 1985), paper WBB4.
3. K.K. Wong, S. Wright, and R.M. De La Rue, *Technical Digest of the Topical Meeting on Integrated and Guided-Wave Optics* (Optical Society of America, Washington, D.C., 1982), paper WA5.
4. R.H. Rediker, T.A. Lind and F.J. Leonberger, Appl. Phys. Lett. **42**, 647 (1983).
5. J. Hayes and F. Lang, Proc. SPIE **429**, 22 (1983).
6. R.H. Rediker, T.A. Lind, and B.E. Burke, *Technical Digest of Conference on Laser & Electro-Optics*, p. 196 (1984).
7. R.H. Rediker, T.A. Lind, R.A. Becker, and L.M. Johnson, *Technical Digest of 7th Topical Meeting on Integrated and Guided Wave Optics* (Optical Society of America, Washington, D.C., 1984), paper WC4.
8. Y. Noguchi, Y. Suzuki, T. Matsuoka, and H. Nagai, Electron. Lett. **20**, 769 (1984).
9. Y. Nakano and Y. Noguchi, IEEE J. Quantum Electron. **QE-21**, 452 (1985).
10. D.C. Flanders, personal communication.
11. See, for example, W.R. Smythe, *Static and Dynamic Electricity*, 3rd ed., (McGraw-Hill, New York, 1968) Chpt. 4.
12. Z.L. Liau, J.N. Walpole, and D.Z. Tsang, IEEE J. Quantum Electron. **QE-20**, 855 (1984). .

2. QUANTUM ELECTRONICS

2.1 Ti:Al₂O₃ LASER EXPERIMENTS

Experiments are being carried out that are directed towards the development of a stable, widely-tunable Ti:Al₂O₃ master oscillator. A multiline Ar laser was used to optically pump a room temperature Ti:Al₂O₃ laser in a near concentric cavity consisting of two spherical mirrors ($R = 10$ cm) spaced by 18 cm apart. The front mirror, through which 70% of the radiation was injected using a 16 cm focal length lens, reflects nearly 100% in the 700-850 nm region. The back mirror couples out 1% in that region. The Ti:Al₂O₃ sample was 3.2 cm long, had antireflection (AR) coated surfaces, and had been used in previous laser experiments,¹ where room-temperature operation was obtained with a confocal cavity and a chopped pump beam with a 16% duty cycle.

In the present experiments, the use of the near concentric cavity resulted in the lowest laser threshold to date in a Ti:Al₂O₃ laser, corresponding to a 1.8 W of pump power incident on the crystal. About 120 mW was generated at 780 nm for a pump level of 6 W and 4.2% duty cycle. From the data in Figure 2-1, a slope efficiency of 2.8% is obtained. A slope power efficiency of 60% (86% slope quantum efficiency) previously had been measured for the same crystal under high excitation in pulsed experiments using a 30% output coupler. The difference in the two results could be due to the large difference in output coupling for the two experiments (1% versus 30%). However, this would imply a high value of about 10% for the internal losses, which is inconsistent with considerably lower values determined from relaxation oscillation transients.²

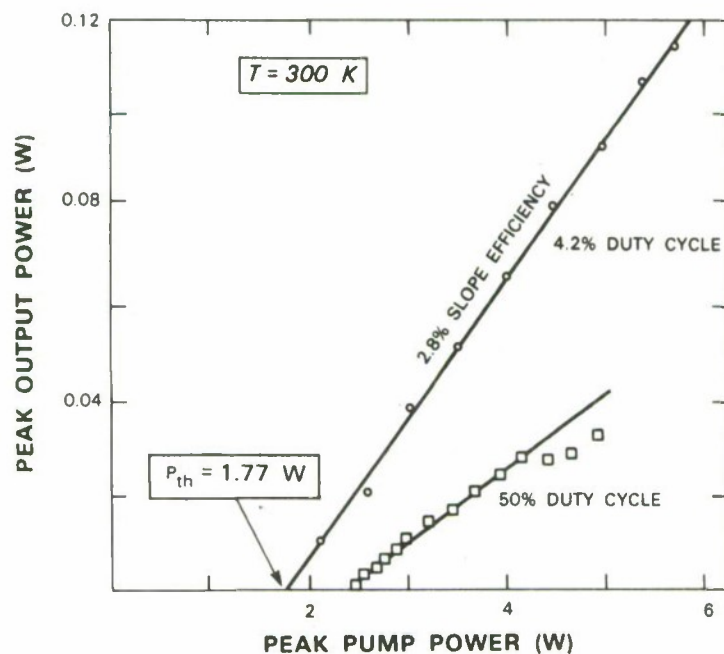


Figure 2-1. Peak output power of the Ti:Al₂O₃ laser vs argon-ion laser peak pump power incident upon the input face of the crystal at room temperature. The two curves correspond to two different duty cycles (4.2% and 50%, respectively) of the mechanically chopped pump beam.

An important reduction of the quantum efficiency is likely to arise from excessive heating of the active region during the pulse; this is being investigated. It should be noted that efficiency is not an issue in the master oscillator. It is, however, in a power amplifier, where, fortunately, it is less sensitive to internal losses. Power amplifier efficiency as high as that of the already demonstrated pulsed oscillator³ can be expected.

True CW laser operation previously had been achieved in an experiment¹ where the Ti:Al₂O₃ crystal was cooled down to 80 K. In the present experiment, operation at a 50% duty cycle was achieved at room temperature, although at reduced laser output, as shown in Figure 2.1. True CW operation was prevented by the temperature rise of the pumped region since nonradiative processes become important above room temperature. This temperature rise was even higher because of the poorer (over one order of magnitude) thermal conductivity of Al₂O₃ at 300 K when compared to that at 80 K. In future work, we expect to obtain CW lasing by using the higher quality (and hence lower laser threshold) Ti:Al₂O₃ material presently being developed and, if necessary, by operating somewhat below room temperature.

Insertion of a 100-μm-thick off-axis etalon in the laser cavity resulted in the appearance of a set of lasing frequencies whose spacing was determined by the etalon thickness. By tuning the etalon angle, the laser wavelengths were scanned across the relatively narrow free spectral range. Cavity modifications to achieve single frequency tuning across the entire gain bandwidth of the Ti:Al₂O₃ system are underway.

R. Aggarwal*
A. Sanchez

2.2 FAST ELECTRO-OPTICAL TUNING FOR A FREQUENCY-AGILE LASER SYSTEM

Fast tuning over a broad (about 20%) frequency range will be required for a master oscillator for a frequency agile laser system. Initial tuning experiments have been performed using a CW dye laser; this has permitted the development and evaluation of suitable intracavity tuning optics, which eventually will be transferred to a master oscillator using Ti:Al₂O₃.

Figure 2-2 shows a laser with an intracavity tuning element; while a dye jet is shown as the gain medium, the concepts to be discussed can be applied to other types of lasers with homogeneously broadened gain and well-defined polarization of the cavity modes.

Current experiments have employed a dye laser pumped by a multiline AR laser. The tuning optics of the dye laser (tilted plate Lyot filter) were removed and replaced with a commercial Pockels cell with AR coated windows, with the cell axis at an adjustable small angle (1-6 degrees) from the laser cavity axis.

* Author not at Lincoln Laboratory.

In this arrangement, the electro-optic cell works both as a mechanical tuning device (when the angle offset from the cavity axis is changed) and as a voltage-controlled tuning element with submicrosecond response time. The operation of the device can be understood by referring to Figure 2-3. With no applied voltage, the Pockels cell behaves as a uniaxial birefringent crystal with optic axis misaligned by θ from the direction of laser radiation propagation. Since the Brewster angle orientation of the jet forces the laser mode polarization to be vertical, the double-pass transmission of the cell for the vertical E-field component determines the amount of roundtrip feedback.

156018-N-01

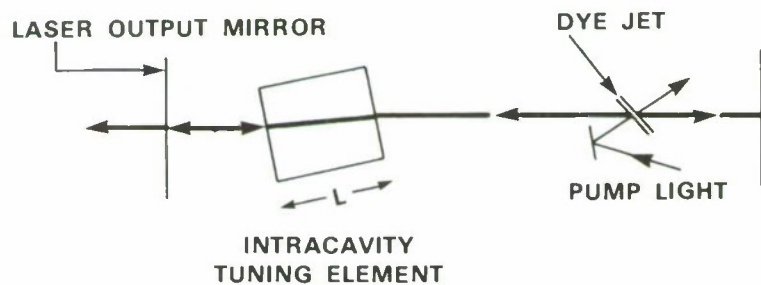


Figure 2-2. Tunable laser cavity.

146688-N-03

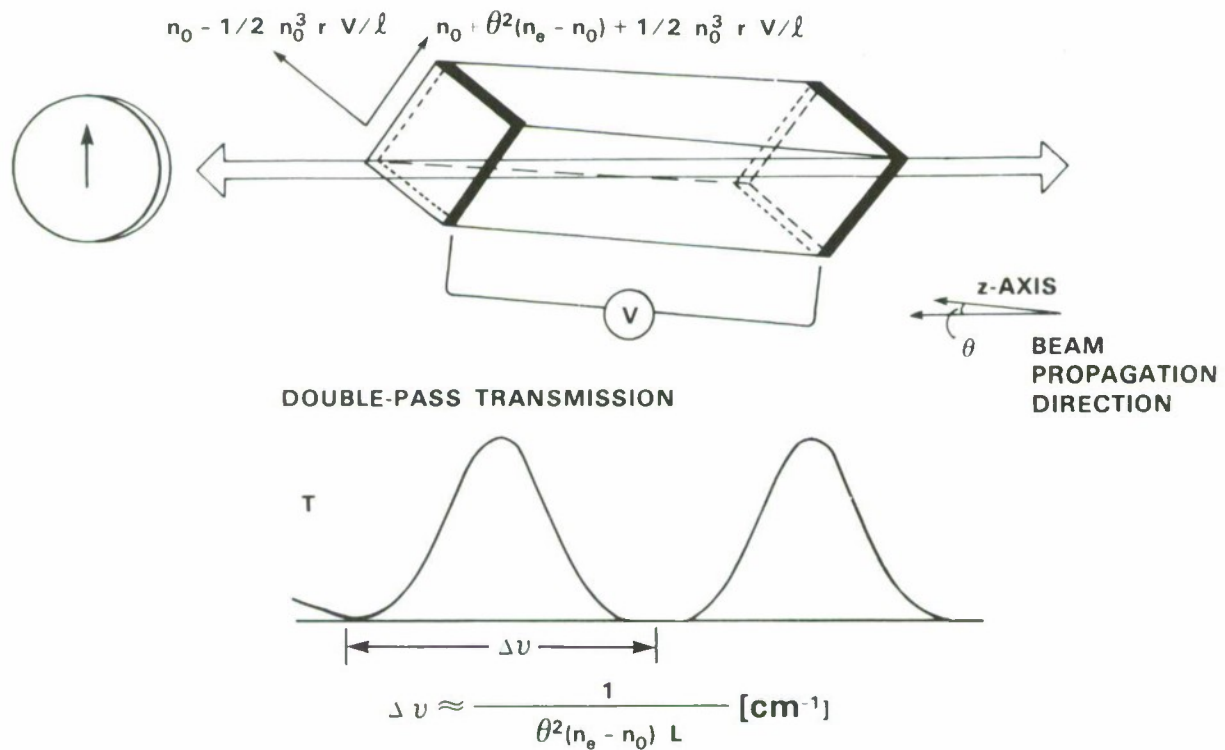


Figure 2-3. Principle of operation of the electro-optic tuning device.

With the geometry of Figure 2-3, the cell transmission is wavelength dependent with maxima (100%) satisfying the condition

$$\Delta nL = m\lambda/2 ,$$

where m is an integer and Δn is the difference between the refractive indices for the E-field components along the directions indicated. Thus, Δn is proportional to the square of the angle θ for small angles.

When a voltage V is applied to the E-O cell, the (longitudinal) Pockels effect induces an additional birefringence, proportional to the voltage: the total birefringence is

$$\Delta n = (n_e - n_o)\theta^2 + n_o^3 r V/L ,$$

where r is the electro-optic coefficient of the cell crystal (KD^*P). Thus, the wavelength of maximum transmission depends on angle and voltage as follows:

$$\lambda = 2\Delta n L/m = 2(n_e - n_o)\theta^2 L/m + 2n_o^3 r V/m .$$

The choice of the order factor m is governed by the requirements of selectivity and necessity of having only one transmission peak fall within the laser gain curve. Values from 2 to 8 have been used in our experiments, which have confirmed the theory outlined above. As expected, even and odd values of m give output polarizations that differ by 90° .

The simple filter so far described is not selective enough to give single cavity-mode operation; use of additional intracavity optics will be necessary, one possibility being represented by off-axis etalons, which should also be tuned in track with the main element. However, the simple arrangement has allowed preliminary studies of transient tuning phenomena. Some results are shown in Figure 2-4; they can be interpreted as showing the wavelength-vs-time response of the tunable laser excited by a 400 V step function. Most of the 'ringing' appearing in the response can be attributed to piezoacoustic phenomena in the electro-optic crystal; these could be counteracted in several ways. The relatively low resolution in Figure 2-4 does not reveal the multimode structure of the laser spectrum; higher resolution studies will require the use of a more stable cavity and associated optics.

Further work is being done to design a system allowing the fast-tuning random access of a single cavity mode, with subgigahertz mode spacing; a demonstration of a spatially agile beam with the required resolution then will become feasible.

V. Daneu

2.3 FREQUENCY CONVERSION USING KTP

The study of the feasibility of achieving high-efficiency tripling of $1.645 \mu\text{m}$ laser radiation is continuing. It was noted in the preceding Solid State Technical Report⁴ that, of the commercially available materials for this application, KTiOPO_4 (KTP) is very promising and the various parameters involved in the frequency tripling of KTP were calculated. Now an experimental investigation of the frequency conversion capability and damage threshold properties of KTP has been started.

158173-N

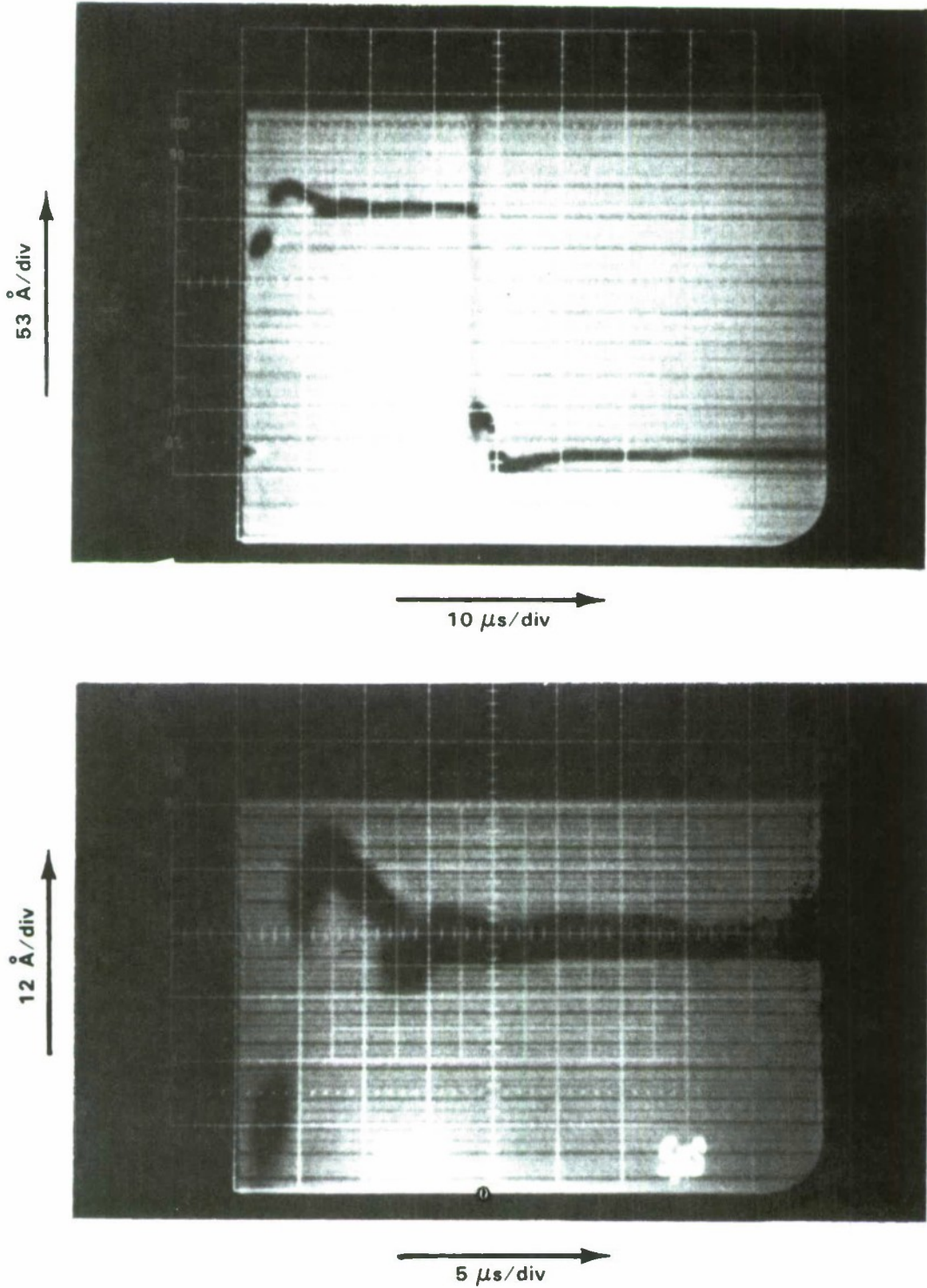


Figure 2-4. Wavelength-vs-time transient response of a laser driven by a 400 V pulse applied to the intracavity E-O tuning cell.

An Er:YAG laser radiating at $1.645 \mu\text{m}$, which is to be the eventual source at this frequency, was not available. Instead, a tunable CO:MgF₂ laser optically pumped by a pulsed $1.32-\mu\text{m}$ Nd:YAG laser was used. The Co:MgF₂ laser was tuned to $1.645 \mu\text{m}$ and experiments were carried out to characterize the laser output when operating in a Q-switched mode. The laser pulse shape was found to be near Gaussian, with a pulse length $\tau_p \sim 1 \mu\text{s}$. The Q-switched pulse energy from the Co:MgF₂ laser is limited to $\sim 10 \text{ mJ}$, necessitating the use of a relatively strongly focused beam to achieve the power densities required to obtain significant frequency conversion.

The frequency tripling is to be carried out in two steps; the first involves second harmonic generation (SHG) and the second involves summing the fundamental and frequency-doubled beams. Therefore, initial frequency conversion measurements were carried out with 5-mm-long crystal oriented for SHG phase matching in the yz crystal plane. The necessary power densities were obtained using lenses of local lengths $f = 20, 15$, and 10 cm . The SHG efficiencies obtained with the $f = 20$ and 15 cm lenses are shown in Figure 2-5 as a function of power density. The initial slope of $0.0525 \%/\text{mW}$, when corrected for Fresnel reflection at the crystal surfaces, corresponds to an internal efficiency slope of approximately $0.065 \%/\text{mW}$. A similar crystal oriented for phase matching in the xz crystal plane, by virtue of its larger d_{eff} value, would have an internal efficiency slope of $0.133 \%/\text{mW}$.

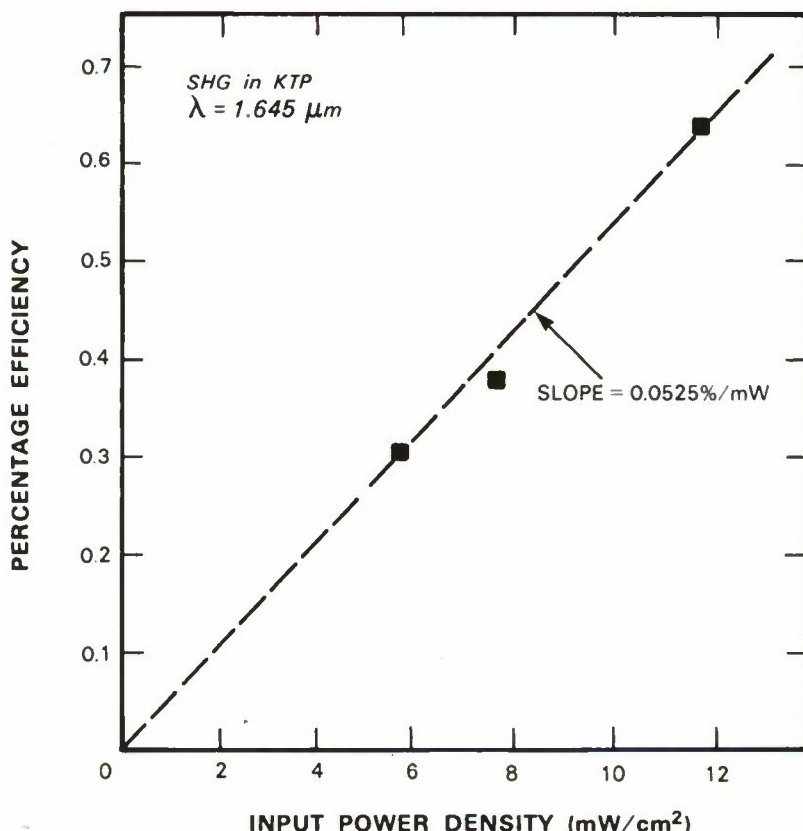


Figure 2-5. SHG in 5 mm KTP crystal as a function of input power density.

This value is far below the maximum efficiency slope predicted by the standard SHG equation, but is within $\sim 10\%$ of the value obtained by Liu et al.⁵ ($0.3\%/\text{MW}$ at $\lambda = 1.064 \mu\text{m}$ in a 3.9-mm-long crystal) when account is taken of the differences in wavelength, crystal length, and figure of merit.⁴

When the laser beam was focused onto the crystal with the $f = 10 \text{ cm}$ lens, the power density was approximately 35 MW/cm^2 , and damage was observed after two pulses. The damage occurred on the input surface, was circular with $100\text{-}\mu\text{m}$ diameter and shallow. In the work of Liu et al.⁵ damage occurred at 250 MW/cm^2 in an uncoated KTP sample subjected to a laser pulse of length $\tau_p = 15 \text{ ns}$. This result is consistent with a power density damage threshold that varies as $\tau_p^{-1/2}$, since this dependence leads to a predicted threshold of 31 MW/cm^2 for $\tau_p = 1 \mu\text{s}$. To establish if this damage threshold is consistent with that of other crystals, further study was carried out with a different KTP crystal, one that was not oriented for SHG from $1.645\text{-}\mu\text{m}$ radiation.

The results of the experiments showed that, as far as damage thresholds are concerned, variations between KTP samples are large and are significant even within a single crystal. Under these circumstances, the apparent accord in damage threshold with $\tau_p^{-1/2}$ noted above must be considered fortuitous. Further work with the crystal oriented for SHG will be carried out to establish if a similar variation in damage threshold occurs.

The present results appear to preclude the use of a single long (say, $\tau_p \sim 600 \mu\text{s}$) laser pulse to achieve efficient frequency tripling of $1.645 \mu\text{m}$ radiation in KTP.

An alternative approach is to operate with a long train of short pulses. This type of operation yields higher conversion efficiency for a given average input power level. The damage threshold of KTP irradiated with a pulse train of this nature remains to be evaluated, and a Nd:YAG laser operating in this manner will be set up.

N. Menyuk

REFERENCES

1. P.F. Moulton, Solid State Research Report, Lincoln Laboratory, MIT (1983:3), pp. 17-18.
2. P.F. Moulton, A. Mooradian, and T. Reed, Opt. Lett. 3, (1978).
3. P.F. Moulton, private communication (to be published).
4. Solid State Research Report, Lincoln Laboratory MIT (1985:3).
5. Y.S. Liu, L. Drafal, D. Dentz, and R. Belt, "Nonlinear Optical Phase-Matching Properties of KTiOPO_4 ," General Electric Technical Report No. 82CRD016 (February 1982).

3. MATERIALS RESEARCH

3.1 GROWTH AND CHARACTERIZATION OF Ti:Al₂O₃ CRYSTALS

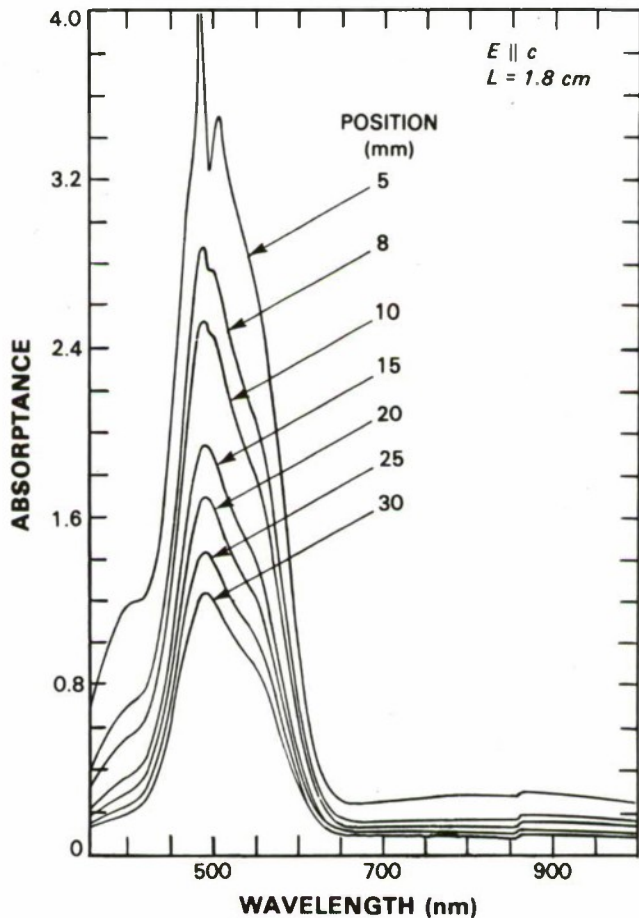
The broad wavelength tunability of the Ti:Al₂O₃ solid state laser, which has been operated over the range from 660 to 986 nm, makes this laser of interest for a number of applications. In order to provide high-quality Ti:Al₂O₃ containing various Ti⁺³ concentrations for use in laser studies, we have developed a thermal-gradient-freeze technique for growing single crystals of this material. A charge of sapphire crackle and single-crystal Ti₂O₃ is placed in a tapered tungsten crucible that ends at the bottom in a closed capillary containing an oriented sapphire seed. A tungsten cap then is spotwelded to the crucible at several points but not sealed. The crucible is placed in a furnace that has a cylindrical tungsten-mesh resistance heater enclosed in a water-cooled, stainless-steel jacket. Multilayer molybdenum heat shields are used for thermally insulating the heater and the crucible. The crucible is cooled from the bottom by contact with the water-cooled base of the furnace, so that the temperature increases from the bottom to the top of the crucible. The furnace is evacuated, heated sufficiently to melt the charge, back-filled with Ar or He gas, and gradually cooled to room temperature, causing the melt to solidify slowly from the bottom up.

Seven Ti:Al₂O₃ single crystals, each weighing about 100 g, have been grown by the thermal-gradient-freeze technique from charges containing between 0.15 and 0.5 wt% Ti₂O₃. Figure 3-1 is a photograph of the most recent crystal, which was grown in a He atmosphere from a charge containing 0.5 wt% Ti₂O₃. The seed, which was oriented parallel to the optic (c) axis, has been removed from the bottom of the crystal. A number of gas bubbles (not visible in the photograph), which are clustered in a small region near the top of the crystal, appear to be the only significant internal imperfections.



Figure 3-1. Single crystal of Ti:Al₂O₃ grown by thermal-gradient-freeze technique from charge containing 0.5 wt% Ti₂O₃.

The relative Ti^{3+} concentrations in the crystals have been monitored by optical absorption measurements. In Figure 3-2, the absorptance values measured with a spectrophotometer at seven positions along the length of the crystal shown in Figure 3-1 are plotted as a function of wavelength from 350 to 1000 nm for light polarized parallel to the c axis. The band peaking near 490 nm is due to transitions between the 2T_2 lower level and 2E upper level of the single d-electron of the Ti^{3+} ion. The shoulder on the long-wavelength side of the band results from Jahn-Teller splitting of the doubly degenerate 2E level. The splitting at the peak of the band, which becomes sharper as the band becomes stronger, has not been observed before and is unexplained. The apparent absorption in the 700-900 nm range does not exceed 4% of the value at the peak. (For a different crystal, more accurate measurements made with a $Ti:Al_2O_3$ laser source have shown that the absorption in the 700-900 nm range is only about 1% of the peak value at 490 nm.)



158090-N-01

Figure 3-2. Absorptance spectra for light polarized parallel to the c axis, taken at seven positions along the length of the crystal shown in Figure 3-1.

The absorption coefficients (α) corresponding to the peak absorptance values for the spectra of Figure 3-2 are plotted in Figure 3-3 against the distance from the top of the crystal. The value of α increases with distance from the seed end, as a result of the increase in Ti^{3+} concentration due to normal segregation accompanying directional solidification. The maximum value, 5 cm^{-1} , which is believed to be the highest value of α so far obtained for $Ti:Al_2O_3$, corresponds to an estimated Ti_2O_3 concentration of 0.19 wt%. A similar variation in α with distance from the seed has been observed for the other crystals, and the values of α vary from crystal to crystal roughly in proportion to the concentration of Ti_2O_3 in the charge.

In connection with the $Ti:Al_2O_3$ crystal growth program, the solid solubility of Ti_2O_3 in Al_2O_3 has been determined by using x-ray diffractometer measurements to determine lattice spacing as a function of Ti_2O_3 concentration for samples annealed at temperatures between 1300 and 1750°C. The measured solubility increases from 0.44 m/o Ti_2O_3 at 1300°C to 2.9 m/o at 1750°C, the reported eutectic temperature for the Al_2O_3 - Ti_2O_3 system. These values, which correspond to a range from 0.62 to 4.1 wt% Ti_2O_3 , are in good agreement with those reported earlier by McKee and Aleshin¹ for 1600°C and 1700°C, but they are substantially higher than the solubilities reported by Roy and Coble² for 1400-1700°C.

R. E. Fahey
A. Sanchez

A. J. Strauss
M. M. Stuppi

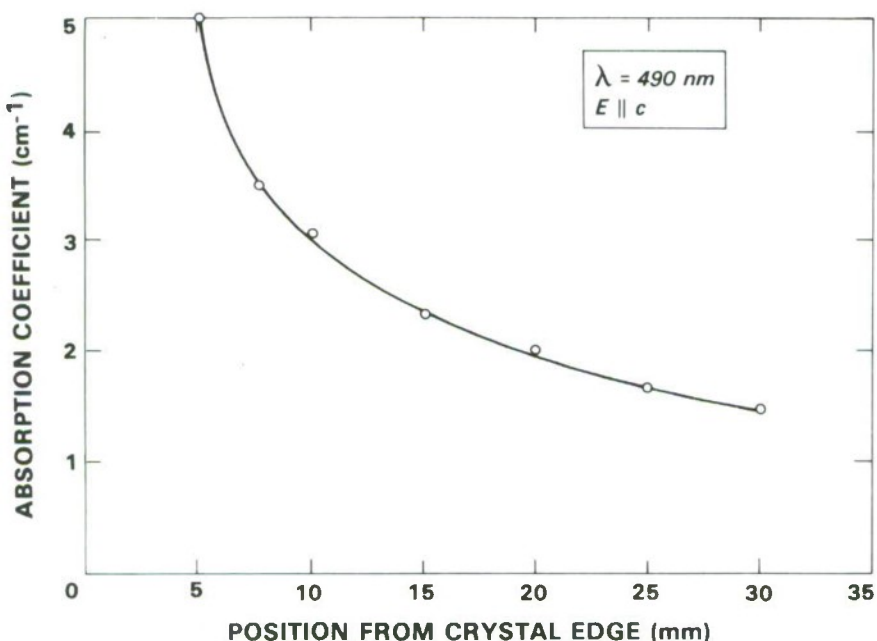


Figure 3-3. Absorption coefficient corresponding to peak absorptance for the spectra of Figure 3-2, plotted against distance from the top of the crystal.

3.2 MONOLITHIC INTEGRATION OF GaAs MESFETs AND Si MOSFETs

Monolithic GaAs/Si (MGS) integration has the potential for achieving substantial improvements in VLSI performance by complementing Si circuits with GaAs/AlGaAs optoelectronic components and high-speed electronic circuits. We previously have reported the fabrication of GaAs MESFETs,³ GaAs optical MESFETs,⁴ and GaAs/AlGaAs diode lasers^{5,6} on MGS substrates. We now have fabricated both GaAs MESFETs and Si MOSFETs on such a substrate.

The device processing steps are shown in Figure 3-4. First, Si MOSFETs are fabricated (except for contact openings and final metallization) on selected regions of a Si wafer. Chemical vapor deposition then is used to cover the entire wafer with layers of SiO_2 and Si_3N_4 to protect the MOSFET structures during GaAs epitaxy and MESFET processing. Openings are etched in the $\text{SiO}_2/\text{Si}_3\text{N}_4$ to expose the bare Si surface in the areas where GaAs devices are to be fabricated. Molecular beam epitaxy is employed to deposit a series of GaAs layers over the entire wafer, yielding single-crystal GaAs where the Si has been exposed and poly-GaAs elsewhere. The conventional recessed gate process is used to fabricate GaAs MESFETs in the single-crystal

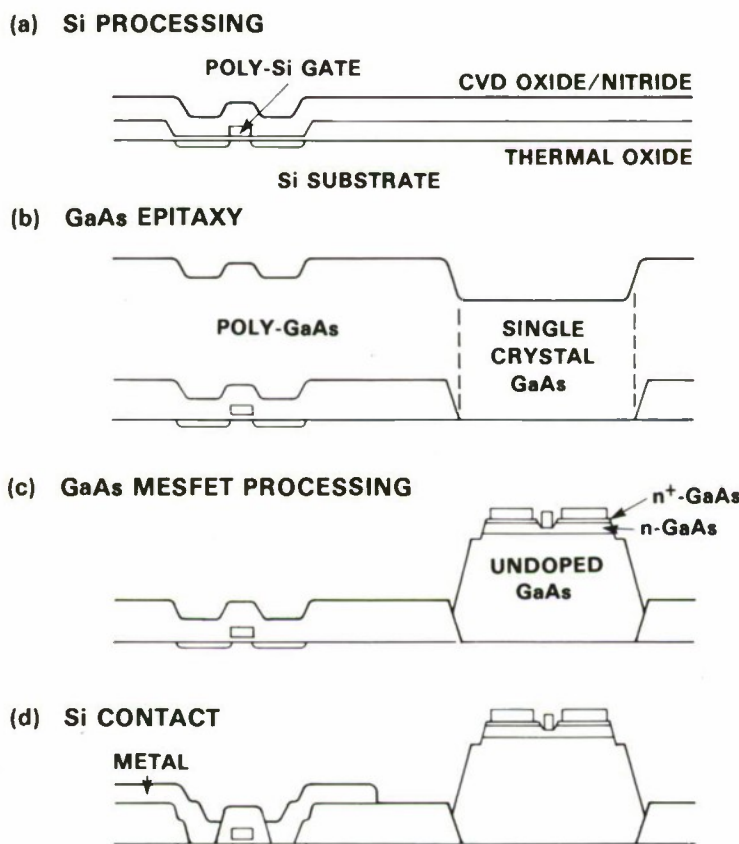


Figure 3-4. Processing steps for monolithic integration of Si MOSFETs and GaAs MESFETs.

regions, and the poly-GaAs is etched away to expose the $\text{SiO}_2/\text{Si}_3\text{N}_4$. Contact openings for the MOSFETs are etched in the SiO_2 , and final metallization is performed to complete fabrication.

Figure 3-5 shows an optical micrograph of a completed GaAs MESFET and an adjacent Si MOSFET. The gate lengths of the GaAs and Si devices are $1 \mu\text{m}$ and $5 \mu\text{m}$ respectively, and the gate width is $40 \mu\text{m}$ for both devices. The GaAs MESFETs have well behaved characteristics, as shown on the left side of Figure 3-5, with transconductance of about 150 mS/mm and output conductance of about 3.5 mS/mm . The gate Schottky diodes have a breakdown voltage of more than 10 V and negligible leakage current. The Si MOSFETs exhibit normal characteristics, as shown on the right side of Figure 3-5, with transconductance of about 19 mS/mm for a gate oxide thickness of 800 \AA . These results demonstrate that the GaAs epitaxy and subsequent processing have little effect on Si device performance.

H. K. Choi
G. W. Turner
B-Y. Tsaur

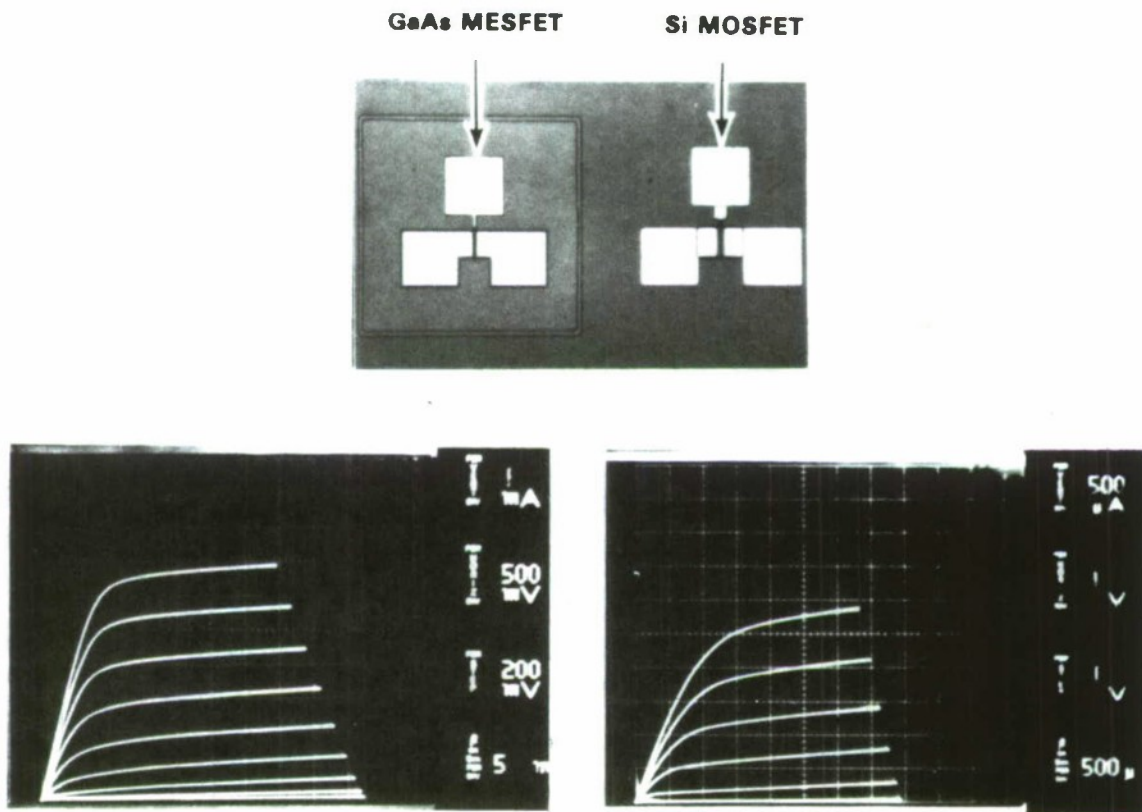


Figure 3-5. Optical micrograph of GaAs MESFET and adjacent Si MOSFET fabricated on the same GaAs/Si substrate, together with transistor characteristics for each device.

3.3 PICOSECOND PHOTODETECTORS FABRICATED IN HETEROEPITAXIAL GaAs LAYERS

One of the major applications proposed for monolithic GaAs/Si (MGS) integration is the fabrication of high-data-rate optical interconnects utilizing GaAs/AlGaAs optoelectronic components for intra- and interchip communication between Si circuits. In an earlier attempt to develop GaAs photodetectors for this application, we fabricated optical MESFETs in GaAs layers grown by molecular beam epitaxy (MBE) on Si wafers.⁴ The fastest of these devices had rise and fall times of ~ 5 and ~ 10 ns. We now have fabricated MGS GaAs photoconductive detectors with response times of ~ 60 ps. In addition, we have made similar detectors with response times of only ~ 40 ps in GaAs layers grown on silicon-on-sapphire (SOS) wafers. The latter are the first reported devices in the monolithic GaAs/SOS (MGSOS) material system, which offers the advantages of optical transparency, electrical isolation, and improved mechanical strength.

Photoconductive detectors with two different geometries were fabricated in undoped GaAs layers grown by MBE on commercial Si and SOS wafers. Detectors of one type have interdigitated contacts with 4- μm gaps, which were fabricated by using a photolithographic liftoff technique to pattern an evaporated, nonalloyed Au film 0.2 μm thick. These detectors were packaged in grooved alumina substrates, and Au ribbon was used to bond the contacts to RF connectors. The detector response was measured by using the system shown schematically in Figure 3-6. A diode laser emitting at 0.86 μm was driven by a comb generator to produce a train of ~ 50 ps infrared pulses that were focused on the gap region of the biased detector, and the RF output of the detector was fed directly into the $50\text{-}\Omega$ input of a sampling oscilloscope. It is estimated that this system can measure detector response times down to ~ 50 ps (FWHM).

The second detector geometry was used in making measurements on MGSOS devices by the correlation technique of Auston,⁷ which can measure shorter response times. The geometry and measurement scheme are shown schematically in Figure 3-7. Dual detectors, each with a linear gap of 4 μm , were fabricated on a square MGSOS wafer 1.3 cm on a side. The active areas of the detectors were defined by Au microstrip transmission lines patterned by the liftoff process used for the interdigitated detectors. (This design, which minimizes parasitic impedances, could not be used for MGS detectors because the MGS wafers were not strong enough to permit monolithic fabrication.) To make the correlation measurements, the pulsed output of a dye laser was split into two beams, one of which was chopped. The chopped beam was focused on one of the dual detectors, which was dc biased and acted as a signal generator. The unchopped beam was subjected to a variable delay and focused on the other detector, which acted as a sampling gate. The signal on the main transmission line then was measured with a lock-in amplifier synchronized to the chopping frequency, giving the correlated response of the detectors as a function of the delay time. It is estimated that our system can measure detector response times down to ~ 20 ps (FWHM).

Figure 3-8 shows the pulse response measured with the sampling oscilloscope system for a typical interdigitated MGS photoconductive detector. The FWHM response is ~ 60 ps, but there

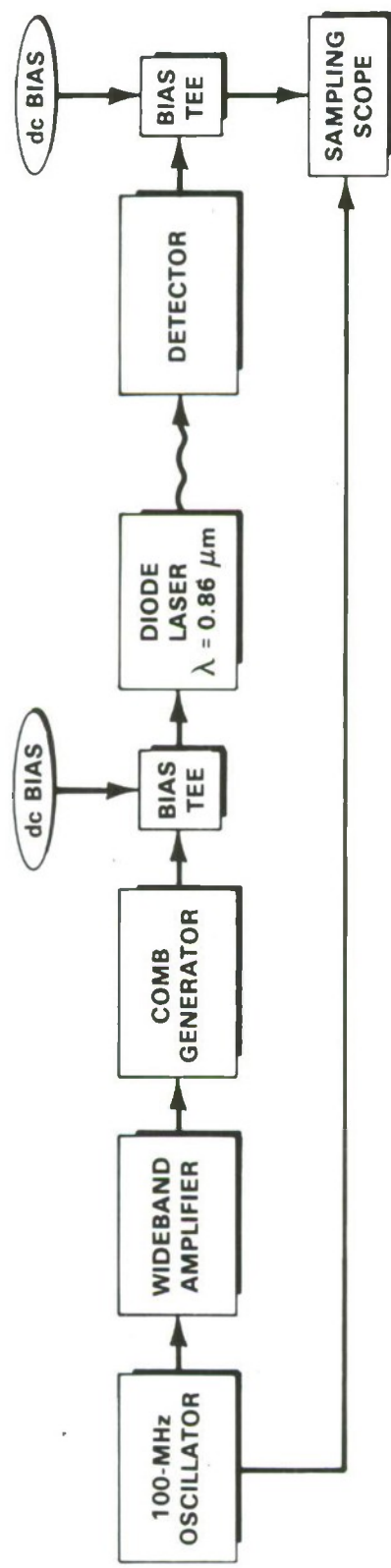


Figure 3-6. Sampling oscilloscope system for measuring photodetector response.

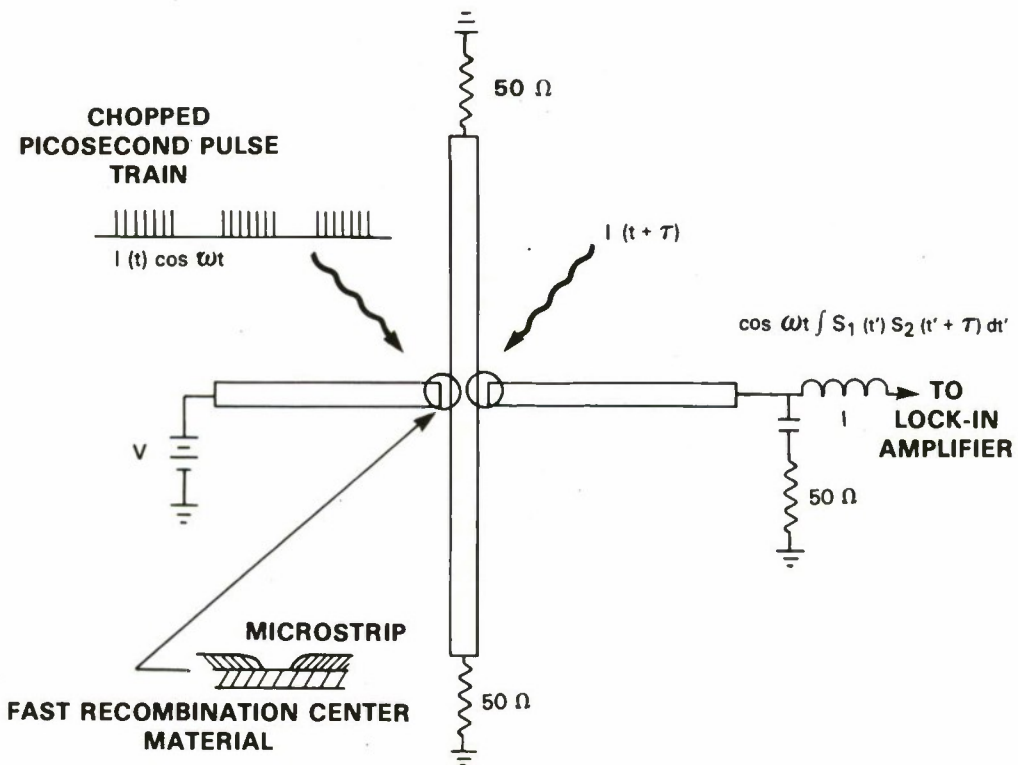


Figure 3-7. Correlation measurement system and dual detector configuration.

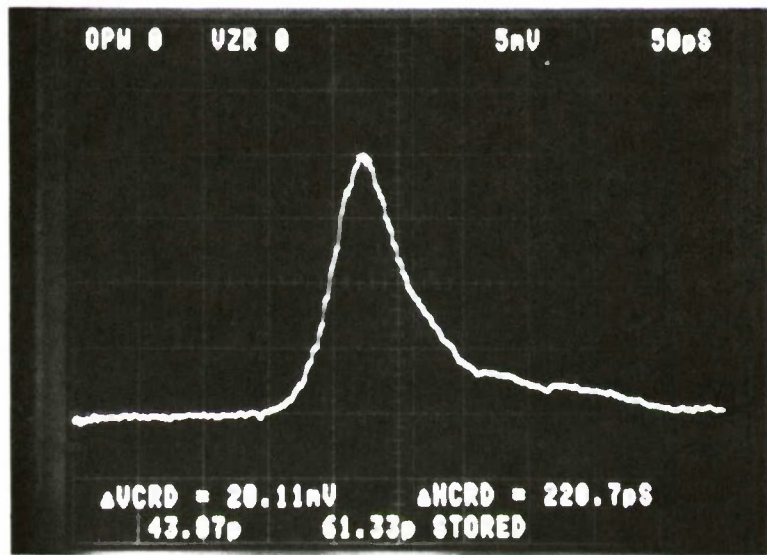


Figure 3-8. Pulse response of interdigitated MGS photodetector.

is a tail that persists for about 150 ps. Figure 3-9 shows the response measured with the same system for a typical interdigitated MGSOS detector. In this case, the response time is instrument limited at ~ 50 ps (FWHM), but there is no significant tail. For both MGS and MGSOS detectors, the response does not depend on bias voltage but is sensitive to the distribution of illumination in the gap region.

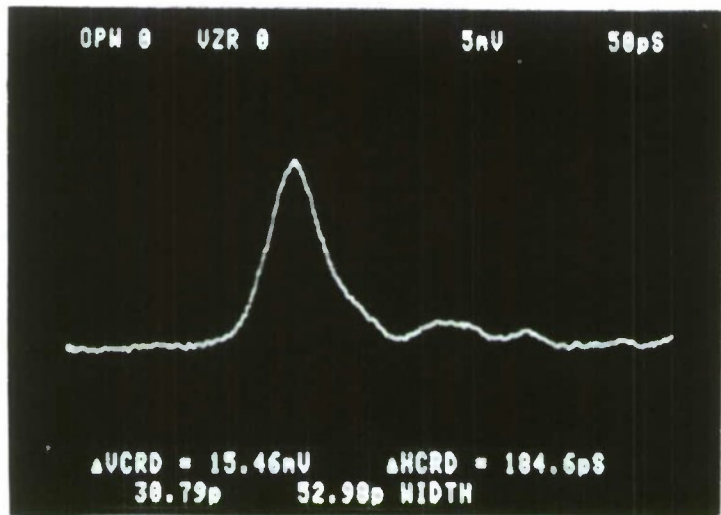


Figure 3-9. Pulse response of interdigitated MGSOS photodetector.

The observation of a tail in pulse response for MGS detectors but not for MGSOS detectors indicates that the carrier lifetime is significantly longer for the GaAs layers grown on Si wafers than for those grown on SOS wafers. Such a difference in lifetime would not be surprising, since the defect density is expected to be greater in the GaAs-on-SOS layers because of the high defect density in SOS Si films.

Figure 3-10 shows the correlation peak measured for a monolithic pair of MGSOS detectors fabricated from the same wafer as the interdigitated detector for which data are shown in Figure 3-9. The FWHM of the correlation peak is ~ 80 ps, which corresponds to a response time of ~ 40 ps for the photodetectors if it is assumed that their response decays exponentially. The trace also includes a number of reflection peaks resulting from impedance mismatches.

We also have measured the responsivities of interdigitated MGS and MGSOS detectors. The measurements were made by comparing the current outputs of these detectors to the current output of a calibrated Ge photodiode when the devices were successively illuminated by the focused output of a He-Ne laser emitting at $0.633 \mu\text{m}$. At this wavelength, the responsivity of the Ge detector was $3.47 \times 10^{-1} \text{ A/W}$, and its quantum efficiency was 68%. At a bias level of 4.5 V, the measured responsivities of the MGS and MGSOS detectors were 3.53×10^{-2} and 1.40×10^{-2}

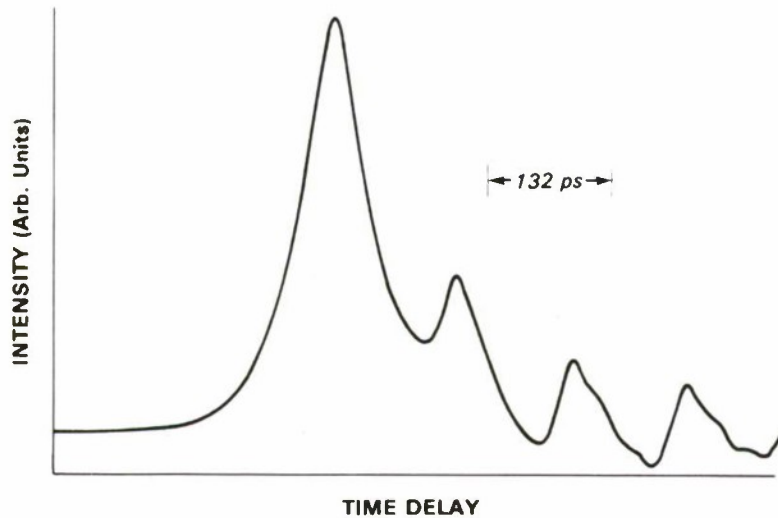


Figure 3-10. Correlation signal from monolithic pair of MGSOS photodetectors.

A/W, respectively, uncorrected for losses of approximately 50% due to contact shadowing and 40% due to reflection.

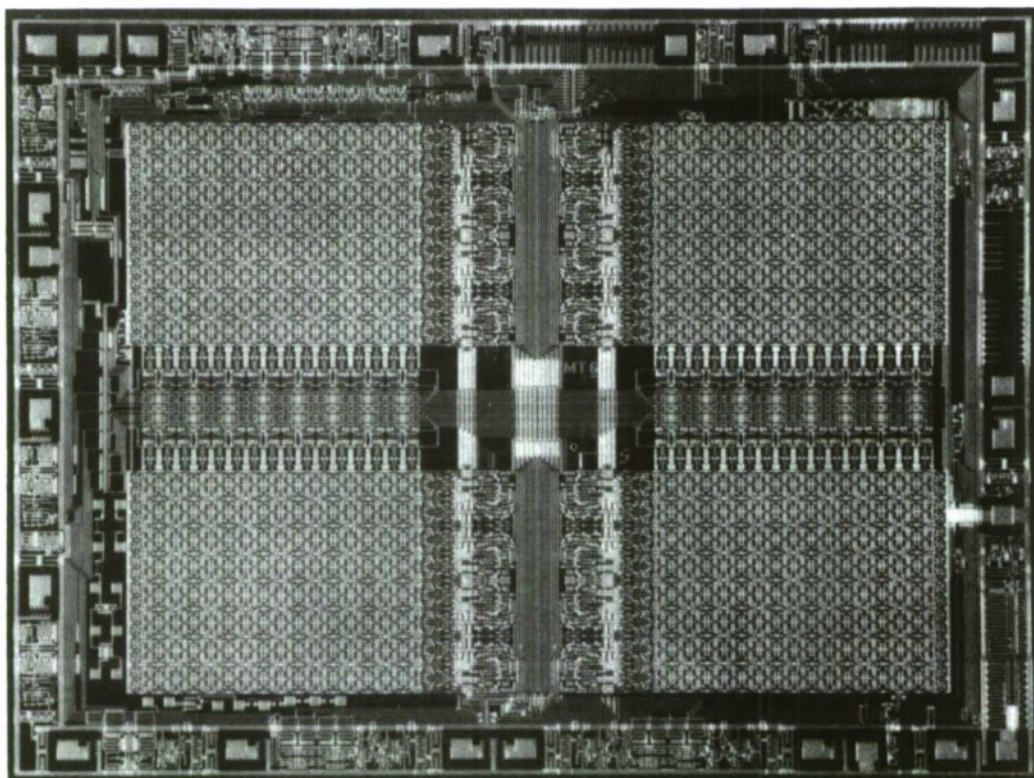
G. W. Turner	B-Y. Tsaur
G. M. Metze	H. Q. Le
V. Diadiuk	

3.4 STATIC RANDOM-ACCESS MEMORIES FABRICATED IN ZONE-MELTING-RECRYSTALLIZED SILICON-ON-INSULATOR FILMS

In the program to develop integrated circuit technology utilizing silicon-on-insulator (SOI) films prepared by the graphite-strip-heater technique for zone-melting recrystallization (ZMR), fully functional 1-K static random-access memories (SRAMs) have been fabricated in such films by a coplanar CMOS process. The SRAMs, which are organized in a 1024 by 1 configuration and contain $\sim 8,200$ transistors, are superior in speed performance to commercial bulk Si memories of similar configuration. These SOI memories are the first LSI circuits that have been fabricated in graphite-strip-heater ZMR films.

Three-inch SOI wafers with a 0.5- μm -thick ZMR Si film covering a 1.5- μm -thick SiO_2 film on the Si substrate were used in circuit fabrication, which is accomplished by a single-poly, single-metal process requiring a total of seven photolithographic masks. The main processing steps are as follows. Device isolation is achieved by a coplanar LOCOS process that involves partial etching of the Si film in the field region followed by complete oxidation of the thinned film to form the isolation oxide. For the p-channel transistors, a low-dose boron implant of $5 \times 10^{10} \text{ cm}^{-2}$ is used to form deep-depletion-mode devices; for the n-channel transistors, a deep boron implant of $2.5 \times 10^{12} \text{ cm}^{-2}$ is used to form enhancement-mode devices. The deep implant, which uses an ion energy chosen to locate the peak of the boron distribution near the lower

SiO_2/Si interface, also serves to suppress n-channel back leakage current. An additional boron implant is performed to increase the doping concentration near the edges of the n-channel transistors. This step, known as the channel-stop process, is used to suppress n-channel edge leakage current. A gate oxide with nominal thickness of 500 \AA is grown by thermal oxidation, followed by deposition of a $0.6\text{-}\mu\text{m}$ -thick poly-Si film that subsequently is doped with phosphorus by ion implantation and then patterned by wet etching. An unmasked boron ion implantation is performed for source-drain doping of the p-channel devices, and a selective phosphorus implant is used for source-drain doping of the n-channel devices. An oxide layer $\sim 0.4 \text{ }\mu\text{m}$ thick is formed by chemical vapor deposition and then densified by 900°C sintering, which also activates the implanted source and drain dopants. Contact openings are etched and Al-Si metallization is performed. Processing is completed by H_2 sintering and low-temperature oxide passivation. Figure 3-11 is a photograph of a completed SRAM chip, which measures about $3.8 \times 5.1 \text{ mm}$.



158178-N

Figure 3-11. CMOS I-K static random-access memory (SRAM) chip fabricated in zone-melting-recrystallized Si-on-insulator (SOI) film.

The memory chips are housed in standard dual-in-line ceramic packages and tested at room temperature using a Tektronix digital analysis system. The address, chip enable, and data output characteristics at a supply voltage of 5 V are shown for the read '0' and read '1' operations in Figure 3-12(a) and (b), respectively. For these operations, the chip-enable access times are 32 and 56 ns, respectively. For a commercial bulk CMOS memory (Harris HM6518) that is signal compatible with the SOI chips, the access time is typically 100 ns.⁸ Access time for the read '1' operation of an SOI SRAM is shown as a function of supply voltage in Figure 3-13. The circuit

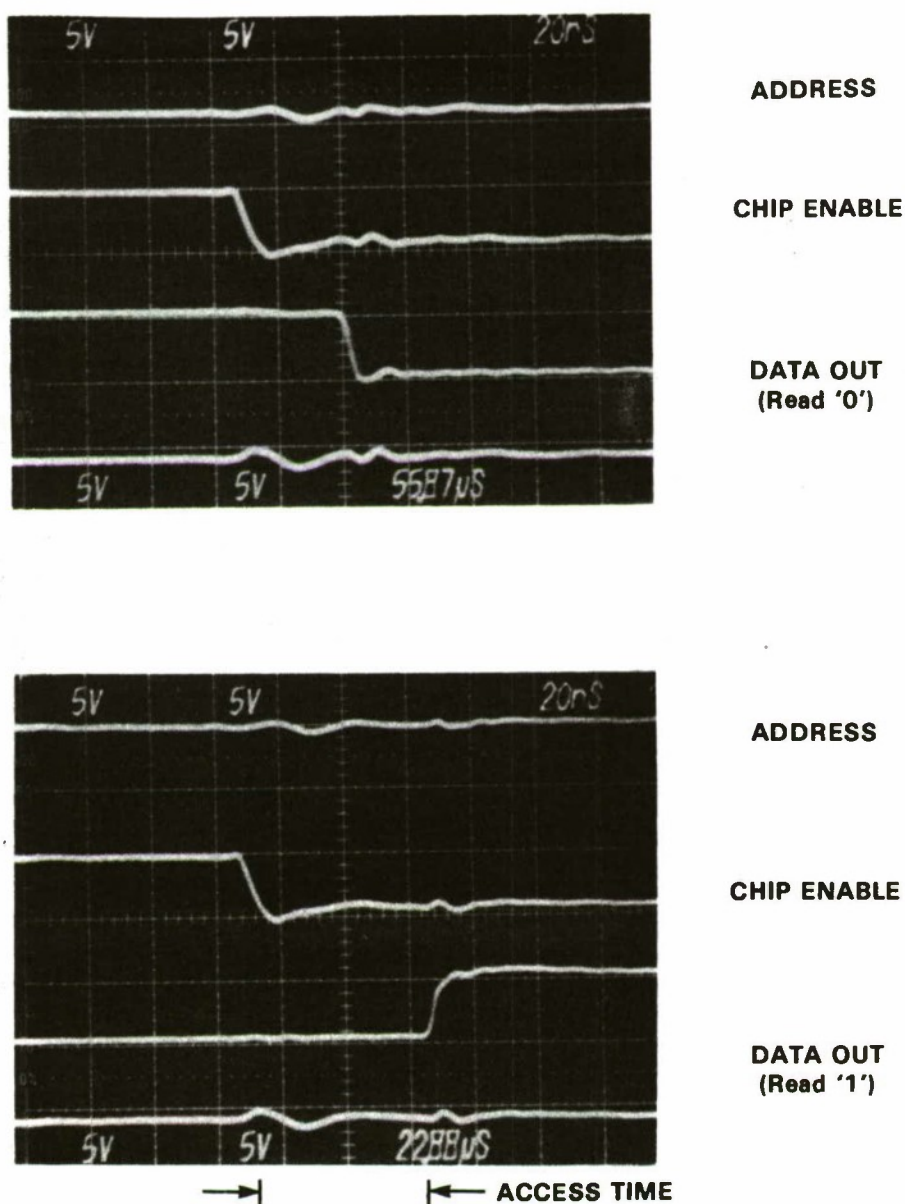


Figure 3-12. Characteristics of SOI SRAM for (a) read '0', and (b) read '1' operations.

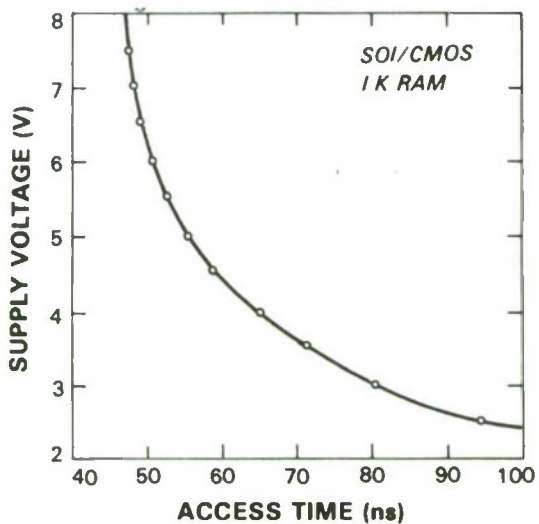


Figure 3-13. Chip-enable access time vs supply voltage for SOI SRAM.

operates over a supply voltage range from 2.5 V to 7.5 V, and the speed improves with increasing voltage. Several fully functional chips exhibiting 100% bit yield have been measured, although the majority of the chips contain a small percentage of nonfunctional memory cells.

B-Y. Tsaur
C.K. Chen
V.J. Sferrino

3.5 HIGH-EFFICIENCY DOUBLE-HETEROSTRUCTURE AlGaAs/GaAs SOLAR CELLS

Recent analyses have shown that higher efficiency solar cells (even though more expensive) have the potential for reducing the overall cost of photovoltaic systems. We previously reported⁹ a 22%-efficient shallow-homojunction GaAs cell with a GaAs/AlGaAs heterostructure back-surface field (BSF). We now have developed a new structure, suitable for both single-junction and tandem applications, that incorporates a shallow AlGaAs/GaAs heterojunction and a GaAs/AlGaAs BSF. Cells fabricated with this double heterostructure have exhibited global AM1 one-sun efficiencies as high as 23%.

The basic double heterostructure, shown schematically in Figure 3-14, consists of a p+ AlGaAs layer, a p GaAs base layer and an n+ AlGaAs emitter layer, with thicknesses of 0.5, 4.5-5, and 0.15 μ m, respectively, grown on a p+ GaAs substrate by organometallic chemical vapor deposition (OMCVD). Trimethylgallium, trimethylaluminum (TMAI), and arsine were the OMCVD source gases, and dimethylzinc and H₂Se were the dopant gases. The AlGaAs alloy composition was 20 mole percent AlAs. An n+ GaAs cap layer sometimes was used for ease of front contacting, and a p+ GaAs buffer layer always was employed to reduce the effects of substrate variations or defects on cell performance.

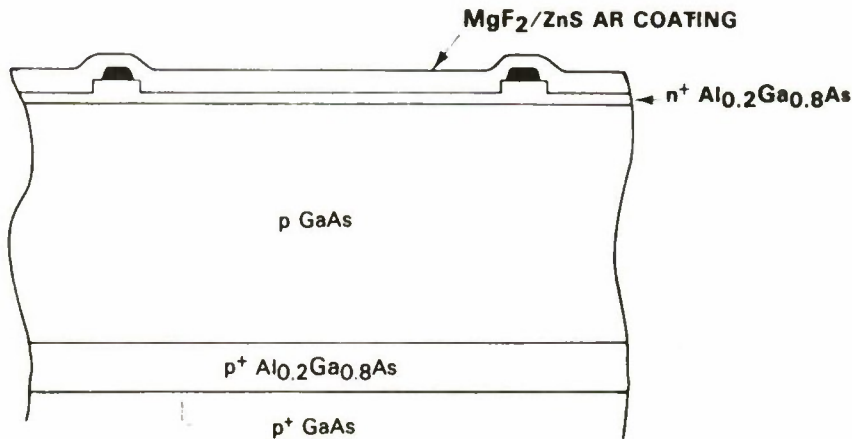


Figure 3-14. Schematic cross section of a double-heterostructure (DH) solar cell.

Cell fabrication techniques were similar to those used for GaAs shallow-homojunction cells.¹⁰ Fabrication was completed by depositing an antireflection coating of MgF/ZnS or MgF/TiO_x on the front surface. Current-voltage curves were measured under simulated AM1 global conditions using a rooftop calibration.¹¹

Figure 3-15 shows the I-V characteristic under simulated AM1 illumination for our best double-heterostructure (DH) solar cell at 25°C. For this cell, the open-circuit voltage V_{oc} is 1.05 V, the short-circuit current J_{sc} is 25.3 mA/cm², and the fill factor, ff, is 0.87, giving an AM1 one-sun efficiency of 23.1%. For our best single-heterostructure (shallow-homojunction, heterostructure-BSF) cell, $V_{oc} = 1.01$ V, $J_{sc} = 25.6$ mA/cm², and ff = 0.86; the AM1 efficiency is 22.2%.⁹ The improvement in efficiency for the DH cell is due to the increase in V_{oc} , which probably occurs because the higher-bandgap emitter contributes less to the dark saturation current.¹²

The external quantum efficiency values for the cell of Figure 3-15 are plotted as a function of wavelength in Figure 3-16. These efficiency values are equal to those obtained for single-heterostructure cells. Collection of current generated by absorption of long-wavelength photons is excellent, but the short-wavelength response indicates that the anticipated increase in current due to lower absorption in the AlGaAs emitter was not realized. It is expected that the short-wavelength response can be improved by optimizing the emitter characteristics.

To grow an n-AlGaAs/p-GaAs heterojunction requires the superposition of the n/p junction and the AlGaAs/GaAs metallurgical interface. In principle, this could be achieved by beginning the injection of H₂Se and TMAl simultaneously during OMCVD growth. It is known, however, that H₂Se exhibits a memory effect in GaAs OMCVD¹³ and has a greater gaseous diffusivity than TMAl. In addition, Se has a greater diffusivity in GaAs than Al.¹⁴ These effects tend to displace the np junction from the AlGaAs/GaAs interface.

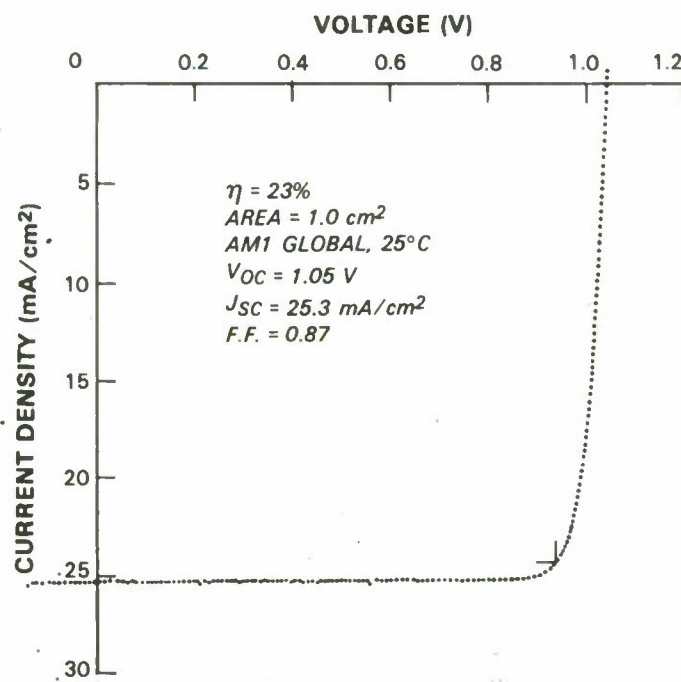


Figure 3-15. Current-voltage characteristic under one-sun simulated AM1 illumination for a DH solar cell.

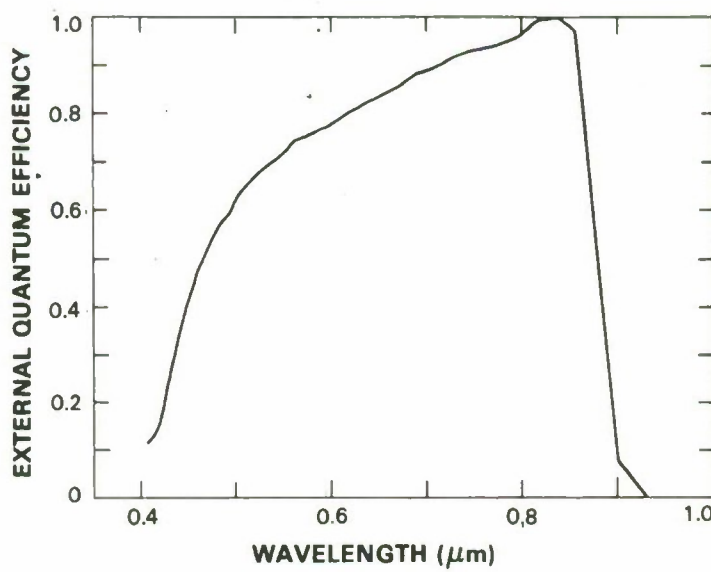


Figure 3-16. External quantum efficiency vs wavelength for the cell of Figure 3-15.

In preparing the initial DH solar cell wafer, we attempted to adjust for the above effects by delaying H₂Se injection for 10 s after beginning TMAl injection. Depth profiles of this wafer obtained by secondary-ion mass spectroscopy (SIMS) show that, in spite of this delay, Se initially was incorporated in the growing GaAs layer well before the start of AlGaAs deposition. In fact, the Se concentration became sufficient to convert the GaAs layer to n type, with the result that the wafer contains a GaAs homojunction rather than an AlGaAs/GaAs heterojunction.

In preparing a number of subsequent wafers, H₂Se injection was delayed for longer times. A heterojunction was obtained for delay times in the vicinity of 50 s, with shorter times yielding GaAs homojunctions and longer times yielding AlGaAs homojunctions. The ff values were greatest for cells fabricated from wafers with delay times in the heterojunction range but fell off sharply for longer delay times. The V_{oc} values, which were all in the range from 1.03 to 1.05 V, appear to be independent of delay time and thus of junction location. The cell of Figure 3-15 was fabricated from a wafer with a small estimated junction displacement.

For solar cells fabricated from a given material, it has been predicted¹⁵ that the normalized decreases in V_{oc} and efficiency with increasing operating temperature will be smaller for cells with higher V_{oc}. To test this prediction, I-V measurements were made on a DH cell and a shallow-homojunction, non-BSF cell at temperatures between 10°C and 80°C. At 25°C, V_{oc} was 1.04 V for the DH cell and 0.98 V for the homojunction cell. As predicted, the normalized decrease in V_{oc} was lower for the DH cell than for the homojunction cell. Since solar cells for flat-plate and concentrator applications are actually operated above 40°C and 80°C, respectively, this lower temperature dependence gives the DH cells a significant advantage.

R.P. Gale* G.W. Turner
J.C. C. Fan* R.L. Chapman*

* Author not at Lincoln Laboratory.

REFERENCES

1. W.D. McKee, Jr. and E. Aleshin, *J. Am. Ceram. Soc.* **46**, 54 (1963).
2. S.K. Roy and R.L. Coble, *J. Am. Ceram. Soc.* **51**, 1 (1968).
3. H.K. Choi, B-Y. Tsaur, G.M. Metze, G.W. Turner, and J.C.C. Fan, *IEEE Electron. Device Lett.* **EDL-5**, 207 (1984).
4. Solid State Research Report, Lincoln Laboratory MIT (1985:1), p. 26.
5. T.H. Windhorn, G.M. Metze, B-Y. Tsaur, and J.C.C. Fan, *Appl. Phys. Lett.* **45**, 309 (1984).
6. T.H. Windhorn and G.M. Metze, *Appl. Phys. Lett.* **47**, 1028 (1985).
7. D.H. Auston, "Picosecond Photoconductors: Physical Properties and Applications," in *Picosecond Optoelectronic Devices*, C.H. Lee, Ed. (Academic Press, New York, 1984).
8. *Harris Digital Data Book* (Harris Corporation, 1981), vol. 2, pp. 3-70.
9. R.P. Gale, J.C.C. Fan, G.W. Turner, and R.L. Chapman, in *Proceedings of the 17th IEEE Photovoltaic Specialists Conference* (IEEE, New York, 1984), p. 1422.
10. G.W. Turner and M.K. Connors, *J. Electrochem. Soc.* **131**, 1211 (1984).
11. R.P. Gale, G.W. Turner, J.C.C. Fan, R.L. Chapman, and J.V. Pantano, in *Proceedings of the 17th IEEE Photovoltaic Specialists Conference*, (IEEE, New York, 1984), p. 721.
12. S.M. Sze, *Physics of Semiconductor Devices* (Wiley, New York, 1981), p. 796.
13. C.R. Lewis, M.J. Ludowise, and W.T. Dietze, *J. Electron. Mater.* **13**, 44 (1984).
14. S.M. Sze, *Physics of Semiconductor Devices* (Wiley, New York, 1981), p. 68.
15. J.C.C. Fan, Solar Cells (to be published).

4. MICROELECTRONICS

4.1 QUANTUM-WELL CHARGE-COUPLED DEVICES

Charge-coupled device (CCD) technology using GaAs and AlGaAs is of major importance in the realization of a new high-speed spatial light modulator¹. In such a modulator, the quantity of charge in the CCD channel controls the electric field across an electroabsorptive medium. Currently, we are exploring the use of a strong electroabsorptive effect in GaAs/AlGaAs multiple quantum wells (MQWs). We describe here the successful demonstration of a new CCD structure whose channel comprises a GaAs/AlGaAs quantum well. The channel quantum-well layers were grown on a MQW structure, thus demonstrating the capability of integrating CCDs and MQWs on a single substrate.

A cross-sectional view of the integrated CCD/MQW spatial light modulator is shown in Figure 4-1. The material layers consist of a p⁺ AlGaAs ground plane followed by a MQW consisting of alternating undoped layers of GaAs and AlGaAs. MQW structures whose layer thicknesses are of the order of 100 Å have been shown to exhibit strong electroabsorption effects involving quantum-confined excitons when an electric field is applied normal to the layers². We also have measured these effects in similar structures and will describe them in future reports. The upper layers consist of two AlGaAs layers (at least one of which contains some n-type doping) separated by an undoped GaAs layer (approximately 100-200 Å thick), and these form a quantum well channel for the CCD. A Schottky-barrier gate structure for a three-phase CCD is deposited on the semiconductor surface, with one phase or set of gates transparent to admit illumination near the wavelength of the exciton resonances into the device.

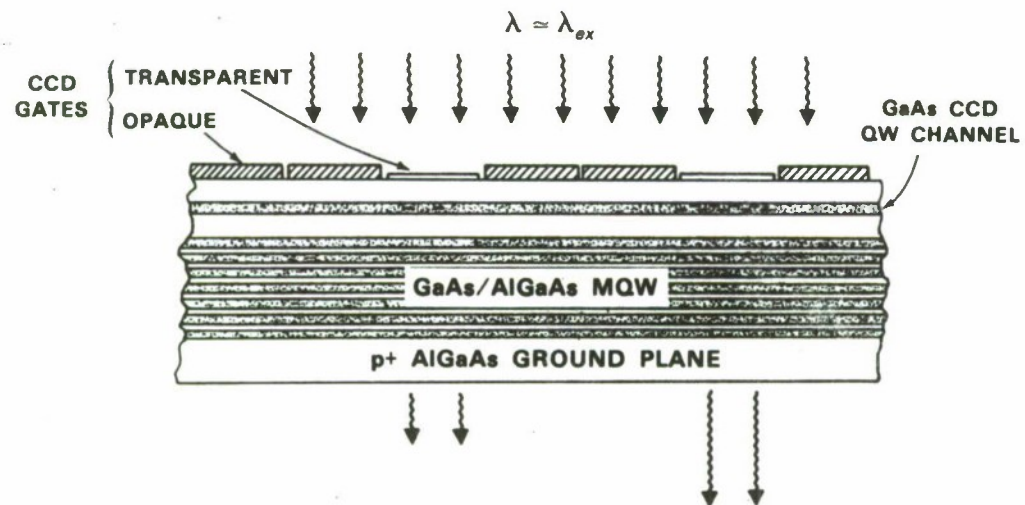


Figure 4-1. Cross-sectional view of an integrated quantum-well CCD/MQW spatial light modulator.

The operation of this device is explained by the energy-band diagram of Figure 4-2, which was calculated for a structure which approximates that of the device described below. The band edges shown in solid lines and the dashed line for the Fermi level correspond to the thermal equilibrium case (labeled 'full well'). The GaAs conduction band provides an energy minimum or quantum well that draws free electrons from the n-AlGaAs, ideally leaving the latter totally depleted. When the charge from this well is drawn off either by an adjacent well or an ohmic contact, the electron quasi-Fermi level drops, and the bands bend according to the dashed band edges labeled 'empty well.' This change in well occupancy causes the electric field across the MQW, and therefore its optical absorption, to be modulated. Thus, the radiation passing through

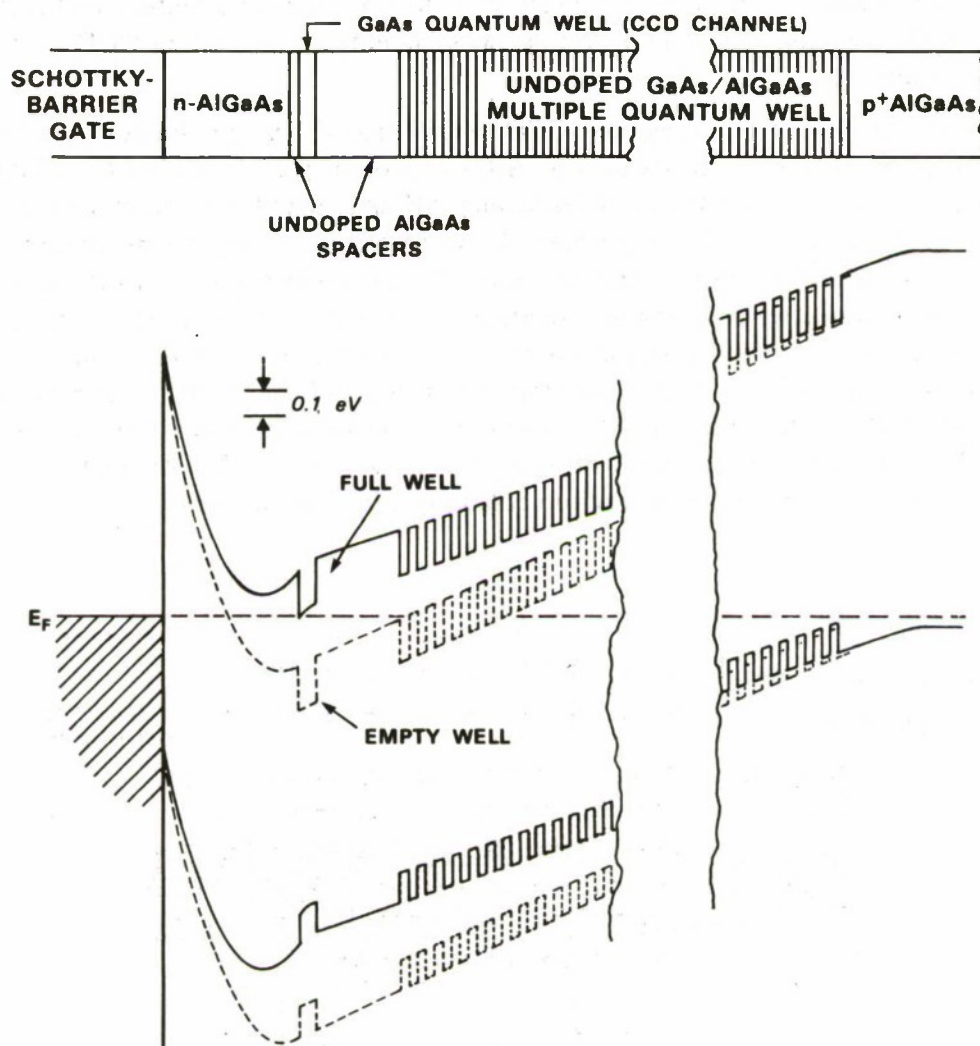


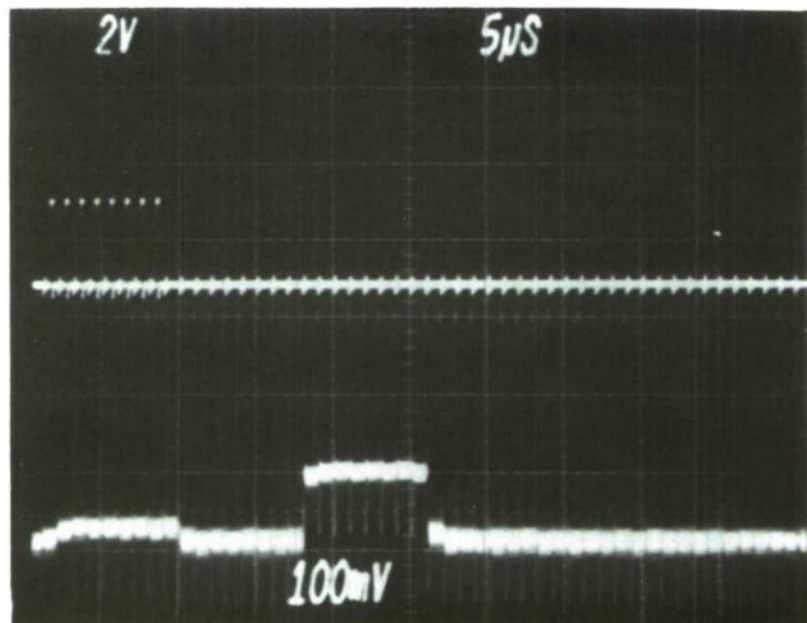
Figure 4-2. Material layer sequence and energy-band diagram of the structure of Figure 4-1 for the full well or thermal equilibrium case (solid curves and dashed line for the Fermi level) and for the empty-well case when the carriers are removed from the GaAs CCD quantum-well channel (dashed curves).

154093-N-03

the transparent gates shown in Figure 4-1 will emerge from the bottom of the device with a spatially varying intensity pattern derived from the quantum-well charge pattern.

We have fabricated a 16-stage, three-phase CCD using the structure described in Figures 4-1 and 4-2. The 60-period MQW structure consisted of undoped 80-Å GaAs and 200-Å AlGaAs layers, followed by a 400-Å layer of undoped AlGaAs, a 140-Å undoped GaAs layer, a 40-Å undoped AlGaAs isolation layer, and a 1000-Å n-AlGaAs layer doped to $2 \times 10^{17} \text{ cm}^{-3}$, all grown by molecular beam epitaxy (MBE). The AlAs mole fraction was 30% for all AlGaAs layers, and the growth took place at a substrate temperature of 715°C. The Schottky-barrier gates were 10 μm long with interelectrode gaps of about 1 μm, and were formed in a single layer of Ti/Au.

An example of device electrical performance at a 1.0-MHz clock rate is shown in Figure 4-3. The input to the device is a sequence of eight pulses (upper trace), while the lower trace shows the delayed output. The charge transfer inefficiency inferred from this measurement is 1.7×10^{-3} per transfer (assuming 48 transfers), and remained constant when the time between pulse bursts varied from 1 μs to 20 ms. This rules out bulk trapping as a cause for the charge loss, at least for traps whose emission time lies between 1 μs and 20 ms. The absence of measurable trapping effects is an expected result of the carrier confinement to the relatively small volume of the quantum well, as well as the carrier separation from known trapping centers in the AlGaAs. More likely, the loss is due to potential wells that can form beneath the interelectrode gaps. This is a persistent problem in the planar-gate structure used for this device, and efforts are being made to adapt an overlapping-gate structure³ to AlGaAs to alleviate it.



168182-N

Figure 4-3. Electrical performance of a 16-stage quantum-well CCD at a 1-MHz data rate. Upper trace is an input signal of eight pulses, while lower trace is the delayed output from the device.

As suggested by Figure 4-2, the maximum swing in channel potential was less than 1 V, a value that is too low to provide useful changes in the MQW optical transmission. Although the voltage swing can be increased to desired levels by increasing the n-AlGaAs thickness or doping, this has the undesired effect of placing the energy minimum in the n-AlGaAs. We are studying modifications to the structure to avoid this problem.

W.D. Goodhue

B.E. Burke

K.B. Nichols

G.D. Johnson

4.2 BALANCED MONOLITHIC MIXER FOR USE AT 44 GHz

Receiver front ends for satellite applications require low noise devices that have been space qualified to withstand shock and vibration during launch, and to operate reliably for many years with continuous LO power and cyclic temperature changes as the satellite passes in and out of earth's shadow.

We have fabricated a novel single-sideband balanced monolithic mixer suitable for use in satellites at 44 GHz. The mixer has a single-sideband noise figure of 6.5 dB flat to within 0.5 dB over a 2 GHz band centered at 44 GHz. The monolithic mixer chip is located at the intersection of a pair of orthogonal waveguides, producing a mixer structure that is simple, compact and rugged.

The design of the balanced monolithic mixer was based on refinements and extensions to the single-ended monolithic mixer described previously⁴, and on concepts of receiver design outlined in a recent publication⁵. This design aims to provide an embedding impedance to the Schottky-barrier diode that falls within an optimum embedding impedance range determined from the theoretical work of Saleh⁶ and the work of Held and Kerr⁷. Extensive use was made of low-frequency scale models of monolithic mixer circuits as an aid to developing an appropriate circuit embedding impedance environment. An embedding impedance locus obtained by network analyzer measurements at the diode port of a scale model of a monolithic mixer circuit is shown in Figure 4-4, with frequencies rescaled to the design frequencies. As can be seen in the figure, the embedding impedance presented to the diode port falls within the optimum embedding impedance range between 44 GHz and 45 GHz, and presents a slightly lossy short circuit in the vicinity of 36.5 GHz. Thus, the mixer should exhibit intrinsic image-enhanced single-sideband operation for image frequencies falling in the frequency region about 36.5 GHz.

The main features of the balanced monolithic mixer are shown in Figure 4-5. The mixer may be thought of as a folded magic-Tee mixer in which the two arms containing the diodes, and also the shunt junction, have been folded and placed on the surface of the GaAs. This balanced monolithic mixer is actually a three-dimensional monolithic implementation of a magic-Tee mixer. The monolithic mixer chip is located at the intersection of two orthogonal waveguides; it terminates the signal waveguide, transforming the impedance of the full-height

12B469-N-02

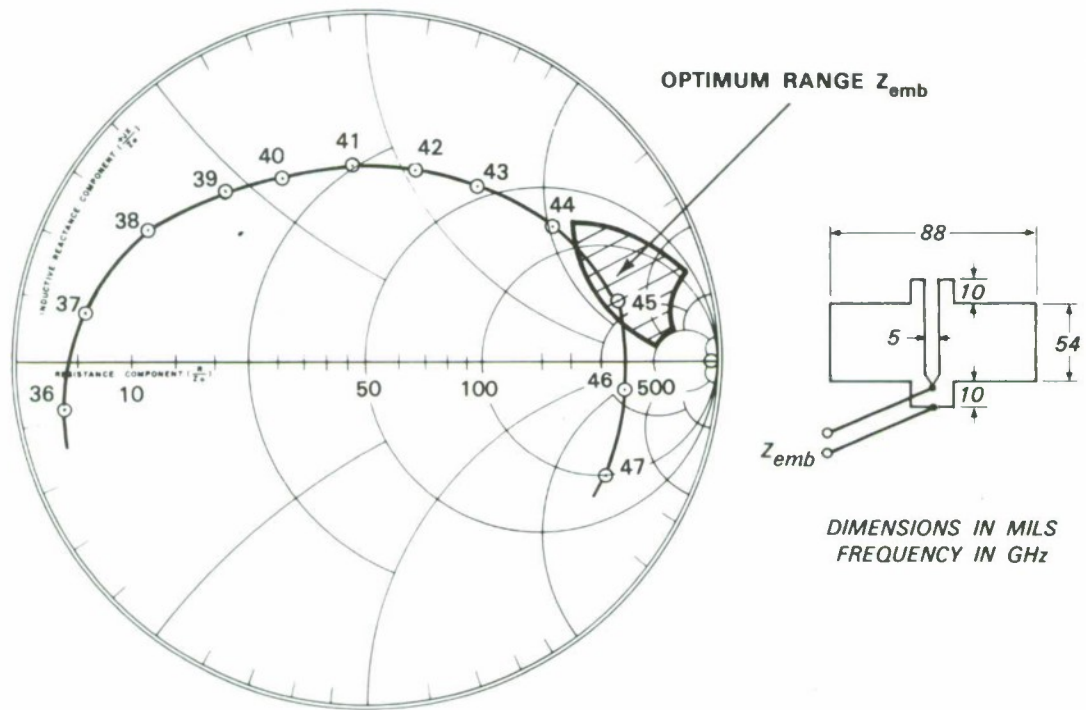


Figure 4-4. Projected embedding impedance locus for a monolithic mixer circuit as a function of frequency.

121731-N-N2

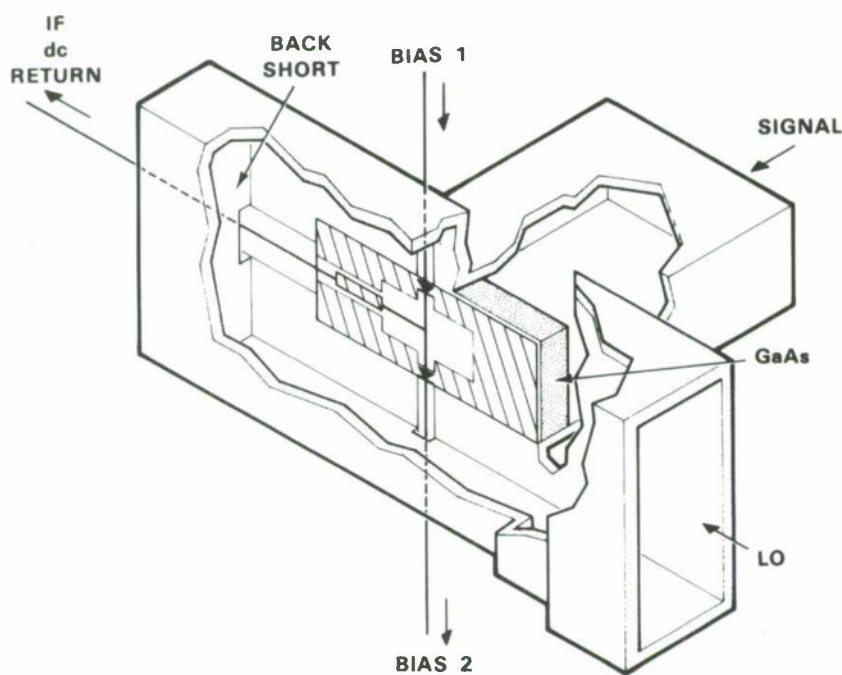


Figure 4-5. Balanced monolithic mixer.

signal waveguide and matching it to the surface-oriented diodes of the monolithic mixer circuit. The ground plane actually serves as the intersecting wall between the two orthogonal waveguides. The broad wall of the orthogonal LO guide opposite the slot of monolithic mixer chip serves as a backshort for the small amount of signal guide energy that is radiated from the slot into the LO guide. The Schottky diodes appear in parallel to the LO energy, which is coupled from the reduced-height waveguide to coplanar line on the surface of the GaAs. This coplanar line also serves to combine the IF outputs from the two diodes, and includes on-chip coplanar filters for LO and sum frequency rejection.

The monolithic balanced mixer circuit chip is alloy-bonded into a gold plated kovar carrier. The kovar carrier also includes microstrip bias-filter circuits and a microstrip IF output circuit with filtering and matching functions. The kovar carrier with integrated balanced monolithic mixer is mounted in a split-block waveguide mixer mount that contains the orthogonal signal and LO waveguide ports, bias connectors and IF output connector, as shown in Figure 4-6. The completed balanced monolithic mixer is shown in Figure 4-7.

Fabrication of the balanced monolithic mixer uses essentially the same semiconductor fabrication techniques that have been described previously for the single-ended monolithic mixers⁴. The GaAs monolithic mixer module dimensions are $0.2 \times 0.1 \times 0.011$ in, while the kovar carrier dimensions are $1.0 \times 1.0 \times 0.050$ in.

The mixer has given a single-sideband noise figure of 6.5 dB over a 2-GHz band centered at 44 GHz, as shown in Figure 4-8. This is believed to be the lowest noise figure measured for any room-temperature monolithic mixer. These results have been achieved with mixers that do not

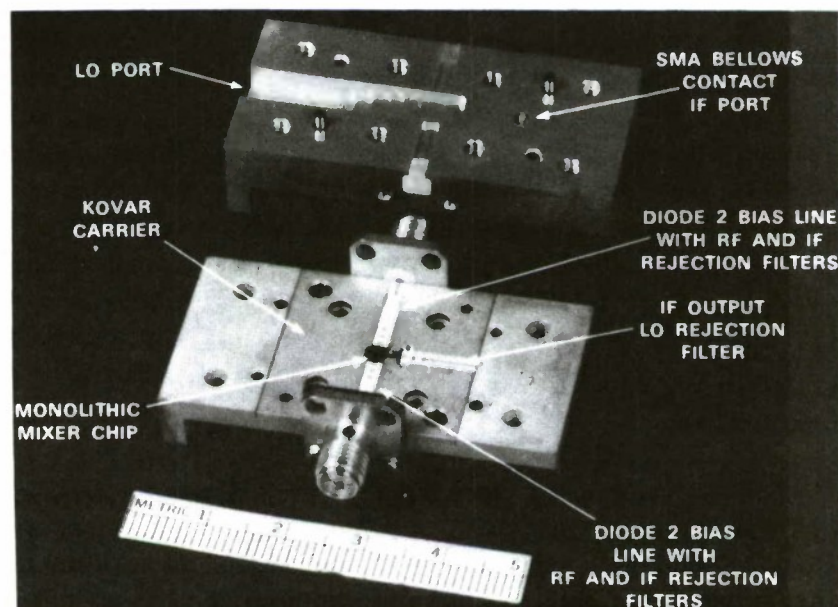


Figure 4-6. Balanced 44-GHz monolithic mixer in orthogonal waveguide structure.

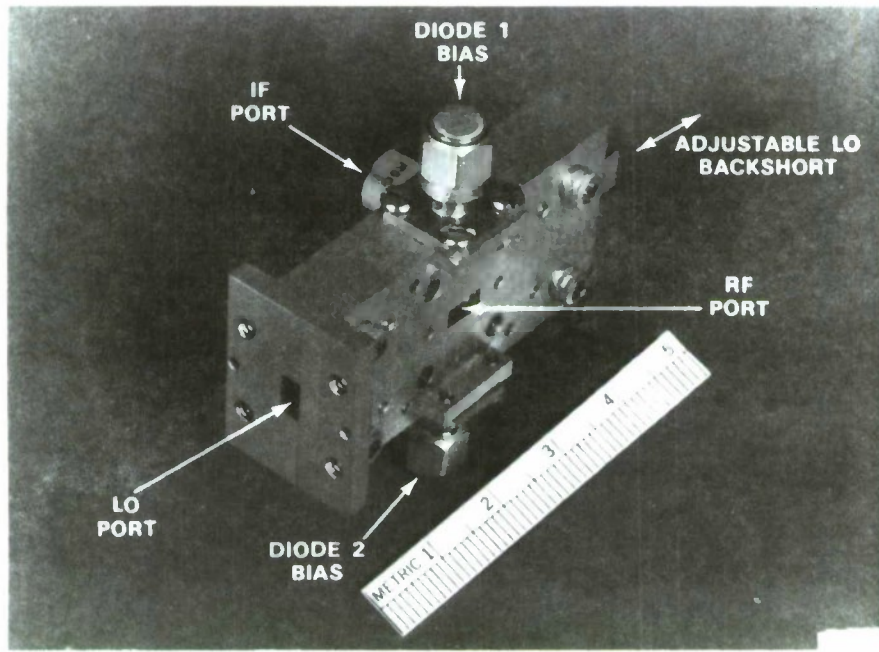


Figure 4-7. Assembled 44-GHz balanced monolithic mixer.

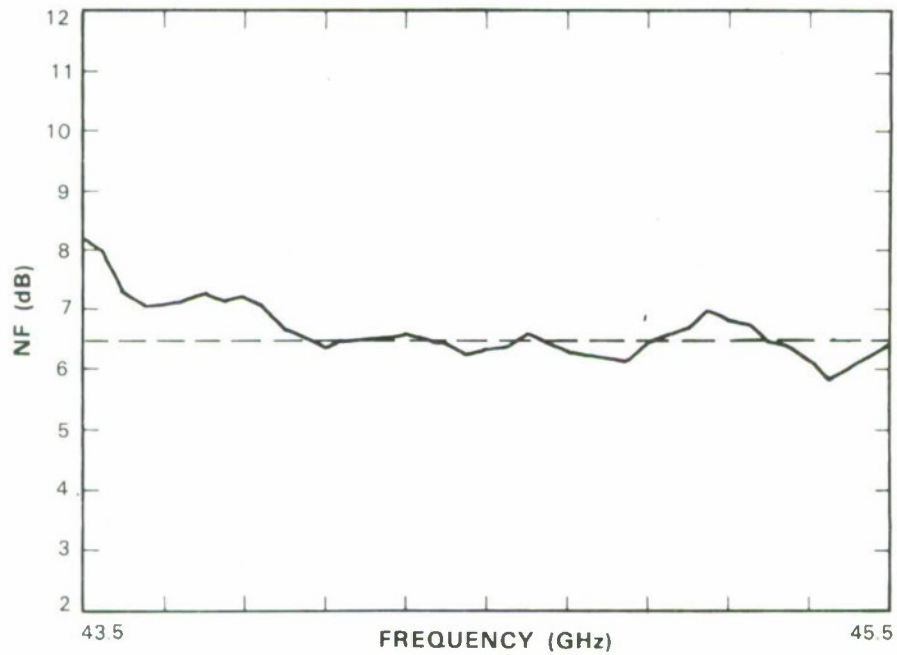


Figure 4-8. Balanced monolithic mixer single-sideband noise figure vs frequency.

have optimized RF and IF port matching. With further matching of signal and IF ports and optimized on-chip sum frequency termination, even lower noise figures should be possible. This mixer can be easily scaled to higher frequencies, maintaining all the advantages inherent in a balanced mixer.

B.J. Clifton
R.W. Chick

4.3 EXCIMER-LASER ETCHING OF DIAMOND AND HARD CARBON FILMS BY DIRECT WRITING AND OPTICAL PROJECTION

Laser-induced microchemical etching is being explored as an alternative to ion etching with distinct potential advantages, including patterning by direct-writing or optical projection without contact masks, higher etch rates, and reduced damage to fragile substrates. In well-controlled systems, short-wavelength laser sources can achieve linewidths of 0.2-0.5 μm , i.e., dimensions competing with refined optical lithography.

Below are described experiments on the dry etching of crystalline diamond and of diamond-like carbon thin films with reactions controlled by the deep-UV pulses from a rare-gas halide excimer laser. The diamond-like carbon thin films were explored as positive-acting resists for semiconductor patterning. Both of the above materials are chemically inert and are extremely hard to etch under either wet or dry etching conditions. The ArF laser, at 193 nm wavelength, is particularly suitable for interaction with diamond, since the photon energy at this wavelength, 6.4 eV, is higher than the 5.4 eV bandgap of diamond. Consequently, the crystal is highly absorptive at 193 nm.

In the direct writing geometry, 20- μm -wide lines were etched. Vertical or faceted line profiles were obtained with etch rates $\sim 1 \mu\text{m}/\text{s}$ in depth (20 J/cm^2 , 20 Hz). For projection patterning, chrome-on-quartz transmission masks were imaged at 36x reduction onto the substrate. Well-defined gratings $\sim 1000 \text{ \AA}$ deep with periods as small as 0.25 μm , were obtained with single, 15-ns-long pulses. An example is shown in Figure 4-9. Note that the linewidth is $\sim 0.13 \mu\text{m}$, less than the wavelength of the laser. For such single-shot exposures, nearly sinusoidal features with an amplitude close to the half-period (i.e., line width) dimension are achieved. Deeper structures can be obtained with multiple pulsing, although, in our undamped apparatus, only with reduced dimensional control because of mechanical vibration. In a mechanically stabilized projection system, etching of deep gratings with 0.25- μm period or less should be possible.

Two processes take place during laser irradiation: conversion of diamond to graphite and sublimation or reaction of carbon. The former manifests itself in a deposit-like morphology (due to the lower density of graphite relative to the initial diamond), in increased opacity in the visible, and in a dramatic rise in electrical conductivity. The rate of this conversion, as measured by optical transmission, exhibits a threshold at $\sim 60 \text{ mJ/cm}^2$, and then increases nonlinearly with increasing laser fluence.

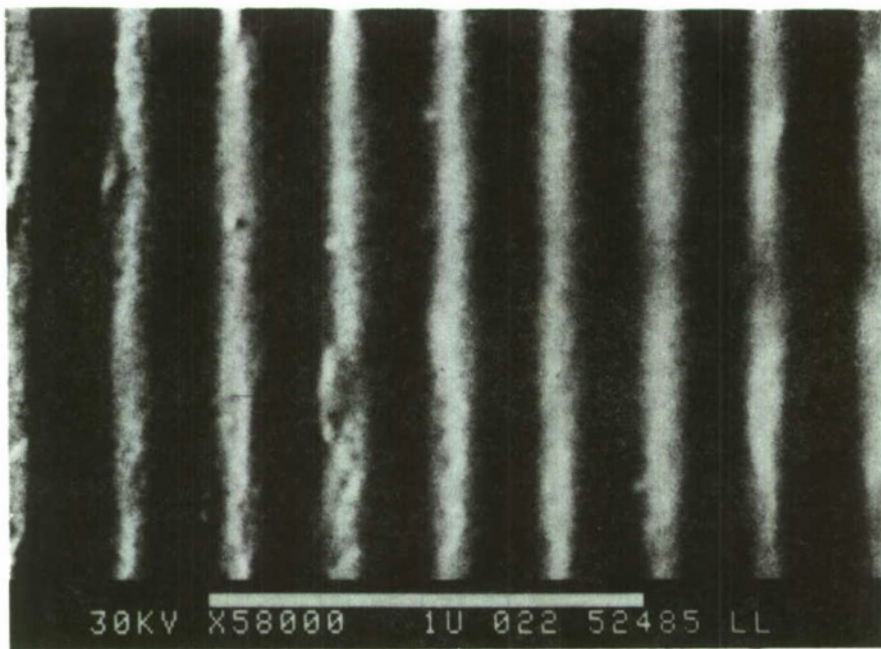
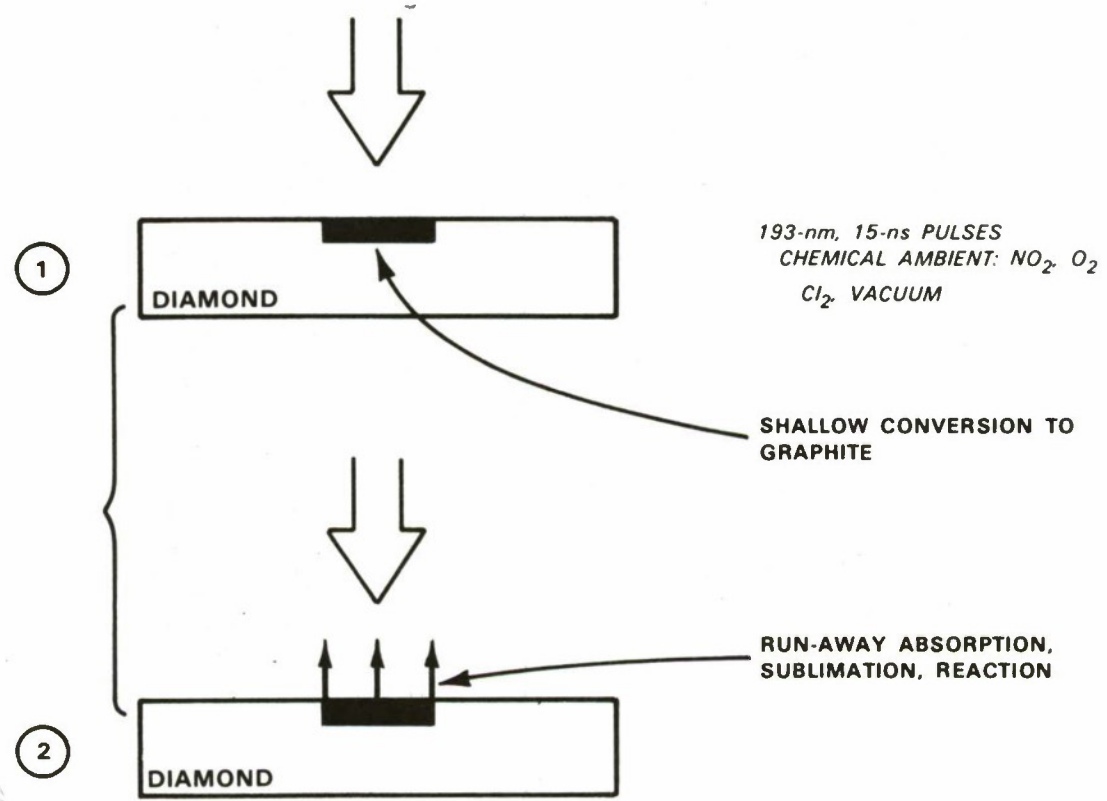


Figure 4-9. Scanning electron micrograph of a 0.25- μm -period grating etched in monocrystalline diamond with a 0.193- μm laser. The grating was generated in projection with one 15-ns excimer-laser pulse. The fluence was 65 J/cm².

The graphite generated at the diamond surface in the early parts of a laser pulse has a smaller absorption length than that of the diamond (0.1 μm compared to $\sim 10 \mu\text{m}$) and a lower thermal diffusion constant ($1.4 \text{ cm}^2/\text{s}$ compared to $11 \text{ cm}^2/\text{s}$ at room temperature). Consequently, the energy of the latter part of the laser pulse is deposited and localized in the graphite layer, leading to runaway absorption and, at high laser power, to vaporization. Figure 4-10 is a schematic representation of the processes taking place during excimer-laser-induced etching of diamond.

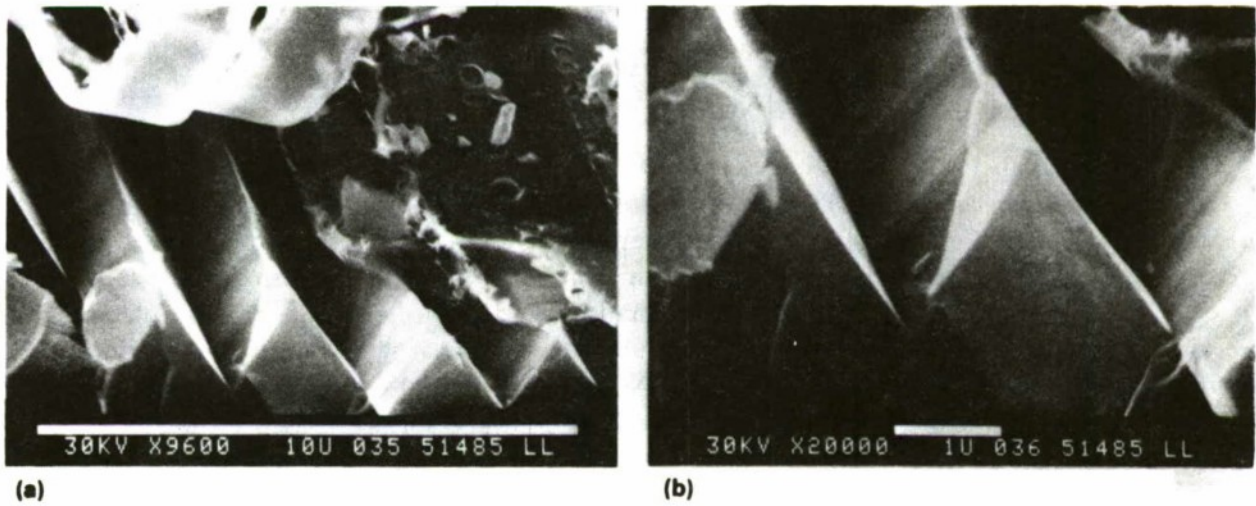
The large temperature difference between formation and sublimation of the graphitic layer in vacuum leads to an accumulated graphitic 'deposit' in the lower-energy wings of the laser-illuminated regions. To reduce the required temperature and eliminate accumulation of graphite, reactive ambient vapors were used to react with the heated graphitic layer. Volatile products (CCl_4 , CO , CO_2) at temperatures below sublimation were formed, and the amount of graphitic residue was reduced dramatically. The best results were obtained with gases simultaneously photolyzed during the pulse, such as Cl_2 , O_2 , NO_2 . Under typical conditions, free radical densities of $10^{17}\text{-}10^{18} \text{ cm}^{-3}$ are generated by the laser near the surface. Based on our observations, these radicals react with near unit efficiency with the hot graphitic layer.

The effectiveness of excimer-laser etching of diamond indicates that the same laser may be effective in etching hard-carbon thin films. These films have been shown to contain carbon in tetrahedral bonding, analogous to the diamond structure, to have extremely low electrical



151787-N-03

Figure 4-10. Schematic representation of the excimer-laser/diamond interaction.



152515-N-02

Figure 4-11. Scanning electron micrographs at two different magnifications of grooves etched in GaAs following exposure of the carbon thin film to excimer-laser irradiation (0.5 J/cm², one 15-ns pulse). In (a), the carbon film and the laser-induced etch pattern on it are clearly visible.

conductivity, and to be hard and very resistant to chemical attack. These same properties make them potentially attractive as resists. A GaAs crystal covered by a 2000-Å-thick carbon film was exposed in projection as described above to one 193-nm laser pulse. Following the laser etching of the carbon mask, the sample was wet etched in a GaAs etchant ($\text{CH}_3\text{OH}:\text{H}_3\text{PO}_4:\text{H}_2\text{O}_2$ in the ratio 3:1:1) for one minute. This etchant has a preferentially lower etch rate on the Ga [111] surface. The processed GaAs exhibited V-shaped grooves coinciding with the grating etched by the laser in the carbon thin film. The grooves had a period of 2.8 μm and were $\sim 2.2 \mu\text{m}$ deep (Figure 4-11). Although only preliminary experiments have been completed, such films show excellent promise as resists to mask both wet and dry etching. Note that the radiation sensitivity (required dose $\sim 0.5 \text{ J/cm}^2$) is consistent with efficient patterning in a step-and-repeat geometry with a small commercial excimer laser.

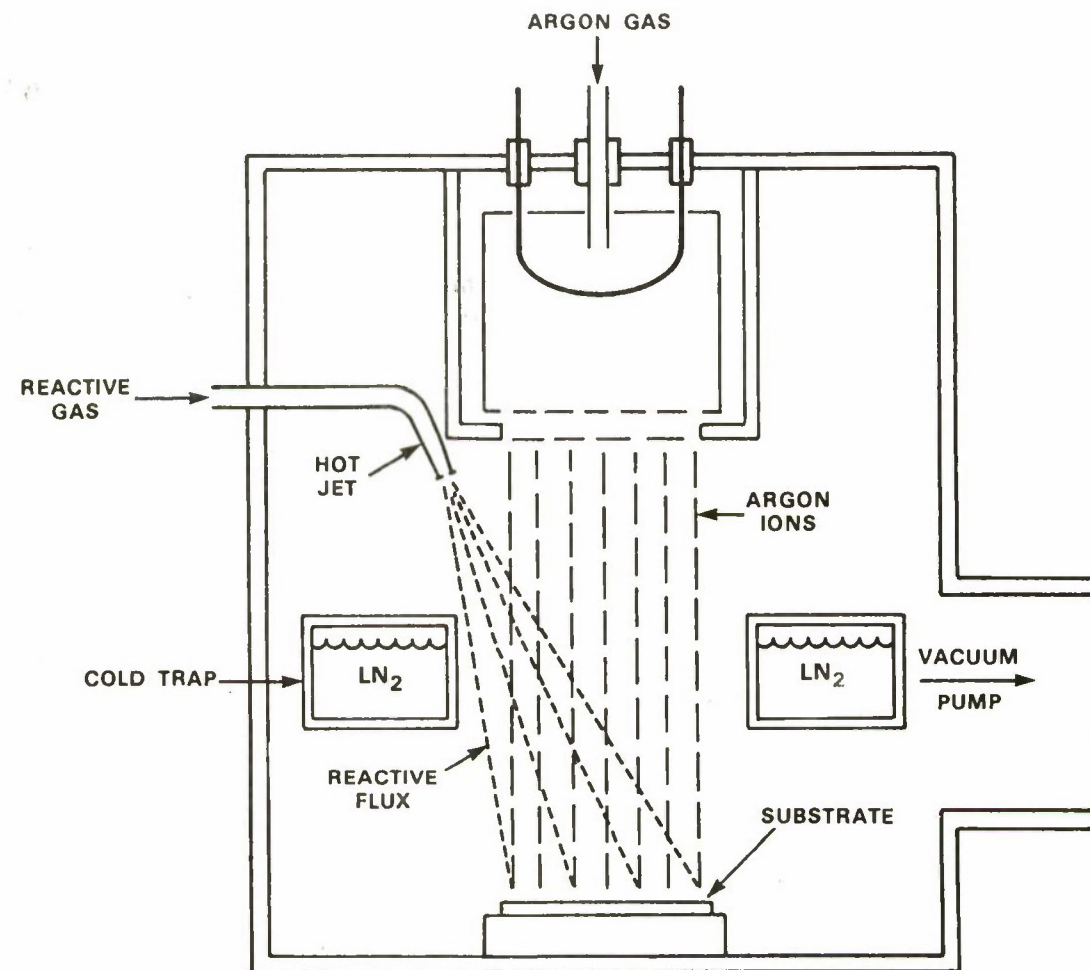
M. Rothschild
D.J. Ehrlich

4.4 HOT JET ETCHING OF GaAs AND Si

Conventional anisotropic dry etching usually is accomplished with a combination of energetic ions and chemically reactive species produced in a plasma from an unreactive gas. This report contains a description of a new dry etching technique — hot jet etching — requiring no energetic ions or plasma, in which the anisotropic etching is obtained from a directed flux of chemically reactive species. The reactive species are obtained from the thermal decomposition of comparatively unreactive gases. The etching technique has the advantages of simplicity of operation and a large differential etching rate between the mask and the substrate materials.

The etching system shown in Figure 4-12, consists of a Kaufman ion source used to sputter clean the surface of the sample prior to etching, a resistively heated tube (hot jet) through which the unreactive gases are disassociated to form a directed flux of hot reactive species, and a liquid nitrogen cold trap that efficiently pumps both the unused reactive species and the reaction products. The distance between the hot jet and the sample is approximately 10 cm. The samples are heat sunk to an air-cooled plate to ensure they remain near room temperature during etching. However, even samples that were not heat sunk during etching showed no thermal effects since the heat flux on the samples is less than 0.3 W cm^{-2} . Similar systems have been used for ion beam assisted etching^{8,9} (IBAE). Etching is accomplished by first sputter cleaning the sample, after which the ion beam is turned off and the reactive species produced from the hot jet are allowed to etch the sample.

The production of the reactive species depends upon the unreactive feed gas, the temperature of the hot jet, and the chemical and thermal stability of the hot jet. Any gas consisting of two or more elements can be decomposed at a sufficiently high temperature. But, because of material limitations, the hot jet used in these experiments cannot be operated much above 2500° , and the addition of reactive gases may limit the operating temperature still further. However, even at this temperature, many gases can be dissociated into free radicals. The fractional dissociation of the gas into free radicals depends upon the gas pressure and temperature. The calculated percentage



152565-N-01

Figure 4-12. Diagram of the hot jet etching system.

of free radicals formed in a hot jet as a function of temperature is shown in Figure 4-13. These calculations assumed an estimated experimental room-temperature pressure of 20 Torr in the jet. Since the mass flow of gas is held constant in these experiments, the gas pressure in the hot jet is assumed to increase with the square root of temperature and the percentage of gas dissociation. Gases like F_2 , Br_2 , Cl_2 , CF_3Br , and CF_3CF_3 can be decomposed easily into free radicals at temperatures less than $1800^\circ C$. However gases like H_2 , N_2 or CF_4 require higher temperatures or lower gas pressures to obtain thermal decomposition.

The stability of the hot jet depends upon its design. Figure 4-14 is a drawing of one of the several hot jets used in these experiments. It consists of a tungsten tube resistively heated to temperatures between 1500° and $2500^\circ C$. The ends of the tube are held in position by springs made from 1 mm tungsten wire and the gas is fed into the tube through an alumina tube. The hot jet shown in the figure was designed to operate with Cl_2 as a feed gas. Chlorine is known to

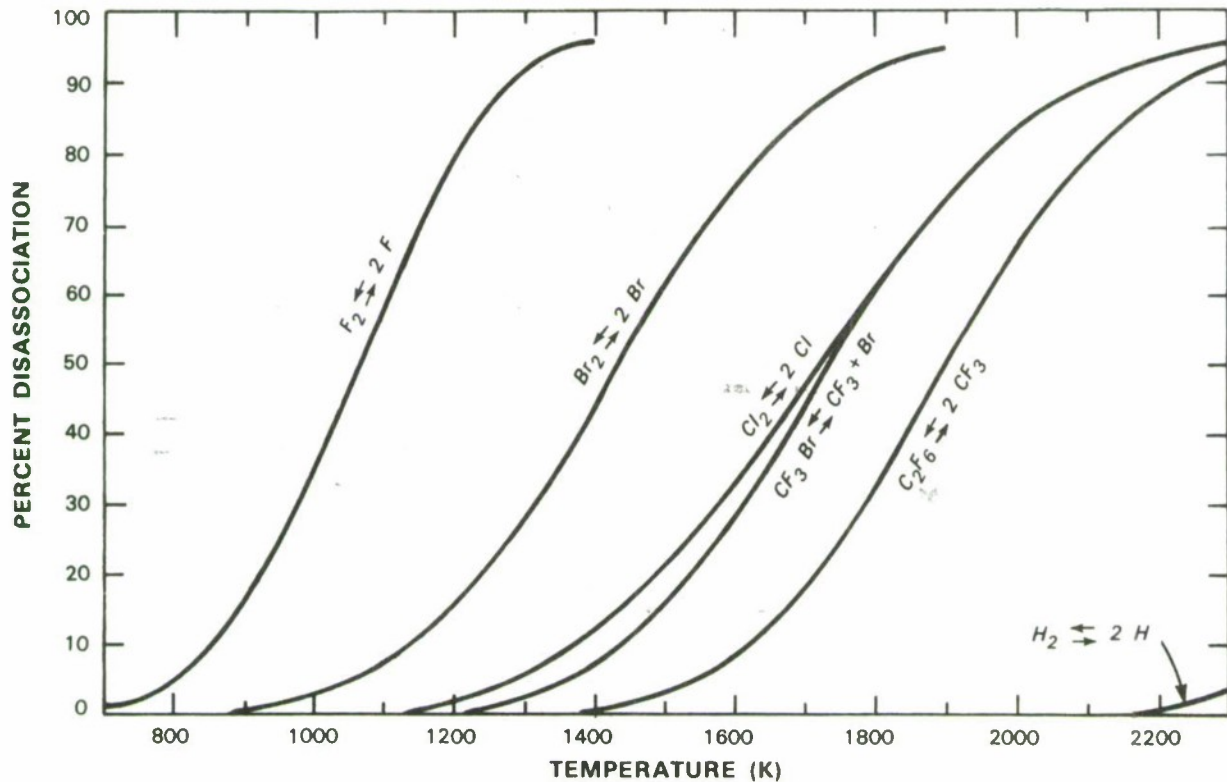
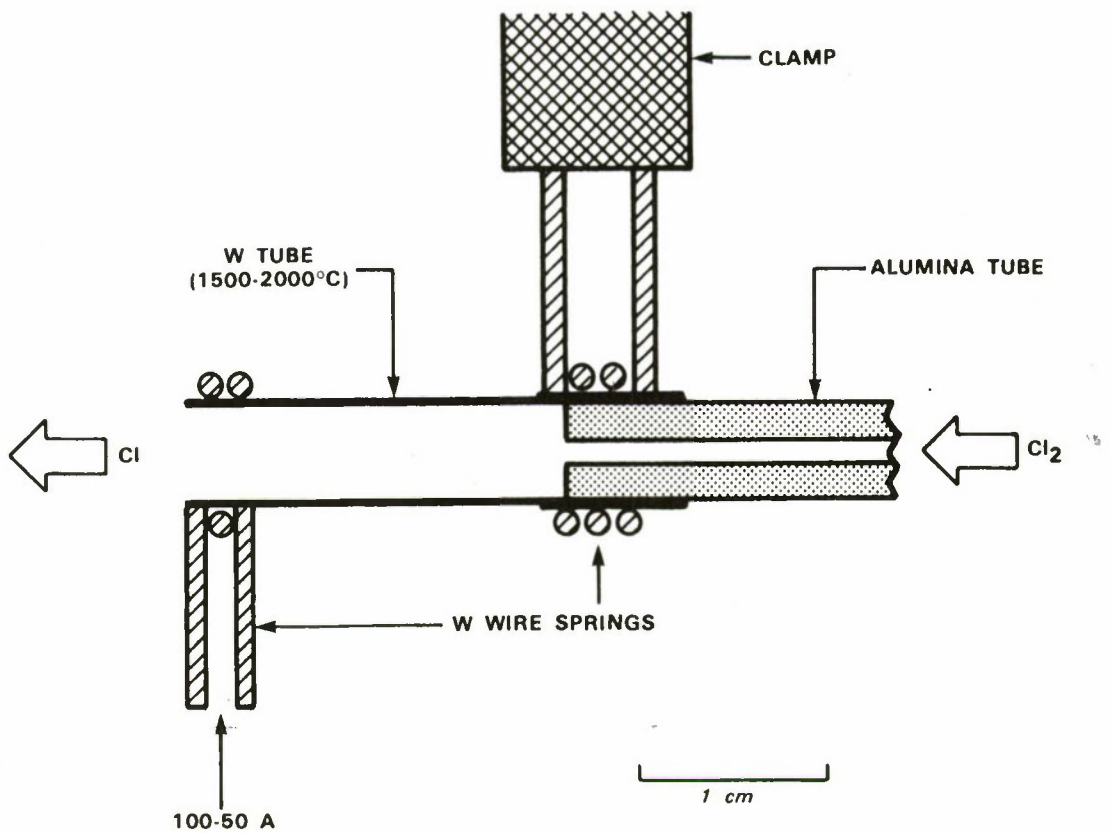


Figure 4-13. Percentage of radicals formed by thermal dissociation.

react with tungsten at temperatures above 300°C, forming a variety of volatile tungsten chlorides. However, at temperatures above 1500°C, tungsten becomes inert to Cl₂. This insures that the hot jet will operate with Cl₂ provided all the tungsten surfaces that will come in contact with Cl₂ are above 1500°C. Hot jets have been operated with Cl₂ for up to an hour without degradation. However, when these jets are operated below 1500°C, the Cl₂ will etch the tungsten tube away in less than 20 s. Gases like CF₃Br are comparatively unreactive, and the jet design is not critical.

By using the hot jet technique, a variety of materials have been etched, as shown in Table 4-1. These etching rates were obtained with a hot jet exit pressure estimated between 20 and 60 Torr, a sample flux equivalent pressure between 3 and 10 mTorr, and a hot jet temperature between 1500°C and 2500°C. Since there is no ion beam used during the etching of the samples (except to sputter clean the sample surface), high differential etching rates are possible. Etching rates of photoresist and SiO₂ were too small to measure, <0.1 μm min⁻¹, when Cl₂ was used as a feed gas. Even the few-nanometer-thick native oxide on top of the GaAs sample was sufficient to mask the sample during etching.

Since there is no ion beam used during the etching, any accumulation of material on the etching surface from the hot jet or the vacuum system could cause the reduction of the etching rate. To check for this, the etch depth into GaAs was plotted as a function of the etching time.



152566-N-01

Figure 4-14. Scale drawing of the hot jet. The hot jet dimensions were found not to be critical.

TABLE 4-1
Hot Jet Etching
(nm/min)

Gas	GaAs	Si	SiO ₂	Photoresist
Cl ₂	2-5*	10	<0.1	<0.1
CF ₃ Br	10	10	<0.1	<0.1
SF ₆	<0.1	200-300	-----	-----

* ($\mu\text{m}/\text{min}$)

The etch depth was found to be a linear function of the etch time, indicating that there is no evidence of contamination. Etched depths as deep as 75 μm have been obtained without any indication of the etch rate diminishing. The etch rate for Cl₂ feed gas on GaAs was found to be linearly dependent upon the equivalent flux pressure of reactive species on the sample up to a pressure of about 5 mTorr. An anisotropic etch ratio of the etch depth to the undercutting distance of 5, which is obtained by hot jet etching GaAs with Cl₂, is acceptable for some device fabrication and etched-through holes in GaAs wafers. Etching uniformity better than 10% was obtained over an area of 4 cm in diameter.

In summary, a new dry etching technique has been described that does not require directed ions to obtain anisotropic etching. The anisotropic etching is obtained by a directed flux of chemically reactive species. Since no ions are involved with this technique, the etching is purely chemical, and high differential etch rates are possible. At present only a very limited number of gases and hot jet designs have been used with this technique.

M.W. Geis

REFERENCES

1. R.H. Kingston, B.E. Burke, K.B. Nichols, and F.J. Leonberger, *Appl. Phys. Lett.* **41**, 413 (1982).
2. T.H. Wood, C.A. Burrus, D.A.B. Miller, D.S. Chemla, T.C. Damen, A.C. Gossard, and W. Wiegmann, *Appl. Phys. Lett.* **44**, 16 (1984).
3. K.B. Nichols and B.E. Burke, *IEEE Electron. Device Lett.* **EDL-6**, 237 (1985).
4. B.J. Clifton, G.D. Alley, R.A. Murphy, and I.H. Mroczkowski, *IEEE Trans. Electron Devices* **ED-28**, 155 (1981).
5. B.J. Clifton, *Infrared Phys.* **25**, 267 (1985).
6. A.A.M. Saleh, *Theory of Resistive Mixers*, Research Monograph No. 64, (MIT Press, Cambridge, Massachusetts 1971).
7. D.N. Held and A.R. Kerr, *IEEE Trans. Microwave Theory Tech.* **MTT-26**, 49 (1978).
8. M.W. Geis, G.A. Lincoln, N.N. Efremow, and W.J. Piacentini, *J. Vac. Sci. Technol.* **19**, 1390 (1980).
9. G.A. Lincoln, M.W. Geis, S.W. Pang, and N.N. Efremow, *J. Vac. Sci. Technol.* **B1**, 1043 (1983).

5. ANALOG DEVICE TECHNOLOGY

5.1 DUAL-CHANNEL, 256-SAMPLE, 128-TAP ANALOG-BINARY CHARGE-COUPLED-DEVICE (CCD) CORRELATOR

A flexible analog-binary correlator has been designed for use in a wide range of applications, such as radar and spread-spectrum communications. To facilitate application, the device has been made as self-contained and easy to use as possible. To assure that a sufficient number of correlators is available for large-scale programs, two commercial CCD foundries have been placed under contract to fabricate the device in parallel with fabrication at Lincoln Laboratory.

A table of correlator specifications and a block diagram are given in Table 5-1 and Figure 5-1, respectively. Although fabricated in 4- μm NMOS technology, the device performance compares extremely favorably in every category with the goals set for the two VHSIC digital correlators under development by TRW and Hughes. In addition, the CCD correlator is immune to the detrimental effects of quantization possible with digital correlators in many applications. The description that follows focuses on issues of interest from a user viewpoint.

During the design of the correlator, heavy emphasis was placed on simplifying the interface requirements. Hence, all required clock circuitry, bias generators, auto-zero circuitry, magnituding

TABLE 5-1
Correlator Specifications

Dual 256-Sample/128-Chip Architecture
I and Q Differential Outputs
Minimum Dynamic Range >50 dB
Nonlinearity <0.5%
On-Chip Magnitude Circuit
On-Chip Clock Drivers
On-Chip Static Protection
5-V CMOS Logic Compatibility
MILSPEC Temperature Range Operation
68-Contact JEDEC LCC Package
Device Interchangeability

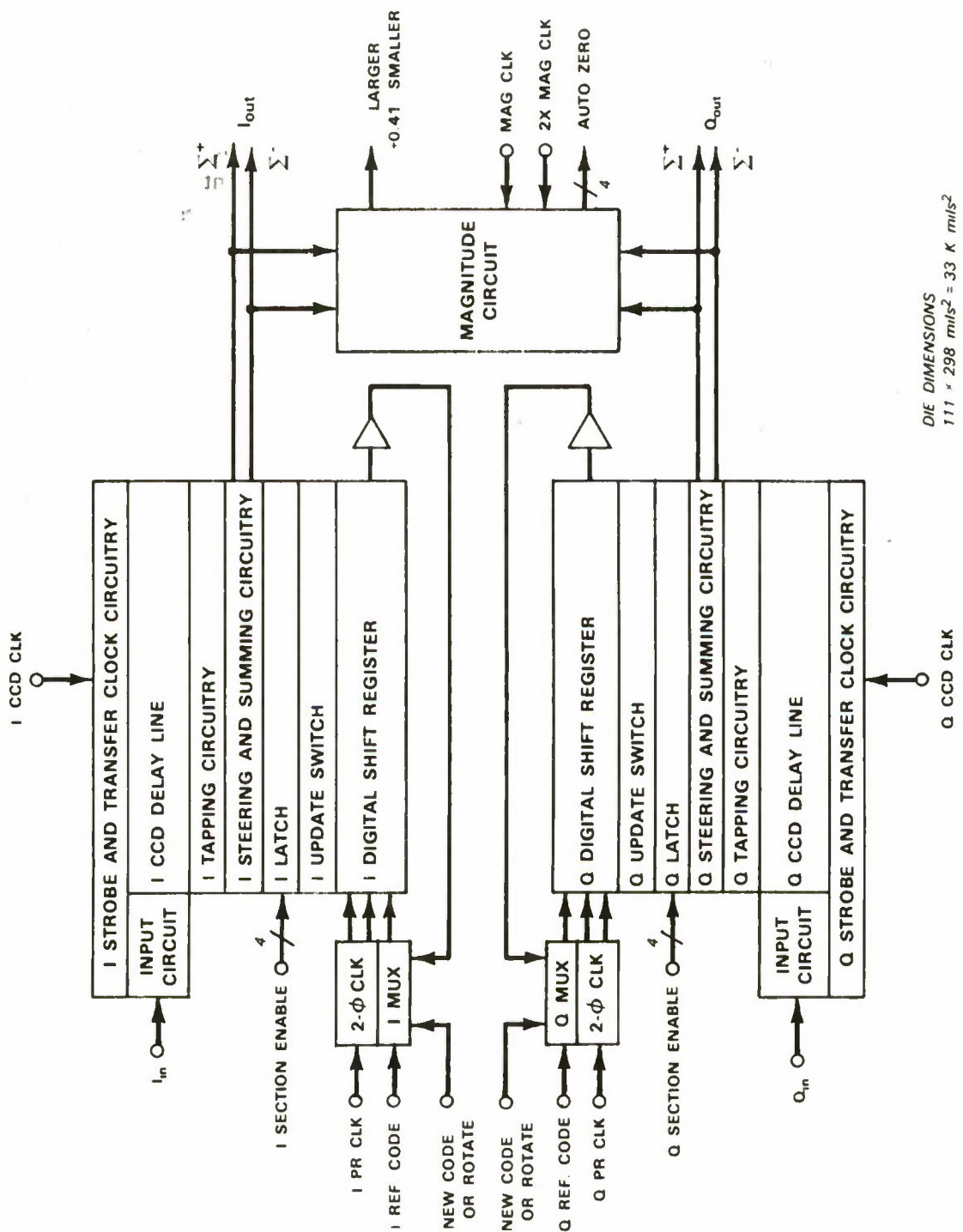


Figure 5-1. CCD correlator block diagram.

circuitry, etc., have been integrated on chip. The use of CCD technology is invisible to the user. Aside from an external resistor required to set the transconductance in the analog circuitry, one need only apply power, digital inputs, and the analog signal to operate the device. All inputs are high impedance and logic inputs are 5-V CMOS compatible.

The two channels on the chip are, except for the output magnitude circuitry, completely independent and may have different reference codes, clock rates, etc. Each may be powered independently up or down, if desired, and each has four 64-sample sections that may be enabled or disabled independently.

The double-sampling single-tapping architecture (i.e., sample twice per code chip but sense only one sample per chip internally at a given time) provides considerable flexibility. Only alternate samples participate in the correlation each clock cycle. This means that in addition to double-sampling one waveform, single-sampling of two independent waveforms by each channel is possible. In I and Q applications, for example, the I and Q inputs may alternate between the two channels (thereby facilitating MSK demodulation). If one of the two independent waveforms is the analog zero of the other, then a high accuracy auto-zero reference is available at the output every other clock cycle.

To facilitate cyclic code-shift keying (CCSK) demodulation, the reference code program register has been made fully static and incorporates a wraparound feature that allows easy reference code rotation. A multiplexer at the input to the program register selects between an external input and the output of the program register. Code rotation is effected by simply placing the MUX in the correct state and clocking the program register. When the reference code is rotated to the desired point, the reference code latches are updated.

A magnitude circuit sums the magnitudes of the I and Q outputs. The result is routed off chip through a buffer. By accomplishing the magnituding on chip, a considerable reduction in off-chip hardware is realized, and summing I and Q magnitudes reduces to one the number of A/D converters required.

In the second iteration of the correlator, a more sophisticated magnituding circuit may be added, which yields a result very close to the ideal $\sqrt{I^2 + Q^2}$. Because of the decision making required in this circuit, it will be able to operate up to half the maximum rate (25 MHz) of the raw analog output.

The quiescent operating points of the correlator outputs are not ground referenced and may vary because of processing and temperature changes. In order to facilitate the interface to an A/D converter, the magnitude output has on-chip auto-zero circuitry that establishes the reference potential on the A/D side of a dc blocking capacitor. In this way, the user can set a drift-free zero reference suitable for any post-correlator processing circuitry.

Wafers made using the Lincoln Laboratory pattern generator tape have been received from one commercial foundry, and the yield has been excellent. Packaged devices from these wafers have been clocked up to the 25-MHz design goal with excellent results. Complete characterization of the correlators is underway.

Figure 5-2 shows, on the two time scales, oscilloscopes of the correlator input (upper trace) and output (lower trace) at a 10-MHz clock (sample) rate and a 5-MHz chipping rate. Because of test equipment limitations, the signal is limited to one-third of full scale. The input is a cyclic maximal-length sequence of length 127. Ideally, the output would be a double correlation spike every 127 clock cycles with flat side lobes in between. As can be seen in the figure, some of the input signal is feeding through to the output. The cause of this problem has been isolated and will be eliminated in the final mask set.

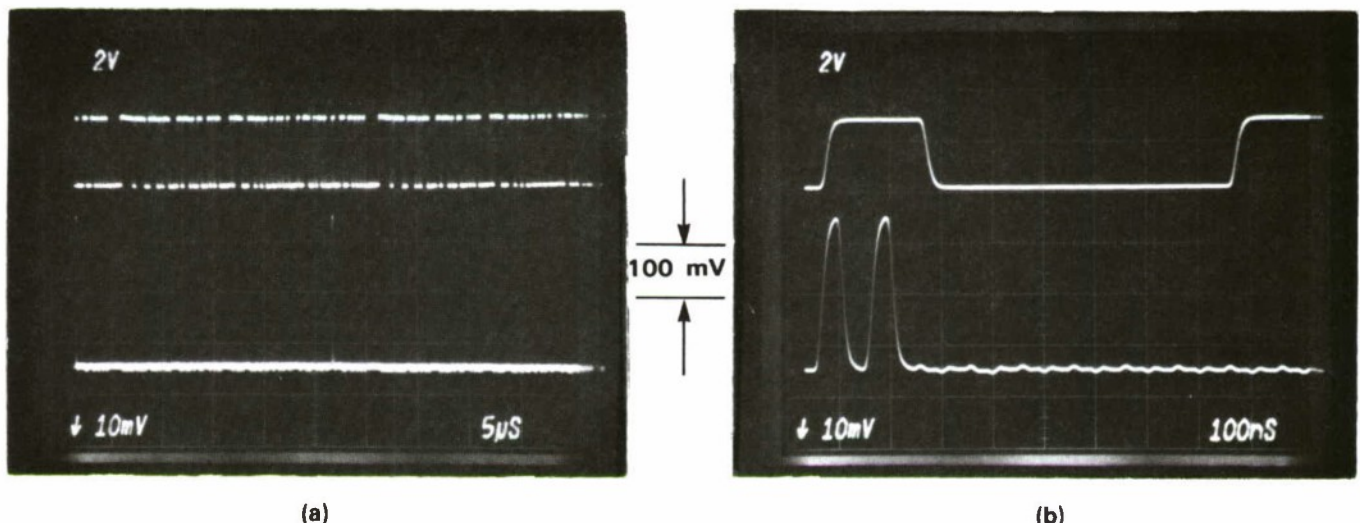


Figure 5-2. Code input (top traces) and correlation output (bottom traces) displayed at (a) 5 μ s/div and (b) 100 ns/div.

Despite the feedthrough and reduced signal level, a dynamic range of 40 dB has been measured. This fact lends confidence that the final version of the device will reach the 50-dB minimum dynamic range goal. The high speed of these devices makes them competitive with surface-acoustic-wave devices.

S.C. Munroe

5.2 OPTICALLY ADDRESSED READOUT OF MOS AND MNOS ARRAYS

Solid-state imagers have reached densities of 4×10^6 pixels in large ($5.5\text{ cm} \times 5.5\text{ cm}$) chips¹. In order to attain densities of 10^6 pixels in more reasonable areas (1 cm^2), pixel areas of $10\text{ }\mu\text{m} \times 10\text{ }\mu\text{m}$ or less are required. Provision of conventional charge-coupled or column-addressed readout circuits will severely stress photolithography and yield.

An optically addressed readout technique has been developed that replaces the on-chip electrical readout structures with a scanning optical beam. Pixels are addressed by the beam, which causes the addressed cells to discharge into the substrate. Random access is preserved in an array that requires only one photolithographic step to define the pixels.

This technique has been demonstrated with MNOS pixels^{2,3}, in which the photogenerated carriers are stored in nonvolatile form in the nitride gate dielectric, although it is equally applicable to MOS arrays. Figure 5-3 is a cross section of a pixel. Images are formed by photogeneration in the depletion layer. The latent image represented by electrons in the resulting inversion layer is committed to nonvolatile storage by the application of a large write pulse to the gate, which causes tunneling of the inversion layer electrons to traps in the silicon nitride. This stored charge is manifested by a shift in the pixel's flatband voltage V_{FB} . Previously, this has been sensed by a capacitive measurement² or by the nondestructive replication of mobile inversion-layer charge³.

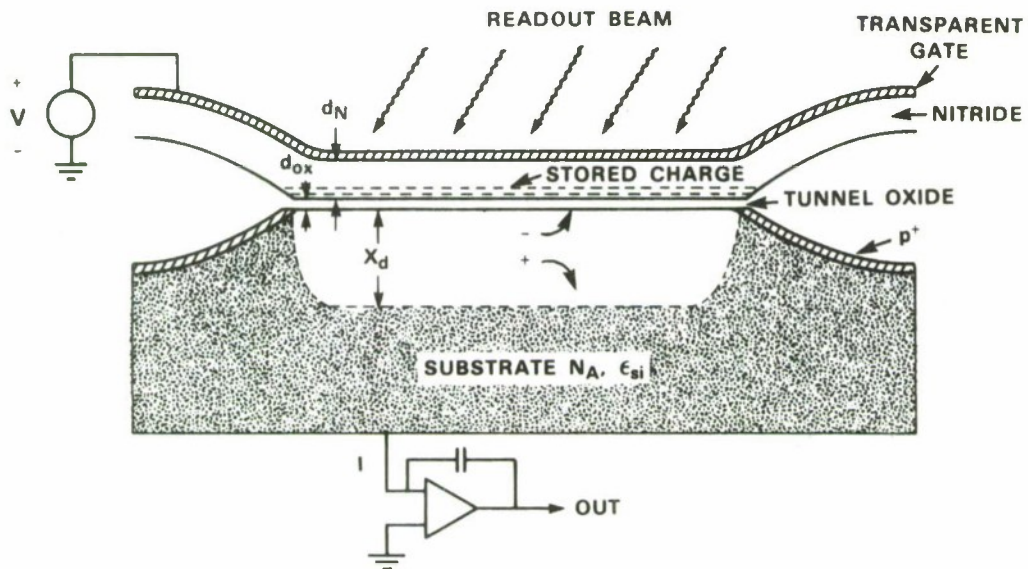


Figure 5-3. Cross section of MNOS pixel during optically addressed readout. The pixel is discharged by hole-electron pairs created in the depletion layer by the readout beam.

The optically addressed readout proceeds as follows: The substrate is accumulated to eliminate any inversion charge and then deep-depleted by a bias voltage V . The substrate current integrator is reset before the readout of each pixel. When the readout beam illuminates the pixel, photogenerated electrons collect in the inversion layer until equilibrium is achieved. During this discharge of the deep-depleted pixel, current flows in the substrate and is integrated in the off-chip integrator. The net charge flow is the difference between the displacement field $\epsilon_{ox}E_o$ in the oxide before the beginning of the discharge and the field $\epsilon_{ox}E_1$ in the oxide after equilibrium is established. The predischarge field is

$$\epsilon_{ox}E_o \approx -qN_Ax_d = -[2qN_A\epsilon_{si}(V - V_{FB})]^{1/2},$$

where x_d is the depletion layer width, N_A is the substrate doping, and ϵ_{si} is the substrate permittivity. The approximation is based on the depletion approximation (small Debye length)

and further neglects the voltage drop across the dielectric caused by the depletion-layer field relative to the drop across the depletion layer. This latter approximation is valid if

$$\frac{d_N}{\epsilon_N} \left(\frac{2qN_A\epsilon_{Si}}{V - V_{FB}} \right)^{1/2} \ll 1,$$

where ϵ_N is the nitride permittivity and where it is assumed that the nitride width d_N is much greater than the oxide width d_{ox} . The approximation holds for typically thin dielectrics RSW and lightly doped substrates. The equilibrium oxide displacement field is again, assuming $d_N \gg d_{ox}$,

$$\epsilon_{ox}E_t \approx -\frac{\epsilon_N}{d_N} (V - V_{FB} - \psi_s) ,$$

where the surface potential $\psi_s \approx 2\psi_B \approx (2 kT/q) \ln (N_A/n_i)$. The measured substrate charge flow is then

$$Q = \int I dt = -\epsilon_{ox} (E_t - E_0) \approx -\frac{\epsilon_N}{d_N} [V - V_{FB} - 2\psi_B] - [2qN_A\epsilon_{Si} (V - V_{FB})]^{1/2}$$

The first term in this expression produces a linear dependence of Q on the pixel intensity (as represented by V_{FB}), while the second term gives a square-root nonlinearity. In practice the second term may be made small; for $d_N = 600 \text{ \AA}$, $N_A = 2 \times 10^{14} \text{ cm}^{-3}$, and $V - V_{FB} \approx 5 \text{ V}$, the first term contributes a charge of $4.5 \times 10^{-3} \text{ C/m}^2$ while the second gives $0.2 \times 10^{-3} \text{ C/m}^2$.

Optically addressed readout was demonstrated using 1-mm² capacitors. Figure 5-4 shows the measured output as a function of the input scene level (*not* readout level). One curve was obtained by a conventional capacitive measurement of V_{FB} , while the second curve was obtained by optical readout. The saturation displayed by both curves is a limitation of the MNOS writing process. The close agreement between the curves validates the technique.

The technique is applicable to MOS arrays. In this case, V_{FB} is fixed and the signal is present as mobile inversion-layer charge. The effect of this charge is, in this readout process, equivalent to that of trapped charge in the nitride and is reflected in the substrate charge flow on a nearly one-for-one basis. In effect, exposure to the scene causes a partial discharge of a pixel before readout.

This technique is promising for high-density imagers. Because the only required photolithographic step is the definition of channel stops for pixel isolation, pixels can be made very small. In addition, groups of pixels may be addressed simultaneously, for example, through a mask, to produce on-focal-plane binary/analog correlation. The high output capacitance will, however, limit noise performance, as in charge-injection-device imagers.⁴

R.S. Withers
M.A. Delaney

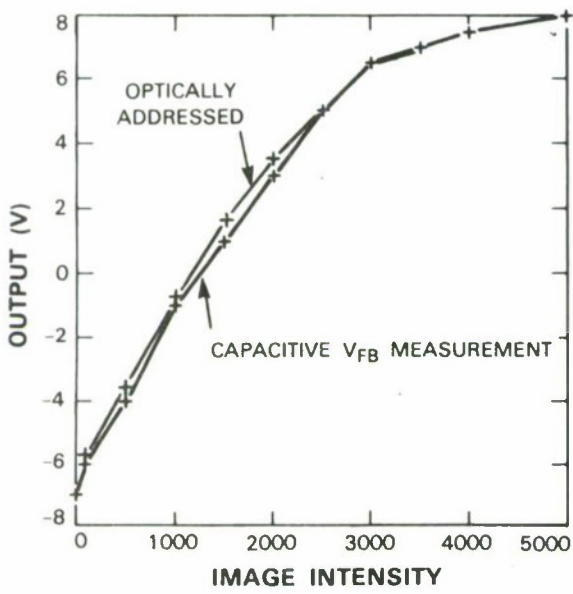


Figure 5-4. Measured output of an MNOS pixel as a function of the stored image intensity. One curve was measured by a conventional $C(V)$ determination of the flatband voltage; the second curve was measured by the optically addressed technique.

5.3 A SAW-BASED COMMUNICATION LINK WITH PRECISE TIME-OF-ARRIVAL MEASUREMENTS

The extreme need for high performance and flexibility in military communications has caused considerable interest in packet radio networks. A demonstration radio that exploits signal processing based on surface-acoustic-wave (SAW) devices for high-antijam-performance pseudonoise (PN) communication has been developed.

Because of the varying needs of tactical situations, it is desirable to provide a means for trading data rate for processing gain. This radio selectively operates from 1.45 Mbps to 44 bps, with a commensurate and nearly optimum trade of data rate for processing gain of 18 dB to 61 dB.

The variability of multipath profiles between mobile users results in problems with data demodulation and with arrival-time measurements that support interradio ranging. Techniques have been developed that include RAKE demodulation of data and incoherent integration for detecting weak leading multipath components.

In this radio, SAW convolvers provide programmable matched filtering with 30-dB processing gain for 100-MHz waveforms with continuously changing PN spreading codes. A hybrid-correlator technique has been devised to extend the processing gain to as much as 61 dB over a wide processing window⁵. This hybrid analog/digital approach utilizes a convolver matched filter and a binary-quantized postprocessor. The analog preprocessing and binary postprocessing make it possible to overcome the limitations encountered when using either technology alone.

Figure 5-5 shows a block diagram of the signal processing in the radio modem. The analog matched filter preprocessor is composed of a 100-MHz PN code generator, a minimum-shift-keying (MSK) modulator, and the convolvers⁶. The code generator is made with three identical custom thick-film hybrids and ECL logic. A VLSI chip from the DARPA silicon foundry is currently under development that will generate the code in eight parallel low-bandwidth channels. The reversed code generator output is modulated to 300-MHz center frequency in the MSK waveform generator to create the reference. The reference is convolved with the incoming signal, resulting in the correlation peak out of the matched filter. The video interface removes the carrier from the matched-filter output and binary quantizes the envelope using various methods to feed the digital postprocessor. The output of the matched filter is approximately the impulse response of the communication channel; consequently, the multipath signals will be easily discernible at the output as delayed correlation peaks. The time resolution of the output multipath profile is the reciprocal of the spreading bandwidth of the waveform, approximately the 100-MHz chipping rate. Provided there is sufficient processing gain in just the convolver to realize adequate signal-to-noise ratio (roughly 10 dB) necessary for low-error-rate data demodulation, the binary RAKE incoherently combines the multipath energy within the processing window to form a data decision. If the convolver processing gain is insufficient, the binary integrator is used to extend the processing (improve the signal-to-noise ratio) and RAKE demodulation is done at its output. In the case where the convolver alone is used for data demodulation, the binary integration is used as a nonintrusive background process to look for previously undetected multipath precursors that represent a better estimate of the line-of-sight transmission path.

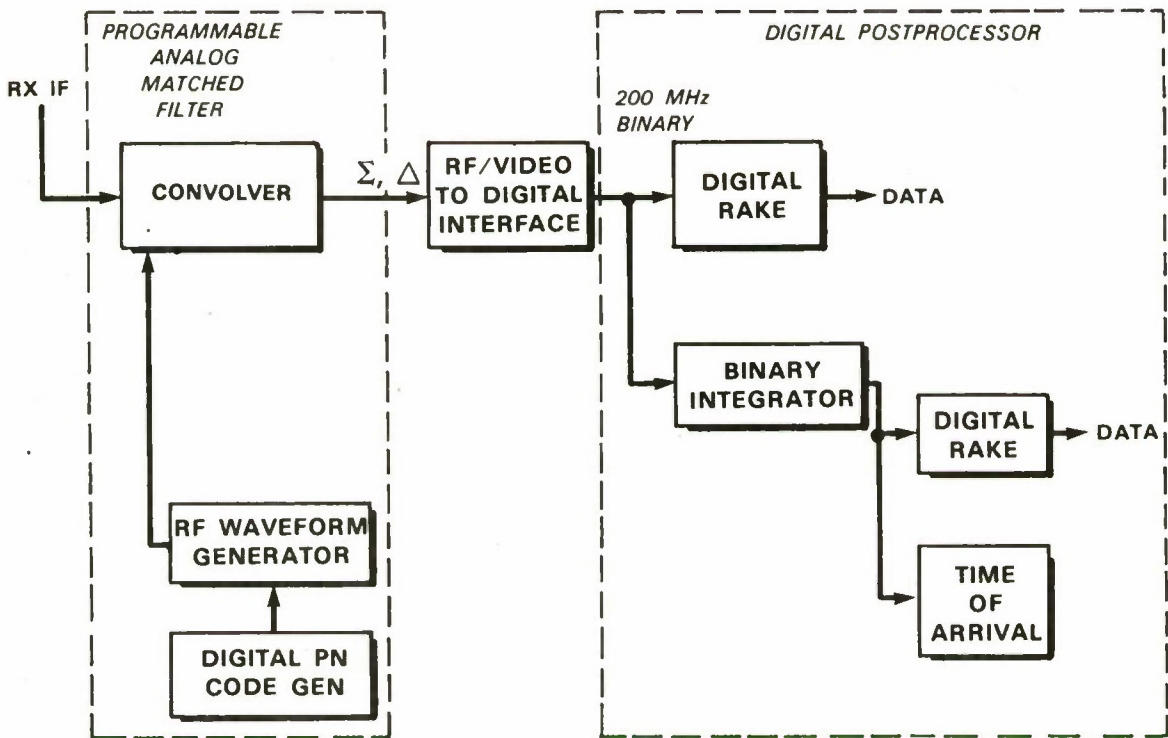


Figure 5-5. The hybrid analog/digital signal processor located in the modem.

In general, the binary integrator accumulates many successive matched-filter outputs on a sample-bin-by-sample-bin basis to extend the 30-dB processing gain provided by the convolver to greater than 60 dB⁷. In the particular case of precursor search, the data value that is imposed on the matched-filter output frame must be removed so that the integration occurs on a unipolar precursor. The binary integrator stores the sampled matched-filter output frame while the data bit is being demodulated. The data value then is stripped off the stored samples so that the accumulation of matched-filter frames will integrate up in a unipolar fashion. The binary integrator operates on 256 sample bins simultaneously in a processing window that is placed just earlier than the demodulation processing window. The precursor search is performed with 3-m resolution, and the processing gain is 15 to 30 dB over the original 30 dB of the matched filter. The result is that with the demodulation of a thousand-bit packet, a window can be searched that represents a half mile in propagation and therefore potential improvement in registering the time of arrival. The 15-30-dB range of processing gain results from the incoherent accumulation in the integrator. At low signal-to-noise ratios, the incoherent processing gain is a strong function of the input signal-to-noise. (Coherent integration may instead be selected; however, the radio requires that no data is transmitted and, therefore, requires a specialized packet type).

The 90 kbps data with the incoherent integration is illustrated in Figure 5-6. The figure does not show the limits in performance. The top photograph shows the time-domain waveform of a received MSK signal contaminated with noise and a small multipath precursor. The large signal is of the order of -10-dB SNR, and the small precursor is of the order of -30-dB SNR. The second photograph shows the detectable main lobe that is used for demodulation and the initial estimate of the time of arrival of the signal. The precursor is barely visible and is indicated by the arrow. The bottom trace is the binary-quantized running data decision, which has only noise when not located under a multipath peak. The next figure is a consecutive frame out of the matched filter. Where there is no multipath present, the binary decision is seen to change randomly. Under the large main lobe, the data is clearly stable, as the signal dominates the noise. Under the precursor, the output is only somewhat stable since it is substantially influenced by the noise. In the fourth photograph, the top trace is the readout clock, and the bottom trace is the detected output out of the binary integrator with a different time scale. The detection to the right is that of the large main lobe and to the left is the precursor. Each clock cycle represents 3 m in range. The distance between the large signal detection and the precursor detection is the corrected time-of-arrival estimate that is available after the data packet is demodulated.

A SAW-based signal processor has been discussed for application to network-radio technology that utilizes a digital postprocessor for RAKE demodulation and time-of-arrival measurements in a diffuse multipath channel. The operation of a hybrid correlator to perform a multipath-precursor search with 3-m resolution over a half-mile range was demonstrated in the laboratory. Future work will include field demonstrations of these circuits in various terrains.

J.H. Fischer
R.R. Boisvert
J.H. Cafarella*

* Author not at Lincoln Laboratory.

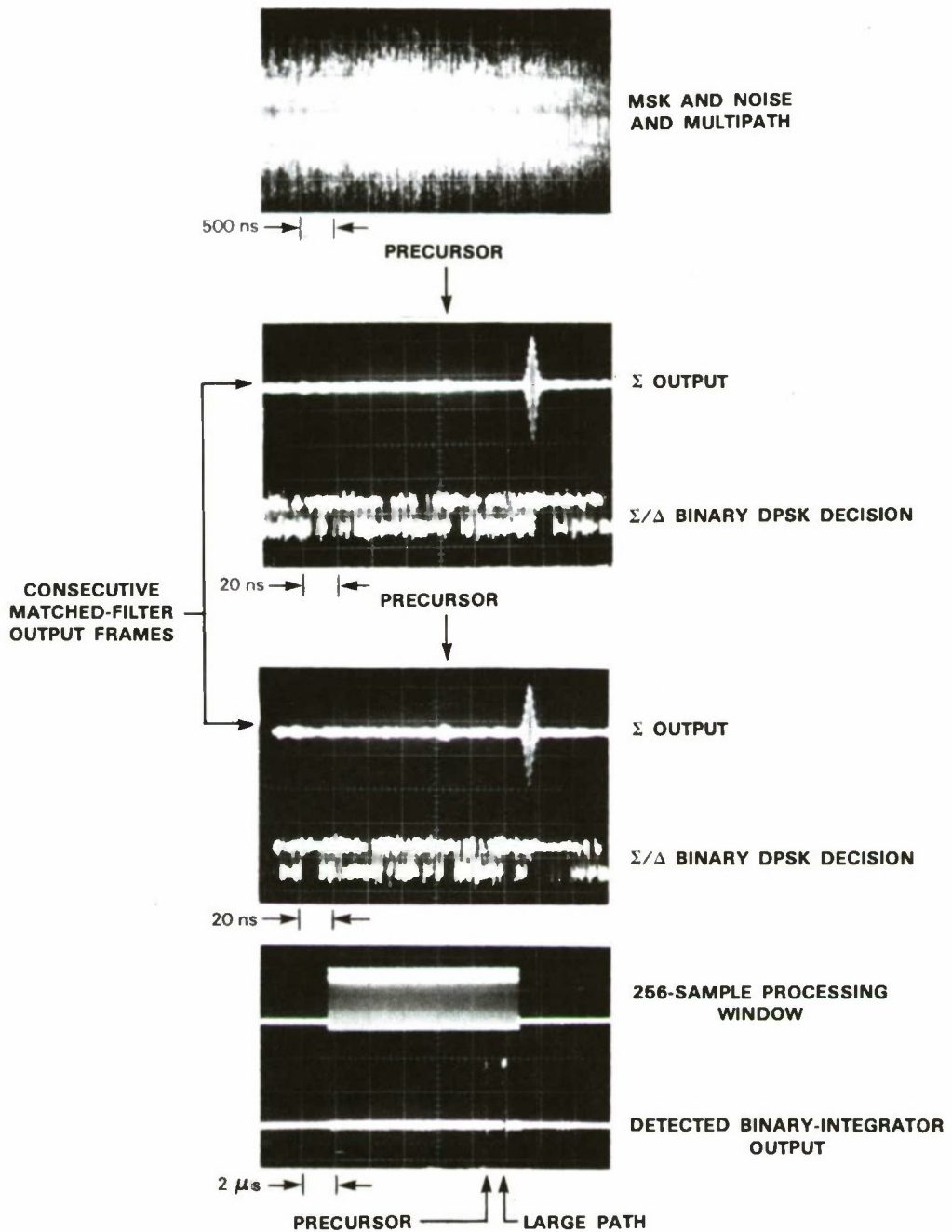


Figure 5-6. Incoherent binary integration for finding a precursor. The top photo is the input to the matched filter. The two middle photos are consecutive output frames from the matched filter, each containing a data bit. The precursor can just barely be seen but will integrate up out of the noise to a detectable level in the binary integrator. The two data bits are the same in this case as can be seen by the output appearing on the sum port. The running DPSK decision that is stored for the binary integrator also is displayed. The bottom photo shows the result out of the binary integrator after detection. The precursor location with respect to the large signal represents the improvement in the time-of-arrival measurement.

REFERENCES

1. "CCD Imagers," Tektronix Integrated Circuits Operation, Beaverton, Oregon (July 1985).
2. R.S Withers, R.W. Ralston, and E. Stern, "Nonvolatile Analog Memory in MNOS Capacitors," IEEE Electron. Device Lett. **EDL-1**, 42 (1980); Solid State Research Report, Lincoln Laboratory, MIT (1979:2), pp. 70-76, DDC AD-A078676.
3. R.S. Withers, D.J. Silversmith, and R.W. Mountain, "MNOS/CCD Nonvolatile Analog Memory," IEEE Electron. Device Lett. **EDL-2**, 165 (1981); Solid State Research Report, Lincoln Laboratory, MIT (1981:1), pp. 53-56, DTIC AD-A103887.
4. G.J. Michon and H.K. Burke, "CID Imager Structure and Operation," 1980 IEEE Intl. Symp. on Circuits and Systems, Houston, Texas, 28-30 April 1980.
5. Solid State Research Report, Lincoln Laboratory, MIT (1980:4), p. 59, DTIC AD-A099712.
6. Solid State Research Report, Lincoln Laboratory, MIT (1984:1), p. 67, DTIC AD-A147429.
7. J.H. Cafarella, "Application of SAW Convolvers to Spread-Spectrum Communication," 1984 Ultrasonics Symposium Proceedings (IEEE, New York, 1984), p. 121.

UNCLASSIFIED

SECURITY CLASSIFICATION OF THIS PAGE (When Data Entered)

REPORT DOCUMENTATION PAGE		READ INSTRUCTIONS BEFORE COMPLETING FORM															
1. REPORT NUMBER ESD-TR-85-302	2. GOVT ACCESSION NO.	3. RECIPIENT'S CATALOG NUMBER															
4. TITLE (and Subtitle) Solid State Research		5. TYPE OF REPORT & PERIOD COVERED Quarterly Technical Report 1 August — 31 October 1985															
		6. PERFORMING ORG. REPORT NUMBER 1985:4															
7. AUTHOR(s) Alan L. McWhorter		8. CONTRACT OR GRANT NUMBER(s) F19628-85-C-0002															
9. PERFORMING ORGANIZATION NAME AND ADDRESS Lincoln Laboratory, MIT P.O. Box 73 Lexington, MA 02173-0073		10. PROGRAM ELEMENT, PROJECT, TASK AREA & WORK UNIT NUMBERS Program Element No. 63250F Project No. 649L															
11. CONTROLLING OFFICE NAME AND ADDRESS Air Force Systems Command, USAF Andrews AFB Washington, DC 20331		12. REPORT DATE 15 November 1985															
		13. NUMBER OF PAGES 92															
14. MONITORING AGENCY NAME & ADDRESS (if different from Controlling Office) Electronic Systems Division Hanscom AFB, MA 01731		15. SECURITY CLASS. (of this Report) Unclassified															
		16a. DECLASSIFICATION DOWNGRADING SCHEDULE															
18. DISTRIBUTION STATEMENT (of this Report) Approved for public release; distribution unlimited.																	
17. DISTRIBUTION STATEMENT (of the abstract entered in Block 20, if different from Report)																	
18. SUPPLEMENTARY NOTES None																	
19. KEY WORDS (Continue on reverse side if necessary and identify by block number) <table style="width: 100%; border-collapse: collapse;"> <tr> <td style="width: 33%; padding-right: 10px;">solid state devices</td> <td style="width: 33%; padding-right: 10px;">photodetectors</td> <td style="width: 33%;">surface acoustic wave devices</td> </tr> <tr> <td>quantum electronics</td> <td>lasers</td> <td>solar cells</td> </tr> <tr> <td>materials research</td> <td>imaging arrays</td> <td>quantum-well devices</td> </tr> <tr> <td>microelectronics</td> <td>signal processing</td> <td></td> </tr> <tr> <td>analog device technology</td> <td>charge-coupled devices</td> <td></td> </tr> </table>			solid state devices	photodetectors	surface acoustic wave devices	quantum electronics	lasers	solar cells	materials research	imaging arrays	quantum-well devices	microelectronics	signal processing		analog device technology	charge-coupled devices	
solid state devices	photodetectors	surface acoustic wave devices															
quantum electronics	lasers	solar cells															
materials research	imaging arrays	quantum-well devices															
microelectronics	signal processing																
analog device technology	charge-coupled devices																
20. ABSTRACT (Continue on reverse side if necessary and identify by block number) <p>This report covers in detail the solid state research work of the Solid State Division at Lincoln Laboratory for the period 1 August through 31 October 1985. The topics covered are Solid State Device Research, Quantum Electronics, Materials Research, Microelectronics, and Analog Device Technology. Funding is provided primarily by the Air Force, with additional support provided by the Army, DARPA, Navy, SDIO, NASA, and DOE.</p>																	